



NTNU – Trondheim
Norwegian University of
Science and Technology

Superhydrophobic Anti-Ice Nanocoatings

Kjetil Knausgård

Nanotechnology

Submission date: August 2012

Supervisor: Zhiliang Zhang, KT

Co-supervisor: Jianying He, KT

Norwegian University of Science and Technology
Department of Structural Engineering

Superhydrophobic Anti-Ice Nanocoatings

Master Thesis
Kjetil Knausgård
Oslo, August 2012



Supervisors:
Prof. Quanshui Zheng & Prof. Zhiliang Zhang



Tsinghua University
Dept. of Engineering Mechanics
in joint collaboration with
Norwegian University of Science and
Technology
Dept. of Structural Engineering



**“ He that stands upon a slippery place, makes nice of
no vile hold to stay him up.**

—William Shakespeare

Abstract

Atmospheric icing from supercooled droplets in the atmosphere can have catastrophic consequences for a number of man-made structures in regions with cold climate and at high altitude, resulting in accidents with both socioeconomic losses and loss of human lives. To mitigate the icing problem, active de-icing involving chemical, thermal and mechanical techniques have been developed to remove ice that has already accumulated. These techniques are sub-optimal, however, as they are plagued with problems such as high energy consumption, hazard to the environment, high economic costs, and need for frequent reapplication.

This thesis takes a look at an entirely different approach, namely utilizing superhydrophobic surfaces to reduce or eliminate the accumulation and adhesion of ice from the outset. Much of the research in the field of superhydrophobicity has involved surfaces with open-cell structures, e.g. pillar-like surfaces and surfaces with bumps and valleys. It has been reported that surfaces with closed cells have a comparative advantage in that they are better at retaining their hydrophobic properties under pressure. This thesis investigates the wetting properties (which are often closely tied to icephobic properties) of closed-cell structures further, using LAMMPS simulations. The simulations show that wetting on these surfaces satisfies the well-known theories of Wenzel and Cassie-Baxter. However, on the small scale on which the simulations were carried out, the effect of tuning the roughness scale is not as predicted by theory. Furthermore, no comparative advantage against open-cell structures could be demonstrated for the closed-cell surfaces.

A physical experiment was also carried out, in which the influence of water condensation on the dynamic behavior of water droplets on a nearly-superhydrophobic black silicon surface was tested. The results confirm a well-known problem: Condensation severely deteriorates the water repellency of hydrophobic surfaces.

The literature review and experiments in this thesis shows that superhydrophobic surfaces have a great potential for use in anti-icing applications, demonstrating delayed freezing, reduced ice accumulation, and reduced ice adhesion. Nevertheless, major problems are yet to be solved, including deterioration of icephobicity due to mechanical damage, and reduced icephobicity in humid conditions.

Sammendrag

Atmosfærisk ising av underkjølte vanndråper i atmosfæren kan ha katastrofale konsekvenser for en rekke menneskeskapte konstruksjoner i kalde områder og i stor høyde, og føre til ulykker med både sosioøkonomiske tap og tap av menneskeliv. For å redusere problemene knyttet til ising har det blitt utviklet aktive avisingsteknikker som ved hjelp av kjemiske, termiske og mekaniske metoder fjerner is som allerede har festet seg. Disse teknikkene er imidlertid suboptimale, da de er energikrevende, lite miljøvennlige, dyre, og krever hyppig utskifting og vedlikehold.

Denne avhandlingen tar for seg en helt annen tilnærming til problemet, nemlig bruk av superhydrofobe overflater for å redusere eller eliminere isdannelse. Mye av forskningen på superhydrofobitet har involvert mikro- og nanostrukturerte overflater bestående av søyler eller andre strukturer med såkalte ”åpne celler”. Det har blitt rapportert at overflater med lukkede celler er bedre egnet enn disse til å bevare de hydrofobe egenskapene under trykk. Denne avhandlingen undersøker nærmere de hydrofobe egenskapene (som ofte henger nøye sammen med anti-icing-egenskaper) til overflater med lukkede celler, ved hjelp av molecular dynamics-simuleringer. Resultatene av disse simuleringene er i samsvar med det som de velkjente teoriene til Wenzel og Cassie og Baxter predikerer. Siden simuleringene ble gjort på nanonivå er imidlertid effekten av å endre overflatens ruhetsskala (eng.: ”roughness scale”) ikke den samme som på makronivå. Det ble heller ikke påvist noe komparativt fortrinn for overflatene med lukkede celler i forhold til overflatene med åpne celler.

Det ble også gjort et fysisk forsøk hvor målet var å se om vanndråper som treffer en hydrofob overflate oppfører seg annerledes når det er vannkondensat på overflaten. Forsøket bekrefter et velkjent problem: De vannavstøtende egenskapene til hydrofobe overflater blir kraftig hemmet som følge av vannkondens.

Litteraturgjennomgangen og forsøkene i denne avhandlingen viser at superhydrofobe overflater har et stort potensial for bruk innen anti-ising. Både tregere frysing, redusert akkumulering av is, og redusert heft til overflaten har blitt påvist. Det er imidlertid fortsatt flere uløste problemer, deriblant redusert evne til å motvirke isdannelse på grunn av mekanisk skade, og svekket funksjon i fuktige omgivelser.

摘要

过冷水滴在大气中的结冰现象对高寒地区的很多人造结构都可能带来灾难性的后果，不仅会造成社会经济的损失，还可能夺去人们的生命。为了解决结冰问题，人们基于化学，热学，力学的方法发展了许多主动除冰技术。然而，这些方法都有种种明显的缺点：耗费能源，破坏环境，昂贵或效果不持久。

本文关注一种完全不同的被动防冰方法，即利用超疏水表面减少或消除冰的累积和粘附。超疏水领域的许多研究都涉及到开放式结构表面，例如柱状结构表面。有研究表明，由于在一定压力下仍然可以保持较好的疏水性能，封闭式结构表面在防冰性能方面具有一定优势。本文将利用分子动力学软件LAMMPS，进一步研究封闭式结构表面的润湿性。计算结果表明，这种结构表面的润湿性仍然满足众所周知的Wenzel和Cassie-Baxter理论，但在分子动力学模拟所能计算的纳米尺度下，表面粗糙度对润湿性的影响未能显现。此外，封闭式结构表面相对于开放式结构表面并没有显示出优势。

本文还开展了实验研究，以测试水汽在超疏水的黑硅表面的凝结对水滴动态行为的影响。实验结果证实了一个众所周知的问题：水汽在表面的冷凝会使表面的疏水性丧失。

文献综述和本文的实验表明，超疏水表面在表面防冰领域具有巨大的应用潜力，可以延迟水滴的冻结，减少表面积冰，减小冰的粘附。然而，仍然有一些重要问题尚未得到解决，例如表面结构的力学稳定性，表面在潮湿环境下防冰性能的丧失等。

Contents

List of Symbols and Abbreviations	vii
1 Introduction	1
1.1 The Problem of Icing and Current Solutions	1
1.2 Purpose and Scope of the Project	3
1.3 Outline of the Report	3
1.4 Acknowledgements	5
2 Atmospheric Icing and Meteorological Aspects	6
2.1 Precipitation Icing	6
2.2 In-Cloud Icing	8
3 Basic Principles of Superhydrophobicity	11
3.1 Surface Tension and Contact Angle	11
3.2 The Wenzel State	13
3.3 The Cassie-Baxter State	16
3.4 Mixed States	19
3.5 Controversy Regarding the Wenzel and the Cassie-Baxter Models	20
3.6 Sliding Behavior	22
3.6.1 Contact Angle Hysteresis and Critical Tilt Angle	22
3.6.2 Effect of Surface Directionality on Sliding Behavior	23
3.7 Conditions for Superhydrophobicity	25
4 Stability of the Cassie-Baxter State	30
4.1 Effect of Roughness and Solid-Liquid Fractional Interface	31
4.2 Effect of Curvature	31

4.3	Effect of Pillar Height, Pillar Diameter, Pillar Slenderness and Inter-Pillar Pitch	33
4.4	Effect of Pillar Rigidity	37
4.5	Effect of Immersion in Water	38
4.6	Effect of Droplet Size	39
4.7	Effect of Roughness Scale and Cross-Sectional Geometry	40
4.8	Effect of Pressure and Droplet Velocity	43
4.9	Effect of Cell Structure	47
4.10	Effect of Temperature and Water Condensation	47
5	Correlation Between Hydrophobicity and Icephobicity	50
5.1	Delayed Static Freezing	51
5.2	Reduced Dynamic Freezing	52
5.3	Effect of Nanoscale Roughness on Freezing Delay	57
5.4	Reduced Ice Adhesion	59
5.5	Deterioration of Icephobicity	61
6	Characterization and Testing of of Superhydrophobic and Icephobic Properties	67
6.1	Chemical Composition and Morphological Characterization	67
6.2	Measuring Wettability	69
6.3	Measuring Ice Adhesion	70
7	Fabrication of Superhydrophobic Surfaces	73
7.1	Lithography Techniques	74
7.2	Electrospinning	75
7.3	Phase Separation	76
7.4	Layer-by-Layer Assembly	76
7.5	Etching and Anodic Oxidation	76
7.6	Etching and Spin-Coating	77
7.7	Superhydrophobic Coating Made from Candle Soot	78
7.8	Graphene Nanomeshes (GNMs)	78
7.8.1	Graphene and GNM	79
7.8.2	Production of GNMs	80

8	Condensation Theory	84
8.1	What is Condensation?	84
8.2	Growth Laws	84
8.3	How Condensation Affects Wettability	85
9	Simulation Theory	94
9.1	Basic Theory of Molecular Dynamics	94
9.2	Software	96
9.3	Wetting Simulation in LAMMPS	97
10	Graphene Nanomesh Simulations	102
10.1	Preparation	103
10.2	Experimental	105
10.3	Results	106
10.3.1	Simulations with Surfaces of Constant S and Varying f_1	107
10.3.2	Simulations with Surfaces of Constant f_1 and Varying S	110
10.4	Discussion	111
11	Droplet Impact Experiments	116
11.1	Preparation	116
11.2	Experimental	119
11.3	Results	120
11.4	Discussion	121
12	Conclusions and Outlook	124
A	Programming codes	127
A.1	Code used to create graphene layers	127
A.2	Code used to convert XYZ file to gro file	131
A.3	Code Used to Cut Holes in the Graphene	133
A.4	Code Used to Convert .gro files to LAMMPS input files	136
A.5	Input file	140

List of Symbols and Abbreviations

A	Pillar cross-sectional area
A_c	Pillar cell area
A_{LA}	Liquid-air interface area
A_{SL}	Solid-liquid interface area
A_F	The projection of A_{SL} on a flat plane along the surface
α	Critical tilt angle
CA	Contact angle
CAH	Contact angle hysteresis
χ	Ratio of the area that has transitioned to the Wenzel state
D	Pillar diameter
δ	Maximum droop of water droplet
E	Young's modulus
η	Slenderness ratio
η_e	Equi-energy slenderness ratio
f_1	Liquid-solid fractional area under a droplet resting on a surface
f_2	Liquid-air fractional area under a droplet resting on a surface
F_{cr}	Critical buckling force
g	Acceleration of gravity
γ	Surface tension of a material
γ_{LA}	Surface tension of liquid-air interface
γ_{SA}	Surface tension of solid-air interface
γ_{SL}	Surface tension of solid-liquid interface
γ_{IW}	Surface tension of ice-water interface
H	Pillar height
H_e	Equi-energy pillar height
I	Moment of Inertia
κ_c	Capillary length
L	Pillar perimeter

L_T	Total length of the triple-phase intersection lines per unit apparent contact area
λ	Triple-phase intersection line tension
P	Pitch distance
r_c	Critical nucleus radius
r_f	Roughness factor for the wet area in the Cassie-Baxter state
R_f	Total roughness factor
ρ	Density of droplet
RMS	Root mean square
S	Area of pillar cross section per boundary length
S_{SK}	Surface skewness
S_{KU}	Surface kurtosis
SA	Critical tilt angle
τ	Ice adhesion strength
θ	Contact angle
θ_{CB}	Cassie-Baxter contact angle
θ_Y	Young's contact angle
θ_0	Young's contact angle
θ_W	Wenzel contact angle
θ_A	Advancing contact angle
θ_R	Receding contact angle
$\theta_{Y,c}$	Critical Young's contact angle
θ_M	Mixed state contact angle
V	Droplet velocity
w	Width of droplet perpendicular to the direction of sliding
W_{SL}	Work of adhesion per unit area of solid-liquid interface

Chapter 1

Introduction

1.1 The Problem of Icing and Current Solutions

Atmospheric icing from supercooled droplets in the atmosphere, also known as "freezing rain", can have catastrophic consequences for many man-made structures and equipment both on the ground and in the air, resulting in socioeconomic losses and fatal accidents with loss of human lives. The high adherence of ice to both metallic and insulating surfaces can severely limit or even destroy equipment and structures in industries like aviation, hydropower, telecommunications, navigation, electrical distribution, and all forms of transportation.^[1]

As an example, consider powerlines. Ice accretion on these structures is a severe problem which can lead to insulator flashover, wire breakage and collapsing powerline towers.^[2] The image in Figure 1.1 represents the largest ice accretion ever recorded on an overhead powerline. The rime ice was measured to have a maximum diameter of 1.4 m and was weighed to 305 kg/m. The image dates to 1961 and was captured in Norway at an altitude of ca. 1400 m.^[3]

Ice accumulation is also a severe problem for aircraft, where planes are exposed to supercooled water droplets both on the ground and while flying through clouds in the troposphere. The presence of even a scarcely visible layer of ice can limit the function of wings, propellers, windshields, antennas, vents, intakes and cowlings. For example, ice accumulated on the horizontal tail stabilizer reduces its ability to balance the tendency of the nose to pitch downward. This can lead to a phenomenon called *tail stall*.^[4] The situation is shown in Figure 1.2. Furthermore, ice on aircraft wings prevents the smooth flow of air past the wings, which leads to increased drag and decreased ability



Figure 1.1: Rime icing on an electric powerline in Norway in April 1961.^[3]

to create lift. Wind tunnel and flight tests have shown that an ice layer the thickness of a piece of coarse sand paper can reduce the lift by 30 percent and increase drag up to 40 percent.^[5]

Loss of lift force due to ice build-up on the wings and/or tail is believed to have caused the tragic Buffalo crash of Colgan Air Flight 3407 that killed 50 people on February 12 2009.^[6] Another aircraft accident due to atmospheric icing was the American Eagle Flight 4184 crash on October 31 1994. The plane encountered freezing rain, and rapid ice build-up followed. The pilots lost control of the aircraft, and crashed into a soybean field near Roselawn, Indiana, killing all 68 people on board.^[7]

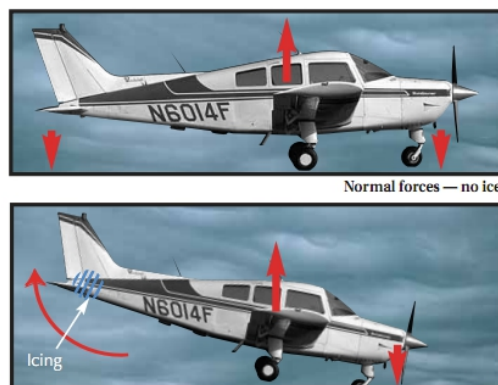


Figure 1.2: Ice lessens the ability of the horizontal tail stabilizer to generate downward lift, and the tail stalls.^[8]

Because of all these problems, significant effort has been exerted to de-

velop surfaces that simplify the removal of ice or slow down its formation. Most of these efforts involve chemical, thermal or mechanical techniques for removing ice that has already accumulated. These are referred to as *active* de-icing techniques. Another possibility is to apply so-called "sacrificial" coatings that are removed from the substrates over time, e.g. sol-gel coatings that slowly release chemical compounds that decrease the freezing point of water.^[9]

These methods are suboptimal, however, as they are plagued with problems such as high energy consumption, hazard to the environment,^[10] high economic costs, and the need for frequent reapplication. A much more appealing solution would be to engineer permanent surfaces that reduce or eliminate ice accumulation from the outset. The latest research strategies are showing great promise for creating *passive* icephobic surfaces like this.

1.2 Purpose and Scope of the Project

This master thesis completes my five year Master of Science program at the Norwegian University of Science and Technology (NTNU). Most of the work was carried out at the Center for Nano- and Micro Mechanics (CNMM) at Tsinghua University, Beijing, under the supervision of Professor Quanshui Zheng (Tsinghua University) and Professor Zhiliang Zhang (NTNU). The thesis has had a broad approach, having the following purposes:

- To explain the problem of icing, and how superhydrophobic surfaces can be used to mitigate this problem.
- To introduce the field of superhydrophobicity research, including relevant mathematical equations.
- To give an overview of different strategies used to create superhydrophobic surfaces, including some fabrication methods.
- To use molecular dynamics simulations to simulate wetting on some of the most interesting surface structures outlined in the theory section.
- To observe the effect of water condensation on the dynamic behavior of water droplets on hydrophobic surfaces.

1.3 Outline of the Report

The report is organized as follows:

- Chapter 2 comprises a review of the fundamentals of atmospheric icing, with emphasis on the difference between glaze ice and rime ice.
- Chapter 3 reviews the basic principles of wetting and superhydrophobicity, including concepts like contact angle, contact angle hysteresis, and the difference between the Wenzel and the Cassie-Baxter states.
- Chapter 4 surveys the influence of a variety of parameters on the stability of the Cassie-Baxter state—a state which is a prerequisite for a micro-nano hierarchically structured surface to be superhydrophobic.
- Chapter 5 deals with the correlation between superhydrophobicity and icephobicity. The influence of different wetting parameters on ice accretion and ice adhesion are illuminated. Some major problems that cause deterioration of the icephobic properties are also covered.
- Chapter 6 presents experimental methods that are commonly used to characterize superhydrophobic surfaces, and to measure their wetting and icephobic properties.
- Chapter 7 examines different processing routes for the manufacture of superhydrophobic surfaces. Both top-down and bottom-up approaches are explained.
- Chapter 8 focuses on condensation, and how it affects wettability.
- Chapter 9 provides a short introduction to the basics of molecular dynamics, and how programs like LAMMPS can be used to simulate the wetting behavior of a liquid droplet on a surface.
- Chapter 10 covers the molecular dynamics simulations carried out in this thesis, including the preparations, the experimental part, the results and a discussion.
- Chapter 11 presents the physical experiments with droplets impinging on dry surfaces and on surfaces exposed to water condensation. Like Chapter 10, this chapter is divided into a preparation part, an experimental part, a results part and a discussion part.
- Chapter 12 summarizes the report and provides some recommendations for future work. An exotic brand new approach to overcome the problems outlined in Chapter 5 is also presented.
- Appendix A contains the programming codes referred to in Chapter 10.

1.4 Acknowledgements

I would like to thank my supervisors, Professor Zhiliang Zhang and Professor Quanshui Zheng, and their co-workers at the Department of Structural Engineering (NTNU) and Center for Nano- and Micro Mechanics (Tsinghua), respectively, for their interest and support during my work. Special thanks to Xiong Wei for invaluable assistance—both professionally and personally—during my stay in Beijing.

Chapter 2

Atmospheric Icing and Meteorological Aspects

Atmospheric icing occurs when freezing rain, wet snow or supercooled liquid droplets (droplets cooled below 0°C) in the atmosphere freeze upon contact with exposed surfaces. Icing of water on a surface is a complex phenomenon, involving three major forces: hydrogen bonding, Lifshitz-van der Waals bonding and direct electrostatic interactions.^[11] The relative contributions of these forces depend on the material on which icing occurs. The fundamental physics of ice adhesion are still not thoroughly understood. Nonetheless, the different types of icing can be divided into two main categories, depending on factors such as wind speed, water droplet size, temperature and substrate properties. The two categories are *precipitation* icing and *in-cloud* icing.^[3] Precipitation icing results from the freezing of precipitation like rain or snow upon contact with a surface. In-cloud icing results from the deposition of cloud or water vapor droplets.

2.1 Precipitation Icing

The lowest part of the Earth's atmosphere is called the *troposphere*. This is where most of the clouds in the atmosphere are found.^[12] The temperature in the troposphere generally gets colder with increasing altitude. Under certain conditions, however, the temperature gradient is inverted in the lowest layer of the troposphere, so that the air is colder near the Earth. The most common type of temperature inversion in the troposphere is probably *radiation inversion*. This can for example happen after sunset during winter, when heat in the layer in the immediate vicinity of the Earth's surface is radiated into space. Since air is a poor conductor of heat, the air above this cooled

layer is left almost unaffected, and the result is a temperature inversion with a warmer layer of air resting above a colder layer.^[13]

If the temperature at the surface is below 0°C and the temperature at the highest point of the inversion layer (Z_{max}) is above 0°C , a region ($H_{melting}$) is created where falling snow flakes and ice particles melt and form raindrops on their way to the ground (see Figure 2.1). When the raindrops enter the inver-

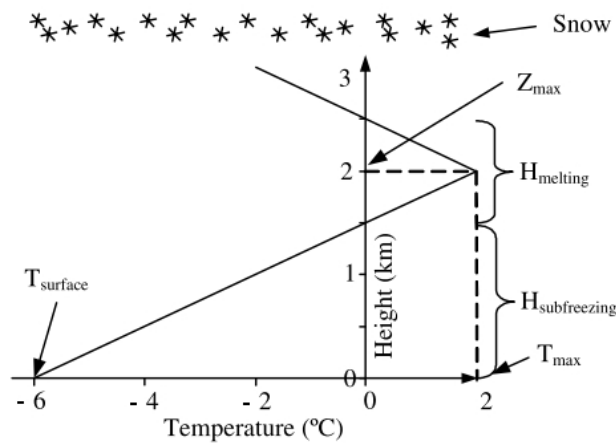


Figure 2.1: Example of vertical temperature distribution in the lower troposphere.^[14]

sion layer and the temperature decreases, the raindrops become supercooled, and they remain in this state—which is thermodynamically unstable—until they hit the ground and freeze, or collide with particles in the atmosphere that act as nuclei for ice crystal growth. The type of precipitation that finally reaches the ground may be rain, ice pellets, slush, wet snow or snow, depending on the specific atmospheric conditions, e.g. the temperature gradients and the thickness of the H_{melt} layer.^[14]

Precipitating water droplets rarely freeze immediately upon contact with an exposed surface even if they are supercooled, so they have sufficient time to wet the surface before they freeze. The result is the build-up of a smooth, high-density layer of clear and solid *glaze ice*,^[15] which is shown in Figure 2.2c. Glaze ice from precipitating water droplets may accumulate at much higher rates than other types of ice. It is also relatively dense, so it exerts a greater force on the substrate on which it accumulates. This type of ice is also a better conductor of electricity, and it therefore poses a greater threat to the operation of electrical networks.

2.2 In-Cloud Icing

In-cloud icing usually results in either *soft rime* or *hard rime*, depending on conditions such as air temperature, humidity, size distribution of the water droplets, and wind speed perpendicular to the exposed surface. Rime is characterized by its opaque and rough appearance, as shown in Figure 2.2a and 2.2b. This type of icing is common at high altitudes and at low temperatures, and is first and foremost a problem for structures located at freely exposed mountain passes where mountain valleys force moist air to higher altitudes while increasing the wind speed.^[16]

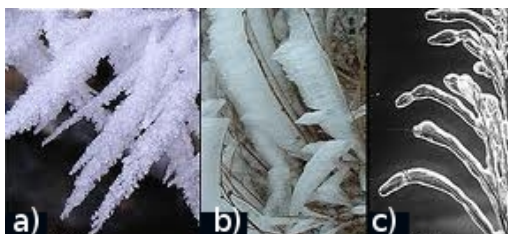


Figure 2.2: (a) Soft rime, (b) hard rime and (c) glaze ice.^[17]

The water droplets hitting the surface freeze as soon as the latent heat of fusion is transferred to the substrate.^[15] When the freezing rate is higher than the flux of impinging water droplets, air bubbles will get trapped in the ice structure. The more trapped air, the "softer" the rime. If the flux of water droplets is higher than the freezing rate, however, the water droplets will tend to wet the surface before freezing, and clear and solid bubble-free glaze ice results.^[15]

Since the heat transfer depends on the temperature gradient between the surface and the liquid, rime formation is more likely to occur at lower temperatures, while glaze ice more frequently occurs at temperatures just below the freezing point where the water has plenty of time to wet the surface before freezing occurs (see Figure 2.3). The wind speed also plays a role. Soft rime and hard rime are more likely to occur under calm conditions, while the probability of glaze ice formation increases with increasing wind speed. This is because the wind helps the water spread on the surface. It should be noted that at very low temperatures (below $\sim -20^{\circ}\text{C}$), the liquid water content in the air is so low that virtually no in-cloud ice formation occurs.^[15]

A third phenomenon besides rime and glaze ice is *hoar frost*, which has a featherlike appearance. The frost process starts with the condensation of vapor on a cold surface to form water droplets. Then the water droplets

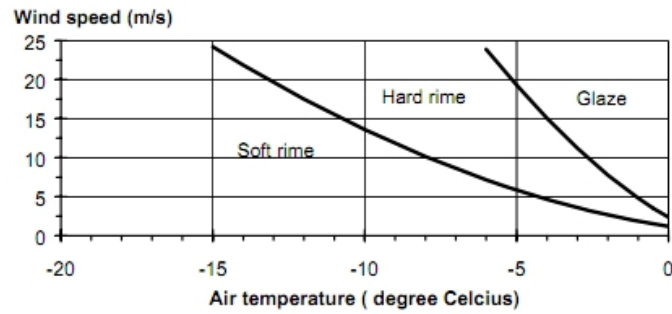


Figure 2.3: Type of accreted atmospheric ice as a function of air temperature and wind speed.^[16]

Type of ice	Density [kg/m ³]	Adhesion and cohesion	Color	Shape
Glaze	900	strong	transparent	evenly distributed / icicles
Hard rime	600-900	strong	opaque	eccentric, pointing windward
Soft rime	200-600	strong to medium	white	eccentric, pointing windward

Table 2.1: Key properties of atmospheric ice.^[16]

freeze, and frost deposition can take place by direct sublimation of super-cooled water droplets in the air to the ice crystals.^[18] Due to the light weight and low adhesion, this type of ice is relatively harmless to most structures.^[3]

A summary of some of the key properties of glaze ice, hard rime and soft rime is presented in Table 2.1. Table 2.2 shows some of the most important meteorological parameters influencing ice accretion.

Type of ice	Air temperature [°C]	Wind speed [m/s]	Droplet size	Water content in air	Typical event duration
Precipitation icing					
Glaze	$-10 < t_a < 0$	any	large	medium	hours
In-cloud icing					
Glaze	see Fig. 2.3	see Fig. 2.3	medium	high	hours
Hard rime	see Fig. 2.3	see Fig. 2.3	medium	medium	days
Soft rime	see Fig. 2.3	see Fig. 2.3	small	low	days

Table 2.2: Meteorological parameters influencing ice accretion.^[16]

Chapter 3

Basic Principles of Superhydrophobicity

Superhydrophobic surfaces are characterized by their extreme water-repellent properties. These surfaces have recently received a lot of attention because of their potential applications in, for example, weather resistant garments, fluidic systems with reduced drag, self-cleaning windows, roof tiles, solar panels, and—as we shall see—anti-icing coatings.^[19] A fact that demonstrates the enormous growth of interest is the number of articles on superhydrophobic surfaces published between 2006 and 2007, which was more than double the total number of articles published previously on the topic.^[20] In this chapter the basic theory behind superhydrophobicity is outlined.

3.1 Surface Tension and Contact Angle

The surface of any material is associated with an excess energy which stems from the much higher fraction of broken bonds among the surface atoms than among the atoms in the bulk. This excess energy is commonly referred to as the surface tension, γ , which is the work required per unit area in increasing the surface area at constant pressure and temperature.^[21] In SI units, the surface tension is measured either in energy per unit area or force per unit length, i.e., J/m^2 or N/m . The surface tension of a given material can be chemically modified, for example by fluorination.^[22]

A droplet suspended in a gas phase is subjected to two forces which determine its shape: The surface tension, which acts to minimize the surface area, i.e., making the droplet spherical; and the gravitational force, which acts to flatten it. The effect of gravity can be neglected as long as the size of the droplet is smaller than the so-called *capillary length*,^[23]

$$\kappa_c = \sqrt{\frac{\gamma_{LA}}{\rho g}} . \quad (3.1)$$

Here, γ_{LA} is the surface tension of the liquid-air interface, ρ is the liquid density, and g is the acceleration of gravity. At ambient conditions, the capillary length of clean water is ~ 2.7 mm.^[23]

When a water droplet is brought in contact with a perfectly smooth and chemically homogeneous surface, a part of the solid-air interface is replaced with a solid-liquid interface of the same area. The energy of the solid-liquid-air system is now reduced by an energy given by the Dupr e equation,^[24]

$$W_{SL} = \gamma_{SA} + \gamma_{LA} - \gamma_{SL}, \quad (3.2)$$

where W_{SL} is the work of adhesion per unit area, and γ_{SA} , γ_{LA} and γ_{SL} are the solid-air, liquid-air and solid-liquid interface energies, respectively. The shape of the droplet changes due to the introduction of the new interface. In the case where the solid-liquid interface energy is lower than the solid-vapor interface energy, the droplet will tend to spread spontaneously on the surface. If the solid-liquid interface energy is higher than the solid-vapor interface energy, on the other hand, then spontaneous spreading will not occur. Instead, the droplet will bead up and assume a more spherical shape.

The angle that the outline tangent of the droplet makes with the surface at the three-phase contact line is known as the *contact angle* (CA) of the system (see Figure 3.1). On a smooth and chemically homogeneous surface,

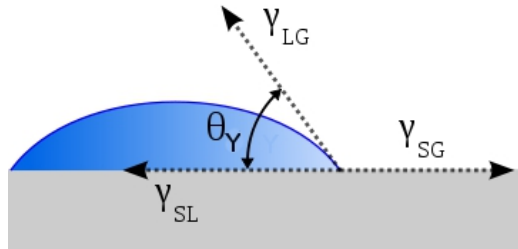


Figure 3.1: The contact angle θ_Y and all the surface tensions in a system consisting of a water droplet resting on a smooth surface.

this contact angle is called *Young's contact angle*, usually denoted θ_Y or θ_0 . When the size of the droplet is smaller than the capillary length and when the volume and pressure are constant, then θ_Y can be determined by minimizing the net surface tension of the three interfaces of the system,^[24]

$$E_{tot} = \gamma_{LA}(A_{LA} + A_{SL}) - W_{SL}A_{SL}, \quad (3.3)$$

where A_{LA} and A_{SL} are the liquid-air and solid-liquid interface areas, respectively. In equilibrium we have

$$dE_{tot} = \gamma_{LA}(dA_{LA} + dA_{SL}) - W_{SL}dA_{SL} = 0. \quad (3.4)$$

Using the geometrical relationship $dA_{LA}/dA_{SL} = \cos\theta_Y$,^[24] and combining Equation 3.2 and 3.4, one obtains the well-known *Young equation* for the contact angle on a flat and chemically homogeneous surface:^[24]

$$\cos\theta_Y = \frac{\gamma_{SA} - \gamma_{SL}}{\gamma_{LA}}. \quad (3.5)$$

This equation tells us that a liquid droplet will spread on a surface when $\gamma_{SA} - \gamma_{SL} \geq \gamma_{LA}$ ($\cos\theta_Y \geq 1$, $\theta_Y = 0$), form a contact angle of 90° when $\gamma_{SA} = \gamma_{SL}$ ($\cos\theta_Y = 0$), and form a contact angle higher than 90° when $\gamma_{SA} < \gamma_{SL}$ ($\cos\theta_Y < 0$).

Surfaces that exhibit low γ_{SA} are usually characterized by possessing few (or even no) polar surface groups.^[25] The CA is often used as a relative measure of the hydrophobicity of a surface, i.e., of its tendency to repel water. A CA of 0° means that the surface is totally wetted, while a CA of 180° corresponds to complete non-wetting. Generally, the lower the surface tension γ_{SA} , the higher the contact angle θ_Y of a surface. Surfaces with CA greater than 90° are classified as *hydrophobic*, whereas surfaces with CA less than 90° are referred to as *hydrophilic*.^[26] Subdividing even further: When the water CA is higher than 150° , the surface is said to be *superhydrophobic*. Some definitions of superhydrophobicity also require the surfaces to have a low *contact angle hysteresis* (CAH), which we will come back to in Section 3.6.

On flat surfaces, the highest water CA that can be obtained is 115 - 120° (for poly(tetrafluoroethylene) or fluorine-terminated organic surfaces).^[23] In other words, surface chemistry alone is not sufficient to create superhydrophobic surfaces. Superhydrophobicity can be achieved, however, by combining an "intrinsically" hydrophobic material with an appropriate surface texture or roughness.

3.2 The Wenzel State

The Young equation does not apply when the flat surface is replaced with a rough one. In this case, the surface tension is not the only factor affecting the

wettability of the water droplet; the surface roughness also enters the picture. On a rough surface, the deposited water droplet faces the alternatives of two main configurations, corresponding to two different equilibrium states of the droplet.^[27] The first possibility that will be discussed is for the droplet to conform to the contours of the solid surface, i.e., "wetting" the grooves of the surface. This is called the *Wenzel* state, named after Robert N. Wenzel who outlined the principles of this model in 1936.^[28] The model is schematically depicted in two dimensions in Figure 3.2, where the surface roughness consists of regularly arranged square pillars.

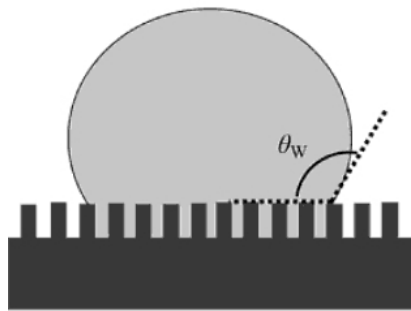


Figure 3.2: Schematic illustration of a droplet in the Wenzel state.^[19]

Wenzel argued that, since the actual solid-liquid contact area is greater under the droplet if the surface is rough than if it is smooth, then a surface that is spontaneously wetted when it is smooth will be wetted more rapidly when the surface is rough, as there is a greater net energy decrease to induce wetting. In the same way, surfaces for which the solid-liquid interface energy is higher than the solid-air interface energy—i.e., surfaces that are intrinsically water-repellent—will be even harder to wet when the surface is rough.

The equilibrium condition for a water droplet in the Wenzel state is given by^[28]

$$\cos \theta_W = R_f \cos \theta_Y . \quad (3.6)$$

Here, θ_W is the apparent contact angle in the Wenzel state, θ_Y is the Young CA for a flat surface of the same material, and R_f is the *roughness factor* defined as the ratio of the actual solid-liquid area A_{SL} to its projection on a flat plane A_F along the surface. The value of R_f on a rough surface must hence be larger than one.

Consider a surface with a surface roughness made up of a regular array of square cross-sectional pillars of length a , periodic interpillar spacing b , and height H (see Figure 3.3). For such a surface, the roughness is given by $R_f = 1 + (4aH)/(a + b)^2$. The Wenzel equation can then be written^[29]

$$\cos \theta_W = \left(1 + \frac{4A}{a/H}\right) \cos \theta_Y, \quad (3.7)$$

where the parameter A is given by $A = 1/((b/a) + 1)^2$.

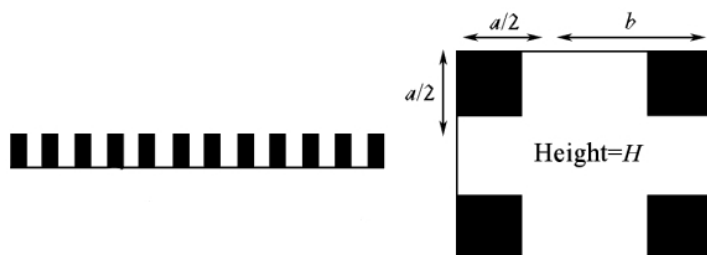


Figure 3.3: A three-dimensional model of the roughness on a surface.^[29]

As indicated above, it follows from Wenzel's equation that droplets in the Wenzel state will tend to amplify the "intrinsic" behavior of the surface: Hydrophilic surfaces ($\theta_Y < 90^\circ$) will become more hydrophilic, which means that the CA will decrease; whereas hydrophobic surfaces ($\theta_Y > 90^\circ$) will become more hydrophobic, corresponding to increased CA values. For a flat surface ($R_f=1$), the Wenzel equation yields the Young equation (3.5). The dependence of the CA on the roughness factor R_f is schematically illustrated in Figure 3.4.

This amplifying tendency has been demonstrated by Jung and Bhushan.^[30] The bar chart in Figure 3.5 shows measured contact angles of water droplets approximately 5 μL large deposited on both hydrophilic and hydrophobic surfaces made from poly(methyl methacrylate) (PMMA). PMMA is a polymer that has polar (hydrophilic) groups with high surface energy, but the surfaces were made hydrophobic by coating them with a hydrophobic self-assembled monolayer (SAM) of perfluorodecyltriethoxysilane (PFDTES). In addition to flat PMMA films, ordered nanostructured surfaces with asperities of both low and high height-to-diameter aspect ratio (LAR and HAR) were processed using soft lithography, as well as a replica of the lotus leaf (this will be covered later in the chapter) microstructure with randomly distributed asperities (see Figure 3.6). These surfaces had roughness factors R_f of 2.1, 5.6 and 3.2, respectively.

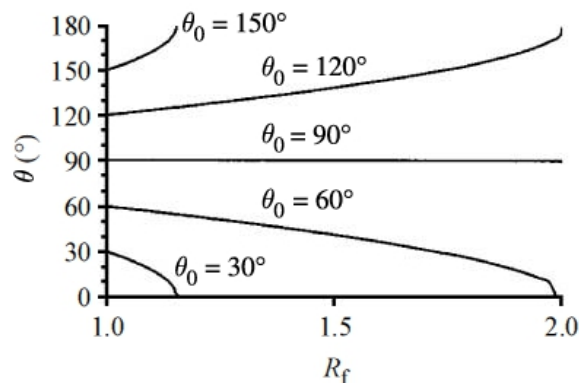


Figure 3.4: CA values for different Young contact angles (θ_0) as a function of the roughness factor R_f according to Wenzel's model.^[30]

As one can see, with increasing roughness factor R_f the measured CA decreases for the hydrophilic surfaces and increases for the hydrophobic surfaces, which is exactly what the Wenzel model predicts. Also shown are the calculated values for three patterned hydrophobic surfaces using the Wenzel equation with the contact angle of the smooth surface as θ_Y . While the measured value corresponds well with Wenzel's theory for the micro-rough lotus replica surface, the measured values for the nanostructured surfaces are somewhat higher than expected. These deviations can probably be ascribed to air pocket formation between the surface asperities. This will be discussed in the next section.

3.3 The Cassie-Baxter State

The second possibility on a rough surface is for the droplet to be suspended on top of the surface asperities, trapping air in isolated cavities below itself. This condition is known as the *Cassie-Baxter* state, after Cassie and Baxter who established the theory in 1944.^[31] It is sometimes also referred to as the "fakir state" because the drop sits on a bed of micronails, as shown in Figure 3.7.

When a water droplet comes to rest at a surface in the Cassie-Baxter state, a solid-air area is replaced by a solid-liquid area. Cassie and Baxter denoted f_1 and f_2 the liquid-solid and the liquid-air fractional area under the droplet, respectively ($f_1 + f_2 = 1$), and they observed that in the process of spreading a water droplet on this surface, an energy $f_1\gamma_{SA}$ is gained in destroying

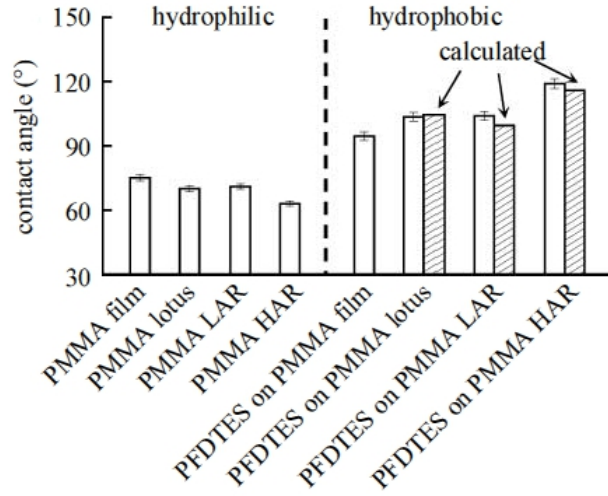


Figure 3.5: Measured contact angles on hydrophilic and hydrophobic surfaces.^[30]

the solid-air interface, while the energies $f_1\gamma_{LS}$ and $f_2\gamma_{LA}$ are expended in forming the new solid-liquid and liquid-air interfaces, respectively.^[31] The net energy expended in the process is, therefore,

$$E_{net} = f_1(\gamma_{LS} - \gamma_{SA}) + f_2\gamma_{LA} . \quad (3.8)$$

Substituting Equation 3.5 into Equation 3.8 one obtains

$$E_{net} = \gamma_{LA}(f_2 - f_1 \cos \theta_Y). \quad (3.9)$$

Since $\gamma_{LS} - \gamma_{SA}$ is the expended energy E in forming the new solid-liquid interface between a water droplet and a flat surface, equation 3.5 can also be written

$$\cos \theta_Y = \frac{-E}{\gamma_{LA}} . \quad (3.10)$$

For a droplet in the Cassie-Baxter state on a rough surface, one can use the following analogy^[31]:

$$\cos \theta_{CB} = \frac{-E_{net}}{\gamma_{LA}} = f_1 \cos \theta_Y - f_2 . \quad (3.11)$$

Here, θ_{CB} is the Cassie-Baxter contact angle, and θ_Y is the "intrinsic" contact angle on a flat surface with the same chemistry, i.e., Young's CA. Equation 3.11 is known as the *Cassie-Baxter* equation, and, as we can see, it reduces

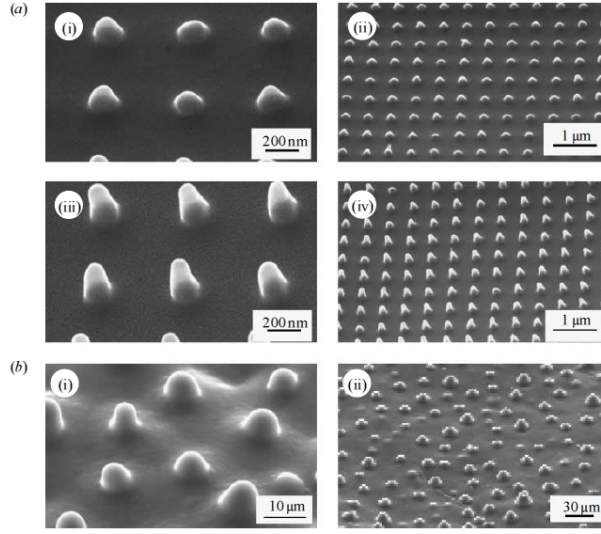


Figure 3.6: SEM micrographs of (a) two nanopatterned surfaces shown at two magnifications; (i)(ii) PMMA low-aspect-ratio (LAR) and (iii)(iv) PMMA high-aspect-ratio (HAR). (b) PMMA surface with a replica of the microstructure of a lotus leaf. [30]

to the Wenzel equation (with roughness factor f_1) when air is not trapped in the valleys between the surface asperities, i.e., when $f_2 = 0$.

A slightly more complex version of the Cassie-Baxter equation is given by [20]

$$\cos \theta_{CB} = r_f f_1 \cos \theta_Y - f_2 . \quad (3.12)$$

This equation applies when the tops of the surface asperities are rounded. The new factor r_f denotes the roughness value of the wet area (see Figure 3.8).

When a water droplet rests on top of the surface asperities, the surface tension is reduced, and this leads to an increase in the CA. The higher the liquid-air fraction f_2 of the area under the droplet, the higher the CA, according to the Cassie-Baxter model. This is true also for surfaces that are intrinsically hydrophilic.

Like the Wenzel model, the Cassie-Baxter model can be modified to describe the three-dimensional pillared structure in Figure 3.3. With $f_1 = a^2/(a+b)^2$ and $A = 1/((b/a) + 1)^2$, the modified equation looks like this:

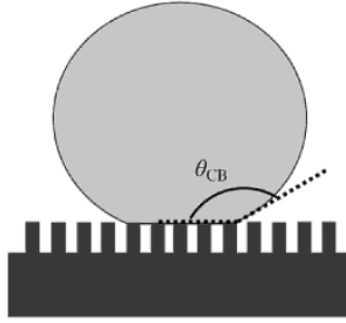


Figure 3.7: Schematic illustration of a droplet in the Cassie-Baxter state.^[19]

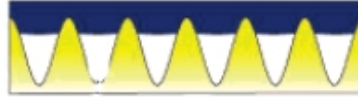


Figure 3.8: Schematic illustration of a droplet in the Cassie-Baxter state where the surface asperities are rounded.

$$\cos \theta_{CB} = A(1 + \cos \theta_Y) - 1. \quad (3.13)$$

This equation shows that high aspect ratio pillars (i.e., high values of b/a for pillars of constant height H and intrinsic contact angle θ_Y) are beneficial for attaining large contact angles.

3.4 Mixed States

To explain water contact angles that correspond neither with those predicted by Wenzel nor with those predicted by Cassie and Baxter, Zheng et al.^[32] proposed a model for a mixed wetting mode, where only a part of the water-air interface has been able to reach down to the bottom of the valleys between the surface asperities:

$$\cos \theta_M = \chi \cos \theta_W + (1 - \chi) \cos \theta_{CB}. \quad (3.14)$$

Here, χ is the fraction of the area that has transitioned to the Wenzel state.

3.5 Controversy Regarding the Wenzel and the Cassie-Baxter Models

Some controversy has been reported on what exactly determines the behavior of the CA on a given surface. The CA is traditionally described as a result of the balance of the liquid-vapor, the solid-liquid, and the solid-vapor interfacial tensions, as shown in Figure 3.9.^[33] According to this line of thought, the

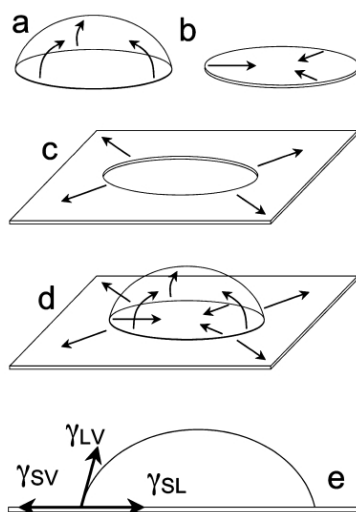


Figure 3.9: Liquid-vapor (a), solid-liquid (b), and solid-vapor (c) interfacial tensions of a three-phase system in equilibrium. Their balance is shown in (d), and the contact angle is the angle between γ_{LV} and γ_{SL} (e).^[33]

solid-liquid contact area is the main factor affecting the wetting. The theories according to Wenzel and Cassie and Baxter suggest that the CA will change if one or more of the three interfacial energies of the system changes. Gao and McCarthy^[33] conducted a simple experiment to show that this is not the case, and that the important factor dictating the wetting behavior is actually the solid-liquid interaction at the three phase (solid-liquid-vapor) contact line. To prove this, they fabricated surfaces containing spots that were either smoother, rougher or chemically different from the surrounding field (see Figure 3.10). Water droplets were then placed within the spot and allowed to expand by adding water through a syringe. The frames in Figure 3.11 show a droplet resting on a superhydrophobic spot on an otherwise non-superhydrophobic surface. The advancing CA was measured to 168° while the droplet was within the spot—as seen in frame (a) to (d)—but

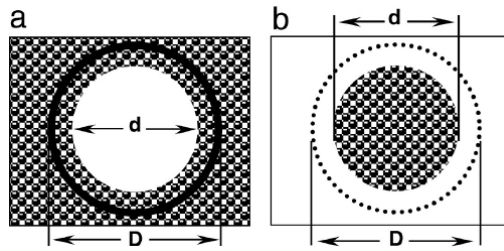


Figure 3.10: Depictions of (a) a smooth spot in a rough field, and (b) a rough spot in a smooth field.^[33]

when it crossed the perimeter to the surrounding smoother region, it quickly decreased to 117° , which we can see in frame (e) and (f).

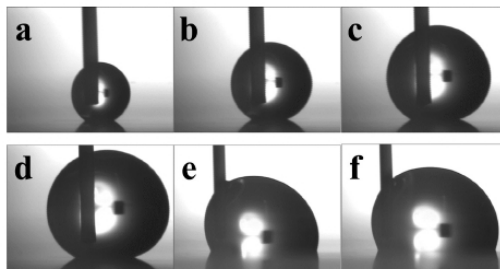


Figure 3.11: Videotape frames showing a water droplet expanding from within a superhydrophobic spot onto a smooth field.^[33]

The opposite effect was observed when the experiment was conducted on a rough surface with a smooth spot on it; the CA was first low, before it suddenly increased to a higher value when the droplet crossed the perimeter.

These experiments show that the Wenzel and Cassie-Baxter models are valid only as long as the surface structure under the droplet reflect that of the three-phase contact line. This is usually the case, however, and in most practical applications the theories according to Wenzel and Cassie and Baxter can still be used.

3.6 Sliding Behavior

3.6.1 Contact Angle Hysteresis and Critical Tilt Angle

When the surface on which a water droplet sits is tilted, its CA will increase and decrease on the downhill side and the uphill side, respectively. The CA on the downhill side is called the *advancing* CA (θ_A), while the CA on the uphill side is known as the *receding* CA (θ_R) (see Figure 3.12). When the tilt angle reaches a critical angle, the droplet will lose its grip and start moving down the plane. The difference between θ_A and θ_R just before the droplet starts moving is termed the *contact angle hysteresis* (CAH).^[29] This value

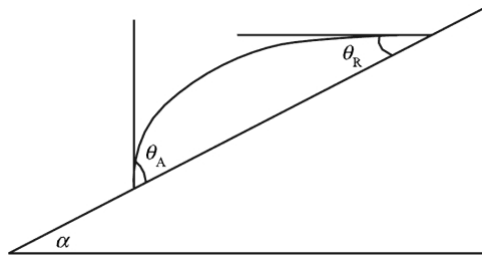


Figure 3.12: Advancing (θ_A) and receding (θ_R) contact angles obtained by tilting the surface at the critical angle α .

gives a measure of how "sticky" the surface is. The higher the CAH, the easier the water droplet will stick to the surface, which means that there is a higher energy barrier as resistance to flow.^[20] The tilt angle at which the droplet starts moving is called the *critical angle*, α . The following relationship between tilt angle and CAH was proposed by Furmidge in 1962:^[34]

$$mg \frac{\sin \alpha}{w} = \gamma_{LV}(\cos \theta_R - \cos \theta_A). \quad (3.15)$$

Here, m is the mass of the droplet, and w is the width of the droplet perpendicular to the direction of motion.

Water droplets can move on a surface either by sliding, rolling, or a mixed propagation.^[33] When a droplet rolls, the only interfacial water molecules that move are those around the three-phase perimeter. These either wet a new surface at the front of the droplet or de-wet a previously wetted surface at the back, as indicated by the open circles shown in Figure 3.13. This mechanism of propagation—which is consistent with the no-slip boundary condition of fluid mechanics^[35]—means that the energy barrier for advancing is much lower than that for receding. To advance, the front molecules of the

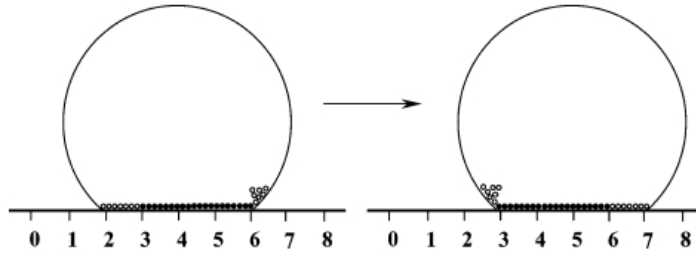


Figure 3.13: A droplet propagating from one position to another. The shaded circles represent water molecules that are in the same position during the process.^[33]

droplet simply need to descend onto the immediate surface ahead of it. To recede, on the other hand, the molecules at the back must disjoin from the surface, something which requires a lot more energy. This energy imbalance is believed to explain the CAH of droplets in the Cassie-Baxter state. It also explains why droplets in the Cassie-Baxter state on rough surfaces have a smaller contact angle hysteresis than do droplets on smooth surfaces, because in the Cassie-Baxter state the solid-liquid contact area is smaller and thus the energy barrier for receding is lower. Water droplets in the Wenzel state usually have a high water CAH, which can be explained by water droplets getting trapped in the surface texture. The droplets thus stick much better to the substrate than do droplets in the Cassie-Baxter state.^[23]

Generally, a decrease in surface roughness R_f will decrease the CAH for droplets in the Wenzel state, while a smaller CAH value can be achieved for droplets in the Cassie-Baxter State by minimizing the liquid-solid fractional interface.^[30]

For water-repellent surfaces we want the CAH and the tilt angle to be as low as possible. In theory, if there is no CAH the droplet will just slid off without dissipating energy as soon as the surface is tilted just a little. In practice, however, there will always be some hysteresis due to friction caused by surface roughness and heterogeneity, but by carefully controlling the roughness on the micro- and nanoscale it is possible to achieve CAHs as low as 1° .^[30]

3.6.2 Effect of Surface Directionality on Sliding Behavior

Yoshimitsu et al.^[36] investigated how surface directionality in the surface microstructure affects the sliding behavior of water droplets. They prepared

various hydrophobic surfaces by dicing aligned pillarlike structures on silicon surfaces and subsequently coating them with fluoroalkylsilane. As expected, the tilt angle was observed to increase with increasing pillar height. More interesting results were found when the sliding behavior of water droplets was studied on a one-dimensional groove structure and compared to the behavior on a pillar-like structure, as can be seen in Figure 3.14a and 3.14b. The

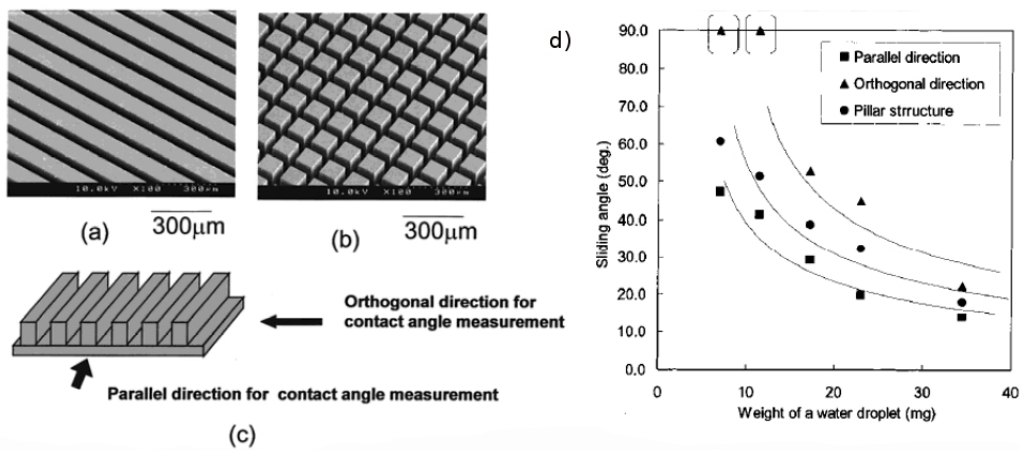


Figure 3.14: SEM micrographs of (a) a one-dimensional groove microstructure, (b) a pillar-like microstructure with the same structural dimensions as the one-dimensional groove structure, (c) a schematic illustration of the sliding directions on the one-dimensional structure, and (d) sliding angle as a function of droplet weight measured on the pillar structure and on the one-dimensional structure in two directions.^[36]

critical tilt angle (or sliding angle) was smaller in the parallel direction on the one-dimensional structure than on the pillar structure, but larger in the orthogonal direction. The sliding angle was observed to decrease with the weight of the water droplet both on the pillar-like and on the one-dimensional surface, as shown in Figure 3.14d.

It seems likely that the sliding behavior is related to the length and continuity of the three-phase contact line on the surface. When water slides in the parallel direction of the one-dimensional structure, it follows a continuous contact line. Turning the surface 90°, on the other hand, will make the contact line discontinuous, as shown in Figure 3.15. This raises the energy barrier for droplet motion in this direction. These results suggest that surfaces on inclined planes may benefit from an anisotropic design to increase their water repellency.

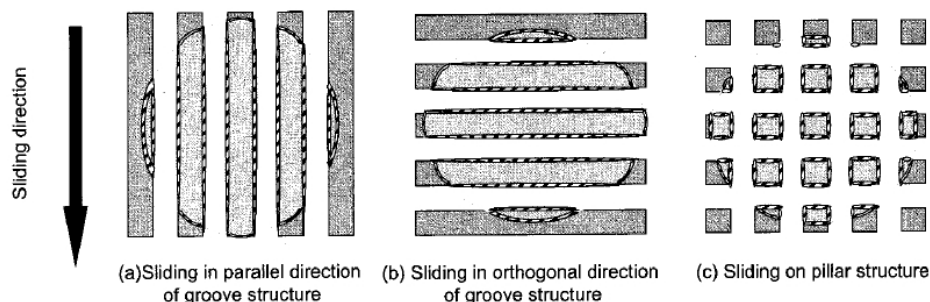


Figure 3.15: Top view of the three-phase contact line on a one-dimensional groove structure surface (a), (b), and a pillar structure (c).^[36]

3.7 Conditions for Superhydrophobicity

Smooth surfaces of many materials are known to exhibit "intrinsic" hydrophobicity with high CAs, e.g. fluorinated polymers and silicon resins.^[23] But as mentioned earlier, to increase the surface roughness above 120° and to reduce its CAH to very low values, it is necessary to introduce surface roughness. Thankfully, nature has already paved the way and provided us with many materials with superhydrophobic properties that we can learn from.

Among the creatures in nature that exhibit extreme water-repellent properties, the self-cleaning lotus plant (*Nelumbo nucifera*) is probably the most famous example. Neinhuis and Barthlott explained in 1997 how the lotus leaf owes its superhydrophobicity to a surface with *dual-scale* roughness. The surface consists of micro-asperities formed by so-called papillose epidermal cells in addition to nano-protrusions introduced by a low-energy (hydrophobic) tubular epicuticular wax (see Figure 3.16).^[30]

Water droplets on lotus leaves are in the Cassie-Baxter state, which is clearly demonstrated by measured static CAs as high as 164° ^[37] (well above the 150° threshold for a superhydrophobic surface). Water droplets on lotus leaves bead up and form spherical droplets, and roll easily off leaves that are slightly inclined. As water droplets roll down the leaves, they tend to drag dust, insects and contamination particles along on their way, leaving behind a clean and dry surface (see Figure 3.17).^[29] This unique property is referred to as *self-cleaning*. Due to its ability to remain clean in murky ponds, many cultures revere the lotus plant as a symbol of cleanliness and purity.

Pond skaters (*Gerris remigis*) are another species that have remarkable superhydrophobic properties. They are able to stand and walk stably on

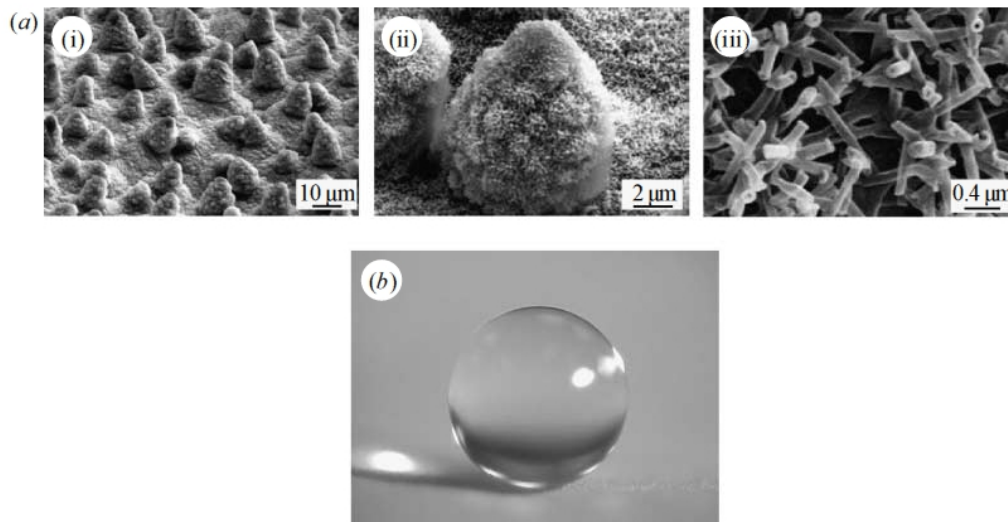


Figure 3.16: (a) SEM micrographs of the surface of a lotus leaf at three magnifications. (b) A water droplet resting on the surface of a lotus leaf.^[30]

water without breaking through the surface, even in heavy rain and rushing currents. Careful investigation of these freshwater bugs has revealed a micro-nano hierarchical structure on their legs, consisting of fine nanogrooves superimposed on tiny microsetae (hairs).^[38] The microstructure and nanostructure are shown in the SEM micrographs in Figure 3.18b and 3.18c, respectively. This topography in combination with a secreted hydrophobic cuticle wax is the secret behind the pond skater's ability to resist water.

The same conclusion can be drawn after investigating several other superhydrophobic materials in nature, including plants,^[39] insects^[40] and animals:^[41] The best water-repellency is obtained with a combination of a hydrophobic chemistry and a hierarchical topography in which a nanostructured texture/roughness is superimposed on a microstructure. Contact angles larger than 150° can be induced on surfaces comprising a microscale only or a nanoscale only texture, but the CAH (and the critical sliding angle) will in these cases be quite large (often higher than 30° ^[29]). To obtain a surface with both θ_A and θ_B greater than 150° in addition to low CAH, a complex hierarchical structure like the one shown in Figure 3.19 is necessary. Such a surface can reduce the critical sliding angle of a same-sized drop by a factor of ten.^[29]

This hypothesis was confirmed by Bhushan et al.^[30] who fabricated flat, nanostructured, microstructured and hierarchically structured surfaces cov-

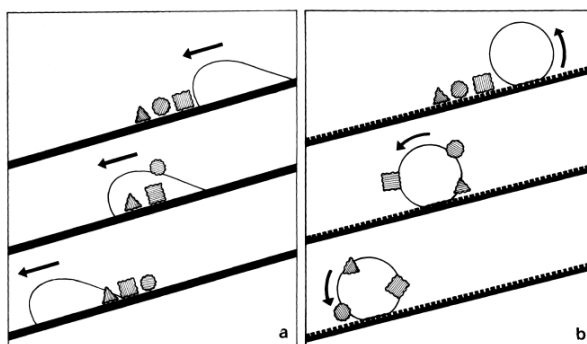


Figure 3.17: The movement of a water droplet down a tilted smooth (a) and a rough (b) surface. On the smooth surface, the droplet redistributes the particles. On the rough surface, the particles adhere to the surface of the water droplet as it rolls down, and they are entirely removed from the surface.^[25]



Figure 3.18: (a) A pond skater resting on water. (b) SEM image of a pond skater leg covered with micro-sized hairs. (c) SEM image of nanogrooved structure on the hairs.^[38]

ered with *n*-hexatriacontane, and studied the influence of the different structures on the static CA and CAH. SEM micrographs of the surfaces are shown in Figure 3.20.

The roughness factor R_f was calculated based on geometrical considerations (for the microstructure) and measured using an AFM (for the nanostructure). For the nano-, micro- and hierarchical structure the roughnesses were 4.9, 3.5 and 8.4, respectively. The corresponding values of f_2 were 0.85, 0.71 and 0.96. The measured values of the static CA and the CAH are shown graphically in Figure 3.21, together with calculated values according to the Wenzel and Cassie-Baxter theories.

Even if the results suggest that all the three structured surfaces were in the Cassie-Baxter state, the hierarchical structure performed best by far, having both the largest CA and the lowest CAH. With a measured CA of



Figure 3.19: a) A simple microtextured surface. b) A complex nano-micro hierarchically textured surface.^[29]

169° and a CAH of 2°, it was the only surface to satisfy the requirements for superhydrophobicity. These values are actually superior to CA and CAH values measured on the lotus leaf. The runner-up in this "race" was the nanostructure, followed by the microstructure. The flat surface finished last. The tilt angle and the adhesion force also proved to be significantly lower on the hierarchically structured surface.

A microstructure with a superimposed nanostructure ensures that the mechanical structure and the superhydrophobicity is stable. According to Nosonovsky and Bhushan,^[30] the function of the micro-roughness in a dual-scale texture is to resist capillary waves by providing mechanical stabilization. The microstructure allows the nanoscale pillars to have lower height and lower density than if the nanopillars were to yield the same apparent contact angle alone. This requirement for Euler stability will be covered in Section 4.4.

The nano-roughness functions to prevent liquid from entering the gaps between the surface asperities by pinning the liquid droplets, in addition to supporting nanodroplets which may otherwise condense between the high asperities.

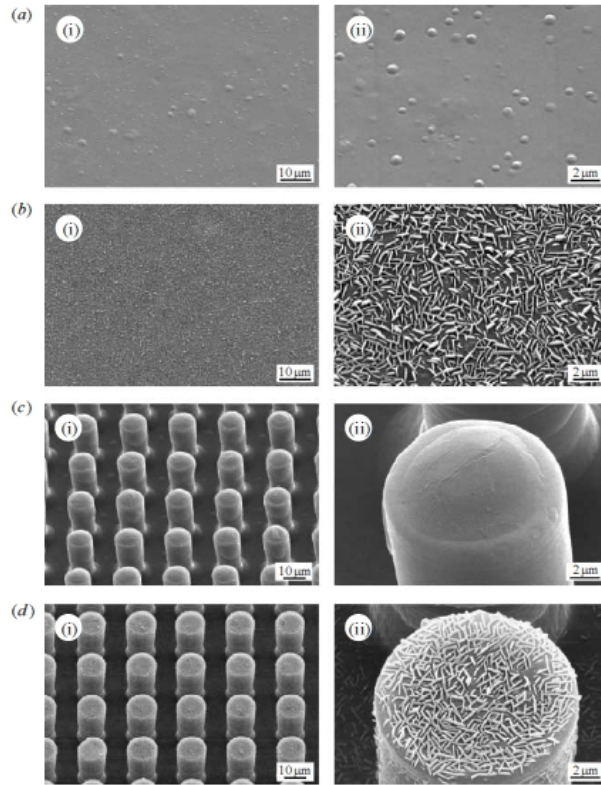


Figure 3.20: SEM micrographs in two different length scales of a flat (a), a nanostructured (b), a microstructured (c) and a hierarchically structured (d) surface covered with $0.2 \mu\text{g mm}^{-2}$ of *n*-hexatriacontane.^[30]

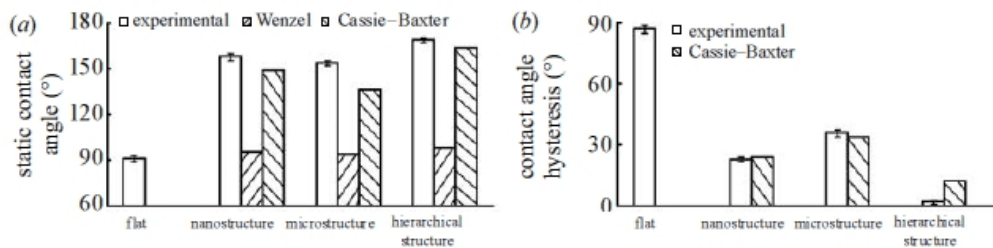


Figure 3.21: Bar charts showing the measured values of CA and CAH on four different surfaces, in addition to calculated values using both the Wenzel and the Cassie-Baxter equation.^[30]

Chapter 4

Stability of the Cassie-Baxter State

Both the Cassie-Baxter state and the Wenzel state represent energy equilibrium positions, but while one of the states (usually the Wenzel state) represents a *global* energy minimum, the other state represents a *local* minimum, and the latter is therefore only a *meta-stable* position.^[22]

In all transitions between different energy minima, the interface between the droplet and the surface must overcome an energy barrier. Which of the two configurations (or possibly an intermediate state) that is attained depends on a number of factors in addition to surface roughness, such as pressure, vibration, humidity, texture, droplet size and how the water droplet is transferred to the surface^[23]). For example, when water droplets are gently deposited on the pillar tops of a superhydrophobic surface, the energy barrier is often too large to be overcome, and the surface will remain in the Cassie-Baxter state (the local energy minimum). If the water droplet is produced by vapor condensation, on the other hand, or if the water droplet impinges on the structured surface with kinetic energy and/or is subjected to vibration or electrical energy, then the Wenzel state is more likely to materialize.^[20]

The goal is to find ways to prevent transition from the Cassie-Baxter state to the Wenzel state. Intensive research has been conducted over the last years to identify the different wetting-mode transition mechanisms. In the following, the effect of various surface parameters on the stability of the Cassie-Baxter state will be reviewed.

4.1 Effect of Roughness and Solid-Liquid Fractional Interface

Although the Wenzel state is generally expected to occur on surfaces with low to moderate roughness and the Cassie-Baxter state is more likely to appear on highly rough surfaces, there is no definite limit by means of which to separate the two states. The two states have indeed been observed to co-exist on hydrophobic surfaces of moderate roughness ($R \approx 2$).^[19] A general rule can be found, however, by equating the Wenzel equation and the Cassie-Baxter equation. This yields the following *critical Young's contact angle*:^[42]

$$\cos \theta_{Y,c} = \frac{f_1 - 1}{R_f - f_1}. \quad (4.1)$$

When θ_Y is larger than $\theta_{Y,c}$, then the Cassie-Baxter mode represents the lowest energy minimum. On surfaces with moderate Young CA, i.e., $90^\circ < \theta_Y < \theta_{Y,c}$, the lowest energy is attained in the Wenzel state. This does not mean that the Cassie-Baxter state is impossible in this region, but rather that the configuration is meta-stable. This relationship is graphically represented in Figure 4.1, where the dotted line indicates the metastability.

4.2 Effect of Curvature

Using the Lagrange method, Nosonovsky^[43] derived a stability condition based on free energy minimization, which explains why curved surface structures are particularly good at resisting transition from the Cassie-Baxter to the Wenzel state. When the liquid-air interface advances down a curved surface pillar (see Figure 4.2), the CA under the droplet changes, and this is accompanied by a change in energy^[43]

$$dW = dA_{SL}\gamma_{LA}(\cos \theta - \cos \theta_0), \quad (4.2)$$

where dA_{SL} is the change in solid-liquid contact area, and $\theta - \theta_0$ is the change in CA. On a concave/grooved surface, an advancing liquid-air interface leads to an increase in the CA. The energy therefore decreases according to Equation 4.2, so that it is energetically favorable for the liquid to advance. On a convex/bumpy surface, on the other hand, an advancing liquid-air interface results in a decrease in the CA, making it energetically profitable for the liquid to retreat. The result is a stable energy equilibrium that can pin the liquid-air interface.

The effect of surface curvature on liquid repellency was utilized by Tuteja et al.^[44] Organic liquids such as octane have a much lower surface tension

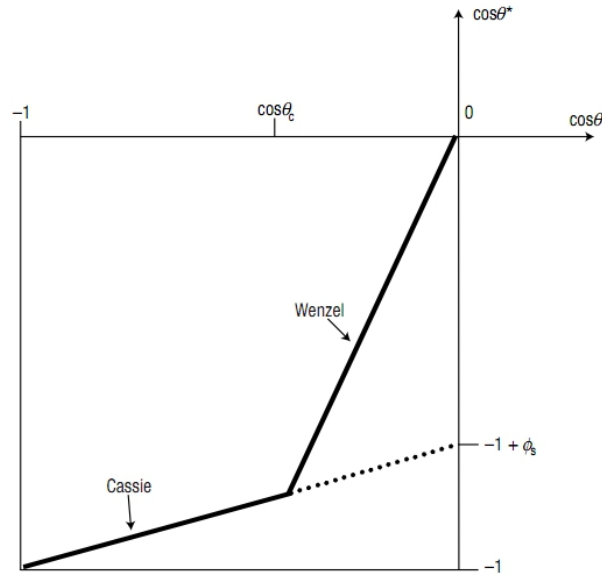


Figure 4.1: The cosine of the apparent contact angle θ^* plotted as a function of the cosine of the Young CA, here denoted by θ . The drawn lines represent the CAs predicted by the Wenzel and the Cassie-Baxter models. The Cassie-Baxter state is expected to be energetically favored when the Young CA is larger than the critical value θ_c .^[42]

than has water ($\gamma_{LA} = 21.6$ mN/m vs $\gamma_{LA} = 72.1$ mN/m), making it much harder to obtain high contact angles. Using a surface coated with curved fibers, the research group was able to overcome these problems, creating textured surfaces that displayed CAs greater than 160° . It should be mentioned that the Cassie-Baxter state was metastable, as separate experiments showed that droplets released from a height were able to penetrate and wet the surface asperities.

The surfaces were produced by electrospinning fibers made from a mixture of PMMA and fluorinated polyhedral oligomeric silsesquioxane (fluoro-POSS) on a silicone surface. FluoroPOSS has a very low surface energy, and the results did indeed show that both the advancing and the receding CA increased with increasing mass fraction of this synthetic fiber, as shown in Figure 4.3a. An abrupt transition from the Wenzel state to the Cassie-Baxter state was observed at an equilibrium contact angle of about 69° by plotting the advancing CA on the electrospun surface against the advancing CA on a corresponding spin coated surface, as shown in Figure 4.3b.

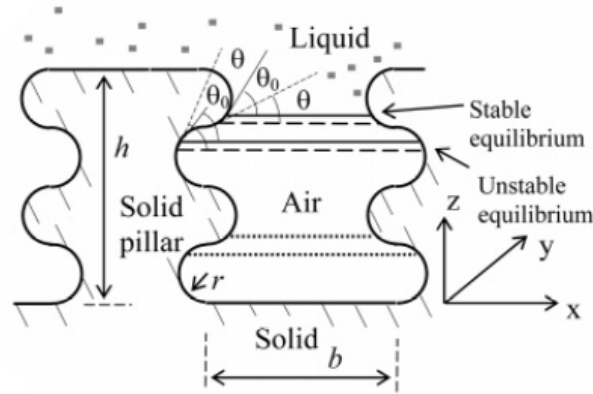


Figure 4.2: Two-dimensional pillars with semicircular bumps and grooves. An advancing liquid-air interface down along the bumps causes the CA to decrease, thereby giving rise to stable equilibria and the ability to pin the triple line. An advancing liquid-air interface down along the grooves leads to a CA increase. The equilibria are unstable, and the triple line will not be pinned.^[43]

Tuteja et al. ascribed the observed liquid repellency to the local surface curvature of the electrospun fibers, which ensures that there is a point at which the Cassie-Baxter state is locally stable. They therefore suggested that one should consider surface curvature as an important factor in conjunction with surface roughness and wetted surface fraction when designing surfaces with very high resistance to wetting. The structure in Figure 4.4 is a side view of what might serve as an ideal hierarchical surface structure with bumpy geometry, according to Bhushan and Jung.^[30]

4.3 Effect of Pillar Height, Pillar Diameter, Pillar Slenderness and Inter-Pillar Pitch

Yoshimitsu et al.^[32] fabricated pillared microstructures on silicon wafers coated with fluoroalkylsilane. The Young CA was measured to 114° . Average CA values were then measured for a 1 mg water droplet resting on surfaces with pillar heights $H = 10, 36, 148, \text{ and } 282 \mu\text{m}$, while the pillar width and groove width were kept constant at $a = 50 \mu\text{m}$ and $b = 100 \mu\text{m}$, respectively. Schematics of the structures are shown in Figure 4.5(a) and (b). The corresponding measured average CA values were $138^\circ, 155^\circ, 151^\circ, \text{ and } 153^\circ$, respectively. With structural parameter $f_1 = a^2/(a + b)^2 = 1/9$,

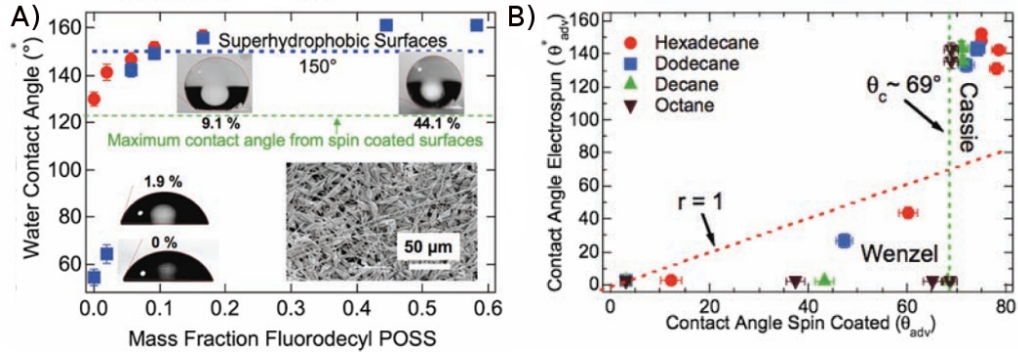


Figure 4.3: (a) Advancing (red dots) and receding (blue squares) CAs for water on electrospun surfaces, as a function of mass fraction of fluoroPOSS. (b) Master curve showing the advancing CA on electrospun surfaces as a function of advancing CA on spin-coated surfaces of the same material, for various liquid alkanes.^[44]

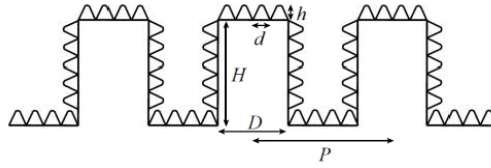


Figure 4.4: A proposed ideal hierarchical structure consisting of microsized asperities of diameter D and height H , separated by a center-to-center distance P . Superimposed on the micro-asperities is a nanostructure with pyramidal tops of diameter d and height h .^[30]

$r_f = 1$ (i.e., no nano-roughness), and $R = 1 + 4aH/(a + b)^2$, equation 3.12 predicts a contact angle of $\theta_{CB} = 159^\circ$ for the Cassie-Baxter mode, which corresponds fairly well with the measured values for pillar heights of $36 \mu\text{m}$ and above. The measured CA of 138° for $H = 10 \mu\text{m}$, on the other hand, does not fit neither the Cassie-Baxter model nor the Wenzel model (which predicts $\theta_W = 116^\circ$ for $H = 10 \mu\text{m}$), so it probably indicates that the droplet is in a mixed state as explained in Section 3.4.

These results indicate a shift from Wenzel to Cassie-Baxter mode with increasing pillar height, and with a transition regime where the measured CAs are of intermediate values.

Consider the pillared structure in Figure 4.6. On such a surface, transition to the Wenzel regime will occur if the maximum droop δ of the droplet—

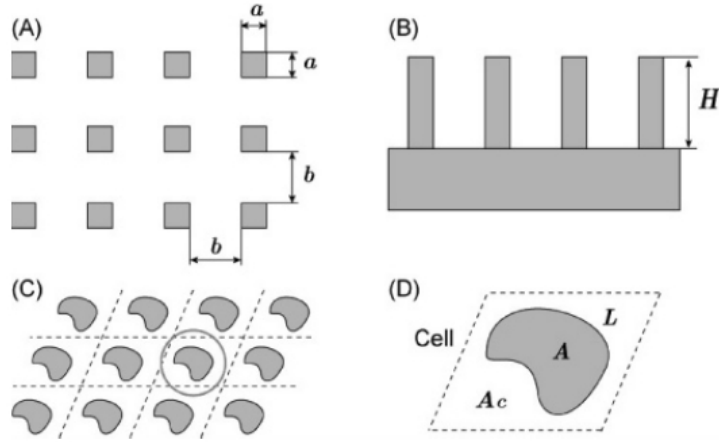


Figure 4.5: Top view (a) and side view (b) of the square pillar-like microstructured surface used in the experiment of Yoshimitsu et al.. Top view (c) of pillars with an irregular cross section, and "cell" containing a single selected pillar (d).

which is located at the midpoint between two diagonally adjacent pillars—is significantly greater than the pillar height H . According to Bhushan et al.,^[30] the droop is given by $\delta = (\sqrt{2}P - D)^2 / (8R)$, so that the criterion for Cassie-Baxter-to-Wenzel transition can be formulated as^[30]

$$\frac{(\sqrt{2}P - D)^2}{R} \geq H, \quad (4.3)$$

where P is the pitch (the distance between the centers of two adjacent pillars), D is the pillar diameter, and R is the droplet radius.

Bhushan and Jung measured the CA on Si surfaces coated with PF_3 and plotted the CA as a function of P to explore the effect of the pitch size on the Cassie-Baxter-to-Wenzel transition.^[30] The plot is shown in Figure 4.7a. The flat PF_3 surface has a CA of 109° . As asperities were introduced, a sudden jump to 152° was observed. The CA continued to increase with the pitch size until a maximum value of 170° was reached for $P = 45 \mu\text{m}$. Then the CA value dropped sharply, as a consequence of regime transition. This happened at ca. $50 \mu\text{m}$, which is somewhat earlier than expected according to equation 4.3, represented by the dotted line.

The CAH and critical tilt angle were also measured on the same surfaces, and plotted against the pitch size, as shown in Figure 4.7b. A relatively small initial increase in the CAH and tilt angle was observed as micropillars were introduced, probably attributed to pinning of the droplet at the edges

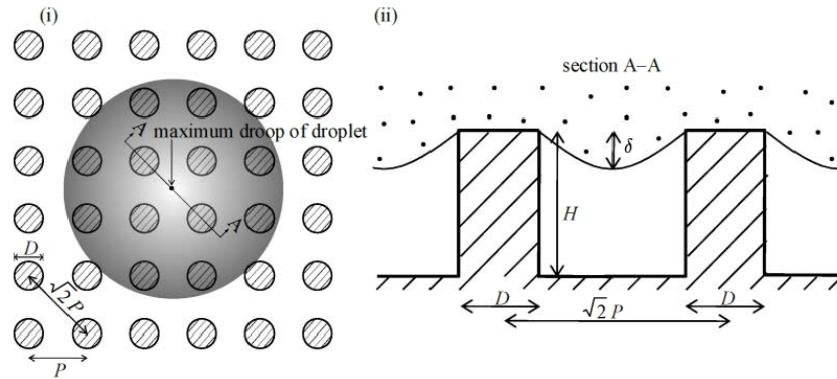


Figure 4.6: (i) Top view of a liquid droplet resting on a regular microstructure of circular pillars. (ii) Cross-section view of the cross-section A-A in (i).^[30]

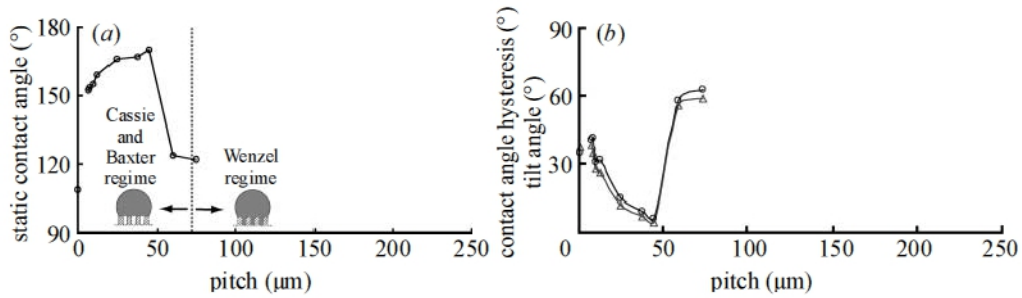


Figure 4.7: (a) CA vs. pitch. The dotted line represents the predicted critical pitch size according to Equation 4.3. (b) CAH vs. pitch.^[30]

of the micropillars. As the pitch increased, the contact area between the patterned surface and the droplet decreased and so did the density of sharp edges. As a result both the CAH and the tilt angle values started to decline until minimum values were observed on surfaces with $45 \mu\text{m}$ pitch. These values were 5° and 3° for the CAH and tilt angle, respectively. Both CAH and tilt angle then increased sharply because of regime transition.

Zheng et al.^[32] numerically simulated the transition from the Cassie-Baxter to the Wenzel state on periodical pillar-like structures with different cross sections. An example of a non-square cross-section is shown in Figure 4.5c. They assumed that the surface of the pillar structures and the base surface were made of the same material, and the pillar tops were assumed

to be flat ($r_f = 1$). Such a surface can be divided into cells of area A_c surrounding each pillar, as shown in Figure 4.5d. Denoting the cross sectional area, the height and the perimeter of the pillars by A , H and L , respectively, Zheng et al. defined the *slenderness ratio* as^[32]

$$\eta = \frac{HL}{A}. \quad (4.4)$$

Based on calculations involving the Gibbs free energy of small water droplets on a surface, it turns out that the Cassie-Baxter state is stable and the Wenzel state is metastable or unstable when the slenderness ratio of the surface is larger than the so-called *equi-energy* slenderness ratio^[32]

$$\eta_e = -\frac{1 - f_1}{f_1} \frac{1 + \cos \theta_Y}{\cos \theta_Y}. \quad (4.5)$$

If θ_Y , f_1 , L and A are known, then one can calculate η_e and find the required pillar height H_e for stable Cassie-Baxter mode using Equation 4.4:^[32]

$$H_e = -\frac{1 - f_1}{f_1} \frac{1 + \cos \theta_Y}{\cos \theta_Y} \frac{A}{L}. \quad (4.6)$$

When $H < H_e$, then the Wenzel mode is more stable than the Cassie-Baxter mode. When $H > H_e$, then the Cassie-Baxter mode is more stable.

4.4 Effect of Pillar Rigidity

The stability of the Cassie-Baxter state also requires *Euler stability*, which means that the surface asperities must have resistance to buckling when water droplets are applied on them.^[45] The theory in Section 4.3 predicts ever increasing Cassie-Baxter stability with increased slenderness ratio, but in reality this is impossible. What the model does not take into consideration is the fact that more slender structures can sustain lower pressures. This means that there must be a trade-off between Cassie-Baxter stability induced by high slenderness, and Euler stability induced by the thickness of the surface structures.

When a force F is applied axially on a pillar, it tends to induce buckling, as indicated in Figure 4.8. This is what we call *Euler instability*. In 1757, Leonard Euler derived a formula for the critical load above which a long, slender pillar will start buckling:^[45]

$$F_{cr} = \frac{\pi^2 EI}{4H^2}. \quad (4.7)$$

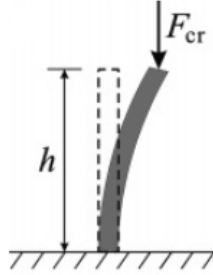


Figure 4.8: An axially applied force makes a pillar Euler-unstable when it exceeds a critical value F_{cr} .^[45]

Here, E is the Young's modulus, I is the moment of inertia, and H is the height of the pillar. Above F_{cr} the pillar will be in a state of unstable equilibrium; even the slightest lateral force will cause the pillar to fail by buckling.

The force acting on the pillar can be written as $F = pA_0 = pA/f_1$, where p is the pressure, A_0 is the area shared by each individual pillar on the surface, A is the cross-section area of the pillar, and $f_1 = A/A_0$ is the area fraction. Using this, Equation 4.7 can be transformed to an expression for the critical pressure:^[45]

$$p_{cr} = \frac{f_1 \pi^2 EI}{4h^2 A} = \frac{\alpha f_1 \pi^2 E}{4\eta^2}. \quad (4.8)$$

Here it is used that $(h^2 A)/I$ is proportional to η^2 , with the proportionality constant $\alpha = 3/4$ and $\alpha = 1$ for square and cylindrical pillars, respectively. The equation reflects the aforementioned fact that more slender pillars (i.e., pillars with high η) can sustain lower pressure. The pressure may be caused by impinging rain droplets, gravity, surface tension, or a combination. Rain impact can cause water droplet pressures as high as 10^5 Pa.^[45] When the required critical pressure is known, one can adjust the other parameters to fulfill equation 4.8.

4.5 Effect of Immersion in Water

Arianpour^[15] tested the wetting behavior on hydrophobic surfaces that had first been immersed in DI water and then withdrawn from the liquid and blown dry with N_2 gas. The samples used were roughened Al substrates covered with nanoparticle-incorporated silicon rubber. The results revealed declining CA values with the immersion time. The surfaces were also periodically annealed overnight to get rid of water that was impossible to remove

by drying in N_2 . This caused the CA to bounce to significantly higher values again, but never as high as in the preceding cycle, as can be seen in Figure 4.9. The mechanism behind the observed deterioration is not yet clear.

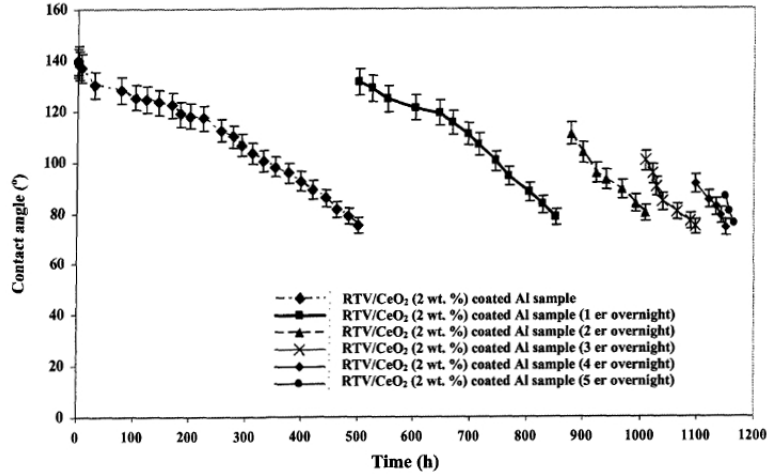


Figure 4.9: Observed CAs on a rough Al substrate coated with silicon rubber incorporated with 2 weight% CeO_2 nanopowder. [15]

4.6 Effect of Droplet Size

The size of the water droplets also has an effect on the stability of the Cassie-Baxter state, as suggested by Equation 4.3. Jung and Bhushan^[30] conducted a series of evaporation experiments on patterned Si surfaces coated with PF_3 and observed for which droplet size transition to the Wenzel regime took place as a function of the pitch (see Figure 4.10). The diameter and height of the pillars were kept constant at 5 and 10 μm , respectively. The first three successive photographs in Figure 4.10a show the droplet in the Cassie-Baxter state. In photograph (iv), transition to the Wenzel state has occurred. The transition happened when the pitch was 37.5 μm and the droplet radius was 360 μm . The regime transition is indicated both by the change in droplet shape with corresponding decreased CA, and by the air gaps that can be observed under the droplet in photograph (i) to (iii), but not in photograph (iv). The graph in Figure 4.10b also includes a solid line which corresponds with the expected critical radius of impalement according to equation 4.3. Even if there is a quantitative deviation between the theory and the measured values, the qualitative agreement is fairly good. The reason

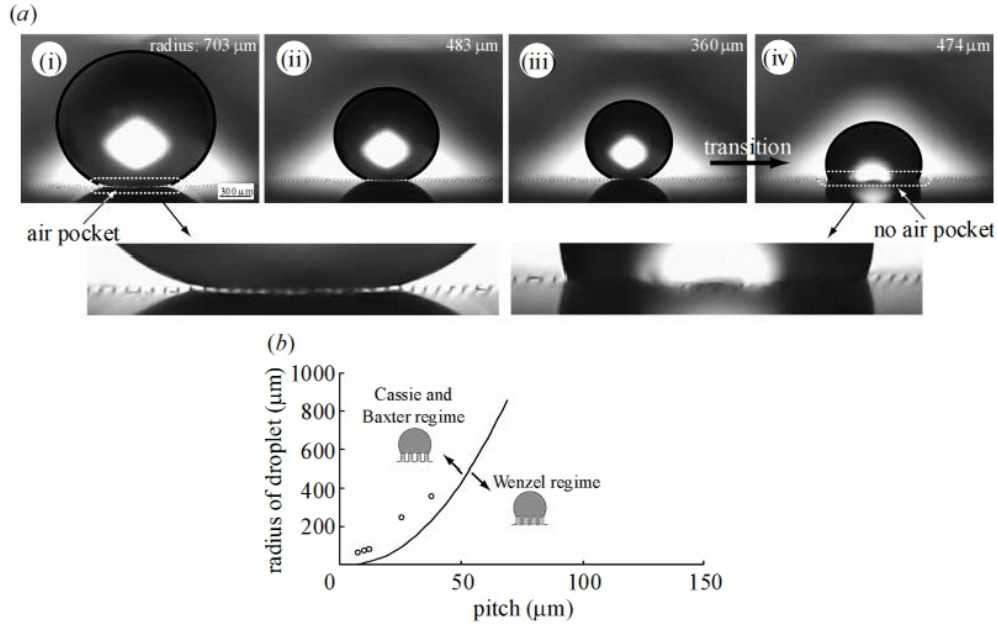


Figure 4.10: (a) Evaporation of a water droplet on a patterned Si surface. Transition to the Wenzel regime takes place between photographs (iii) and (iv). (b) Droplet radius at the time of transition as a function of the pitch size. The line represents the predicted values according to equation 4.3.^[30]

for the droplet transition is that the maximum possible height separating the liquid-air interface from the bottom of the valleys between the asperities diminishes as the curvature of the droplet increases.

4.7 Effect of Roughness Scale and Cross-Sectional Geometry

The roughness scale of a surface, S , is defined as^[46]

$$S = \frac{A}{L}, \quad (4.9)$$

where A is the area of the pillar tops and L is the length of circumference of the pillars. For example, for a surface consisting of square pillars as shown in Figure 4.11, the roughness scale is

$$S = \frac{a^2}{4a} = \frac{a}{4}. \quad (4.10)$$

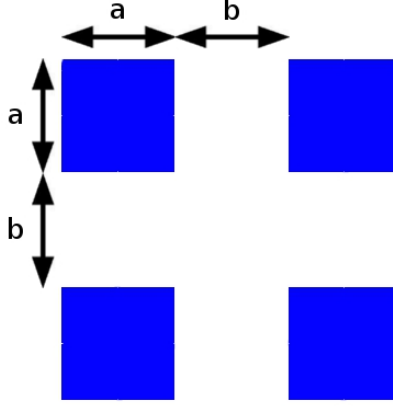


Figure 4.11: Top view of a surface consisting of square pillars.

As the roughness scale shrinks, the total length L_T of the triple-phase intersection lines per unit of apparent contact surface area, increases according to^[46]

$$L_T = \frac{f_1}{S} \quad (4.11)$$

This means that if the dimensions for the surface in Figure 4.11 are $a = b = 1$ mm, then $f_1 = 0.25$, $S = 0.25$ mm, and the total length of the triple-phase intersection lines on a 1 m² surface will be 1000 m. If f_1 is kept constant, but the dimensions are reduced to $a = b = 100$ μ m, then L_T amounts to $10,000$ m on a surface of the same size. Hence, the total line energy $L_T\lambda$, where λ is the line tension, also increases, and hence one expects larger contact angles.

Zheng et al.^[46] modified the Cassie-Baxter equation by taking into consideration the effect of scaling down the size of the surface topography. The new equation looks like this:^[46]

$$\cos \theta_{CB} = -1 + (1 + \cos \theta_Y) \left(1 - \frac{l_{cr}}{S}\right) f_1. \quad (4.12)$$

Here, l_{cr} is an intrinsic or chemical length given by $l_{cr} = \lambda / (\gamma_{LA} + \gamma_{SA} - \gamma_{SL})$. The new introduced factor $(1 - l_{cr}/S)$ becomes increasingly more significant as the roughness is scaled down and/or the shape of the pillar cross-section

is made more complex. This results in increasing CAs as the value of S approaches the critical value l_{cr} , as confirmed by the graph in Figure 4.12, where

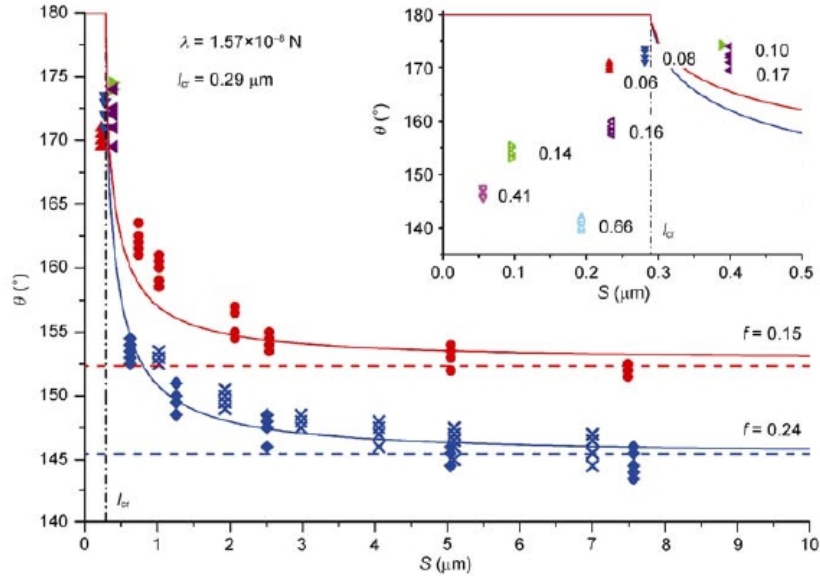


Figure 4.12: Measured CAs as a function of the parameter $S = A/L$. Red dots represent CAs on surfaces with $f_1 = 0.15$ and square-shaped pillars. Blue diamonds represent CAs on surfaces with $f_1 = 0.24$ and square-shaped pillars. Blue crosses represent CAs on surfaces with $f_1 = 0.24$ and X-shaped pillars. The horizontal dashed red and blue line represent the predictions according to the standard Cassie-Baxter equation. The solid lines represent the predictions according to Equation 4.12, with $l_{cr} = 0.29$. The graph in the inset shows measured CAs and respective f_1 values for eight pillar-structured surfaces with S near or smaller than l_{cr} .^[46]

measured CAs on pillar-like structures of different cross-sectional shapes are plotted as a function of S . The data shows an excellent fit to the relationship predicted by Equation 4.12 with l_{cr} set to 0.29. When S was lower than l_{cr} , the CAs quickly decreased, as shown in the inserted graph. This may possibly be explained by the presence of forces from adjacent pillar tops that pull on the water droplets.

Zheng et al. also tested the dynamic behavior of water droplets on square pillared surfaces as a function of the previously introduced parameter S . Both the bouncing height and the number of bounces increased with decreasing S when f was kept constant at ca. 0.15.

Öner and McCarthy^[35] measured the CAH on pillared surfaces with pillars of different cross-sectional shape: squares, indented squares, stars, and staggered rhombi (see Figure 4.13). No significant variation was found for

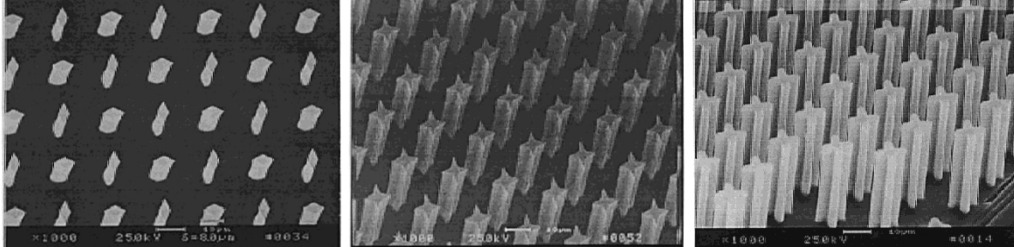


Figure 4.13: SEM micrographs of surfaces tested by Öner and McCarthy.^[35]

the advancing CAs. However, the receding CAs were raised by as much as 22° when the squares were replaced by rhombi. Consequently, the CAH also decreased. The observation can be explained by longer three-phase contact lines.

According to Zheng et al.,^[32] the maximum sustainable hydraulic pressure can be increased by replacing the square pillars with pillars with longer perimeters. Since the force applied by the hydraulic pressure acts on the sidewalls of the pillars through the three-phase contact line, and the sidewall area is proportional to the pillar perimeter L , then the critical pressure will increase linearly with L . The precise expression for the critical hydraulic pressure according to Zheng et al. is

$$p_c = -\frac{\gamma f_1 \cos \theta_Y L}{f_2 A}. \quad (4.13)$$

4.8 Effect of Pressure and Droplet Velocity

It has been shown that even the potential energy of the droplet due to gravitation can be sufficient to make it energetically favorable for the droplet to penetrate into the valleys of the surface roughness, thus causing irreversible transition from the Cassie-Baxter to the Wenzel mode and ruining the superhydrophobicity.^[32] When we know that the impact of rain drops may cause pressures as high as 10^5 Pa, it should be clear why it is crucial to design superhydrophobic surfaces that can resist pressure.

Jung and Bhushan carried out experiments to reveal the effect of pitch size on the *dynamic* behavior of bouncing water droplets on superhydrophobic

surfaces like the one illustrated in Figure 4.6.^[30] As long as the dynamic pressure of the droplet is less than the Laplace pressure, transition to the Wenzel regime will not occur. The Laplace pressure can be expressed as^[30]

$$p_L = \frac{2\gamma_{LA}}{R} = \frac{16\gamma\delta}{(\sqrt{2}P - D)^2}. \quad (4.14)$$

An equation for the dynamic pressure of the droplet is^[30]

$$p_d = \frac{1}{2}\rho V^2, \quad (4.15)$$

where ρ is the mass density of the liquid droplet and V is its velocity. By equating these two expressions, one can derive an expression for the critical velocity at which the droplet touches the bottom, and below which transition will not occur:

$$V = \sqrt{\frac{32\gamma H}{\rho(\sqrt{2}P - D)^2}}. \quad (4.16)$$

Figure 4.14 shows successive photographs of droplets hitting the surface in the experiments of Jung and Bhushan. Series (i) shows a droplet with

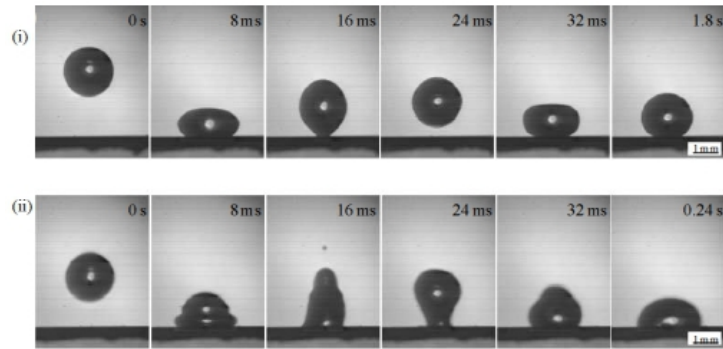


Figure 4.14: Successive snapshots of a 1 mm radius water droplet hitting a microstructured Si surface coated with PF_3 at 0.44 m s^{-1} and 0.88 m s^{-1} .^[30]

impact velocity 0.44 m s^{-1} and series (ii) one with impact velocity 0.88 m s^{-1} , which is the critical velocity. As can be seen, the droplet with the lower velocity first expands rapidly, then retracts due to the hydrophobicity of the surface, and subsequently bounces off the surface. The droplet bounces several times, and when it finally comes to a rest, its CA is high, indicating Cassie-Baxter state. The droplet with the higher velocity, on the other

hand, sticks to the surface before it is able to retract completely. The CA is low, indicating the wetted Wenzel state. The experiment was repeated with different impact velocities and with different pitches to find the critical velocity as a function of pitch size. The results are plotted in Figure 4.15. The

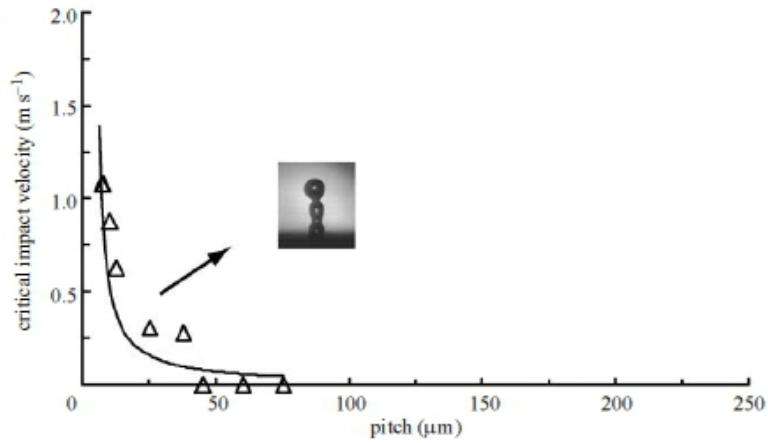


Figure 4.15: Measured values of the critical impact velocity (triangles) as a function of pitch size. The solid line is the predicted results according to Equation 4.16.^[30]

solid line represents the predicted behavior according to Equation 4.16. As we can see the quantitative match between the measured and the predicted behavior is good. Surfaces with low pitch are able to resist droplets with high velocities, but the critical impact velocity decreases exponentially with increasing pitch. The surface tension γ and the liquid mass density ρ were taken as 0.073 N m^{-1} and 1000 kg m^{-3} , respectively.

Bartolo et al.^[47] conducted a similar experiment where they studied the behavior of water droplets impinging on hydrophobic surfaces microfabricated using classical soft-lithography molding on a PDMS silicon elastomer. The group found that for a given surface, there is a certain range of impact velocities within which bouncing occurs, $V_{LB} < V_I < V_{UB}$, where V_I is the impact velocity, and V_{LB} and V_{UB} are the lower and upper boundaries, respectively. For velocities smaller than V_{LB} , the droplet will weakly expand, then retract and finally come to rest in the Cassie-Baxter state without bouncing. This is called the non-bouncing regime. For velocities above V_{UB} , the kinetic energy is so high that the surface structure impales the droplet, preventing it from expanding, and the droplet will stick to the surface. This is called the sticky regime.

Within the bouncing regime, the droplet's contact time with the surface is

independent of the impact velocity, as shown in Figure 4.16a. In Figure 4.16b the impact energy is plotted as a function of the pillar height for a surface with pillar radius $11 \mu\text{m}$ and pitch $50 \mu\text{m}$. As one can see, the impact energy from the non-bouncing-to-bouncing regime is independent of pillar height, while the critical impact energy for the bouncing-to-sticky regime increases linearly with the pillar height for small heights, before flattening out for pillar heights higher than ca. $20 \mu\text{m}$. This means that, contrary to what is predicted by the Wenzel and Cassie-Baxter equations, increasing the pillar height (and thereby the surface roughness) further above this threshold value will not stabilize droplets in the Cassie-Baxter state.

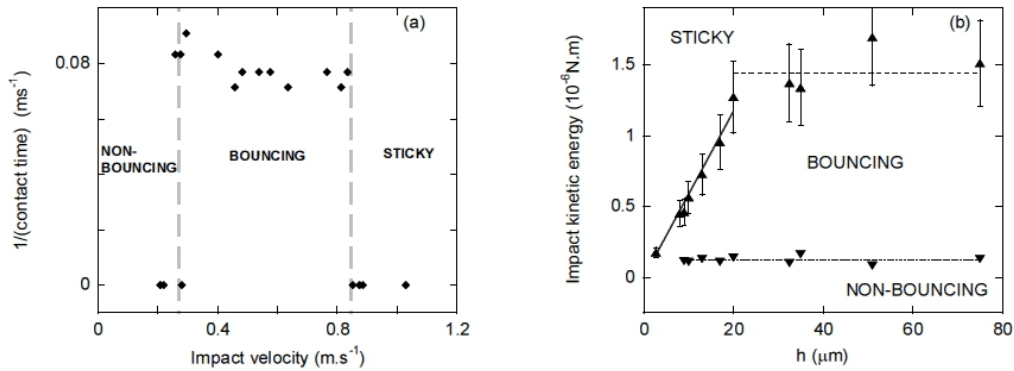


Figure 4.16: (a) Reciprocal contact time vs. impact velocity in the non-bouncing, bouncing and sticky regimes. (b) Non-bouncing to bouncing (∇) and bouncing to sticky (Δ) critical impact kinetic energies vs. pillar height h .^[47]

To wrap up the discussion regarding resistance to pressure: One obvious way to increase a pillared surface's resistance to pressure is to decrease the pillar separation. This method has a major drawback, however, as it increases the wet fraction of the projection area, thereby increasing the solid-liquid contact area and decreasing the contact angle. Therefore, a trade-off has to be made between increased resistance to regime transition by decreasing the separation distance, and increased CA by increasing the separation distance (see Figure 4.17).

A better solution is to increase the perimeter L while keeping A and A_c (and hence f_1 and the CA) unaltered. This will increase the critical pressure. For example, square pillars ($L/A = 2/r$) are expected to have ca. 12.8 % higher critical pressure than circular pillars ($L/A = 4/(\sqrt{\pi}r)$).

Yet another option (and probably the most effective one) is to scale down

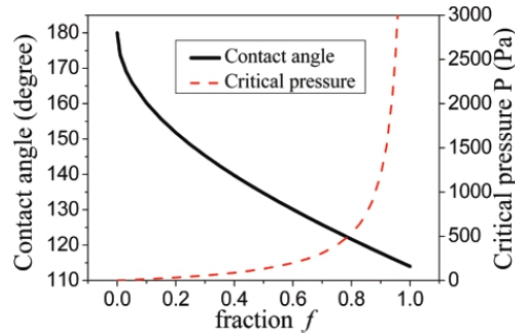


Figure 4.17: Contact angle and critical pressure as a function of the wet fraction of the projection area $f = a^2/(a + b)^2$ under the droplet. In this case, the 'intrinsic' CA is $\theta_0 = 114^\circ$, $a = 50 \mu\text{m}$ and $H = 10 \mu\text{m}$.^[32]

both the pillar cross section and the pillar cell. If these are scaled by a factor of $1/m$, then the critical pressure is increased by a factor of m , because the vertical surface area of pillars per projected surface area increases by the same factor.^[32]

4.9 Effect of Cell Structure

Surfaces with a closed-cell structure have proved to be able to sustain higher pressures than surfaces with open structures.^[6] The reason is that air in the closed cells under a droplet is confined in closed chambers, not having the possibility to escape to the sides. Thus, closed-cell structures are able to resist water droplets falling from greater heights. Other advantages with closed-cell structures are their mechanical robustness and the ease of fabrication using soft lithography and imprinting techniques directly on hydrophobic polymers.^[6] We will come back to closed-cell structures in Chapter 5.

4.10 Effect of Temperature and Water Condensation

Mockenhaupt et al.^[48] reported a gradual increase in wettability for a number of structured surfaces when the surface temperature was cooled from 20 to 5°C. The CA decreased and the sliding angle α increased, both on leaf surfaces from nature and on artificial surfaces. Control experiments with

non-evaporating glycerol droplets instead of water droplets verified that the observed deterioration is due to evaporation from the droplets and condensation onto the cooled surface due to the temperature difference. However, the deterioration was relatively small on hierarchically structured surfaces, e.g. on the tropical plant *Colocasia esculenta*, whose dual-scale surface comprising papillose cells covered with wax platelets is depicted in the SEM micrographs in Figure 4.18b. The micrographs in Figure 4.18a show the surface of the cabbage plant *Brassica oleracea*, and as we can see, this plant has a nanostructure in the form of long and fragile branched wax rodlets, but the microstructure is almost flat in comparison to that of *Colocasia esculenta*. The corresponding values of CA and sliding angle (SA) as a function

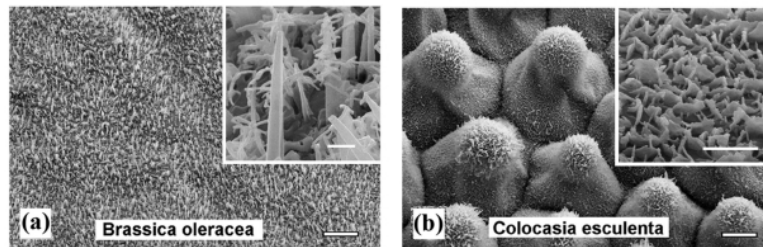


Figure 4.18: SEM micrographs depicting (a) the nanostructured surface of *Brassica oleracea*, and (b) the micro-nano hierarchically structured surface of *Colocasia esculenta*.^[48]

of temperature are shown in Figure 4.19. The deterioration was even less significant for the lotus plant than for *Colocasia esculenta*.

Wang et al. measured how the contact angle of water droplets on a superhydrophobic surface varied as a function of the working temperature in a climatic chamber.^[49] The surface was made from an Al substrate, processed by etching and subsequent coating with stearic acid. The CA is plotted against the working temperature in Figure 4.20. It can be seen that even if the hydrophobicity deteriorated somewhat with decreasing temperature, the CA remained relatively stable, never dipping below 150°.

Water condensation will be covered in greater detail in Chapter 8.

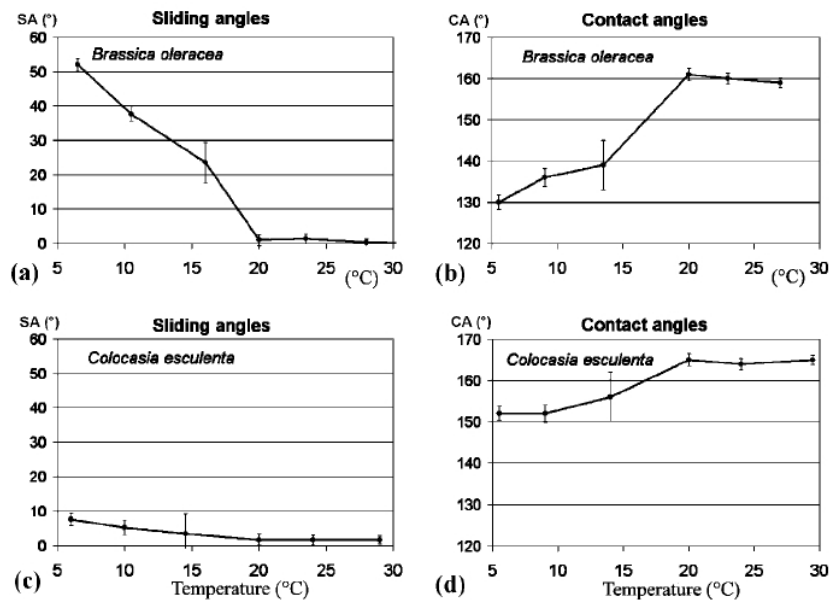


Figure 4.19: Sliding angle and contact angle as a function of temperature for *Brassica oleracea* and *Colocasia esculenta*. Moderate warming above 20°C had no significant effect. [48]

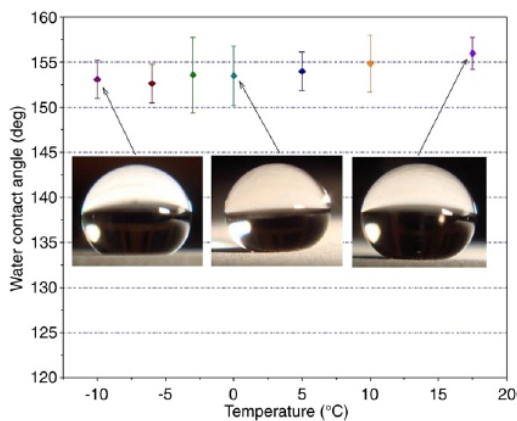


Figure 4.20: Water CA on a superhydrophobic Al surface as a function of climatic temperature. [49]

Chapter 5

Correlation Between Hydrophobicity and Icephobicity

Heterogeneous freezing of water droplets can take place by a variety of mechanisms, but it often involves heat transfer from the droplet through the water-solid interface and a subsequent heterogeneous nucleation process whereby the surface nano roughness or minute particles on the surface act as nucleation centers.^[50] The heat transfer through the solid-liquid interface of a droplet in the Cassie-Baxter state is illustrated in Figure 5.1.

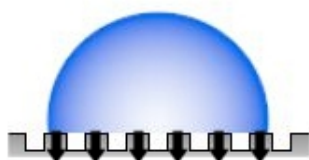


Figure 5.1: A water droplet in the Cassie-Baxter state. The arrows indicate the heat transfer through the water-solid interface.

Since air is a poor conductor of heat, it seems likely that the trapped air below a water droplet will create a thermal barrier which can delay and maybe even prevent accumulation and adhesion of ice. The term *icephobic* has been invented to describe such surfaces.^[51] The validity of this speculation is strengthened by the fact that the surface energy of ice is comparable to that of water (80.2 mJ/m for ice vs. 75.6 mJ/m for water^[52]).

In this chapter, the reported effect of superhydrophobicity on freezing delay, static and dynamic ice accumulation, and ice adhesion will be outlined.

Some major deterioration mechanisms are also covered in the last section.

5.1 Delayed Static Freezing

Tourkine et al.^[53] conducted an experiment to detect the possible static freezing delay induced by superhydrophobicity. An untreated and a superhydrophobic copper plate were used. The superhydrophobic surface was fabricated using a simple method based on galvanic deposition. The advancing and the receding CA was 165 and 155°, respectively (CAH = 10°), clearly indicating the Cassie-Baxter state.

The surfaces were brought in contact with a cryogenic liquid which kept the plates at a constant temperature of -8°C . They were then covered with an inverted Petri dish to avoid condensation of water from the air, which would otherwise replace the air cushion and lead to frost accretion. The research group deposited a volume of tap water (10-200 μL) of initial temperature $T = 25^{\circ}\text{C}$ on the copper plates, and measured the time that elapsed before the onset of freezing. Tap water was used because it contains impurities which will trigger freezing at 0°C . Due to its high purity, DI water can be supercooled, and hence the freezing delay may vary from experiment to experiment.

Figure 5.2 shows a comparison between two water droplets deposited on a microtextured superhydrophobic (left) and a flat (right) copper surface, respectively. A thin circular groove of radius $R = 10$ mm was etched on

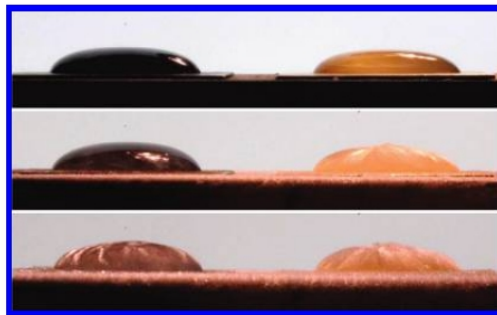


Figure 5.2: The freezing of water droplets on a superhydrophobic (left) and a flat (right) copper surface, both at temperature $T = -7^{\circ}$.^[53]

both surfaces to pin the contact line and make it possible to vary the droplet volume without changing the contact area. This allowed the researchers to

isolate the effect of surface structure on the icing delay. The images on the first row were captured just after deposition, and the colors of the droplets reflect the colors of the substrates. When the second photos were shot, the droplet on the flat surface had frozen, while that on the superhydrophobic surface was still liquid. When the last pictures were taken, the left droplet had also frozen. The group made a series of experiments on both surfaces and plotted the freezing time as a function of the droplet height, as shown in Figure 5.3. In this case, the droplet height is a direct function of the droplet volume.

The plot clearly shows that the freezing time is significantly delayed on the superhydrophobic surface. The slope of the line fitting the values measured on the superhydrophobic surface is approximately twice as steep as the line fitting the values measured on the flat surface. The reasonable conclusion is that the reduced water-solid contact area causes the freezing delay.

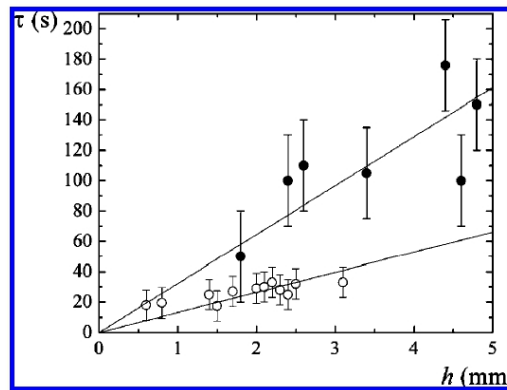


Figure 5.3: Freezing time τ as a function of droplet height h for droplets of the same surface area, deposited on flat copper (white dots), on copper treated with a fluorinated thiol (white squares) and on superhydrophobic copper (black dots).^[53]

5.2 Reduced Dynamic Freezing

Much attention has been given to the freezing of *static* water droplets on supercooled surfaces. In reality, however, atmospheric icing is a *dynamic* process. Wang et al.^[49] compared the ice accretion on Al samples with different hydrophobicity by spraying them with supercooled water droplets in a wind tunnel with a working temperature of -6°C and a generated wind speed of ca. 3 ms^{-1} . The diameter of the droplets hitting the samples was

held at ca. 0.5 mm to simulate drizzle and freezing rain, and the icing process was periodically recorded with a digital camera. The system is shown schematically in Figure 6.6 (Chapter 6).

One of the surfaces was a hydrophilic cleaned and dried Al sample, one was a hydrophobic Al surface coated with a room temperature vulcanized silicone rubber (RTV SR), and one was a superhydrophobic etched and coated Al surface. Images of the ice accretion are shown in Figure 5.4. The im-

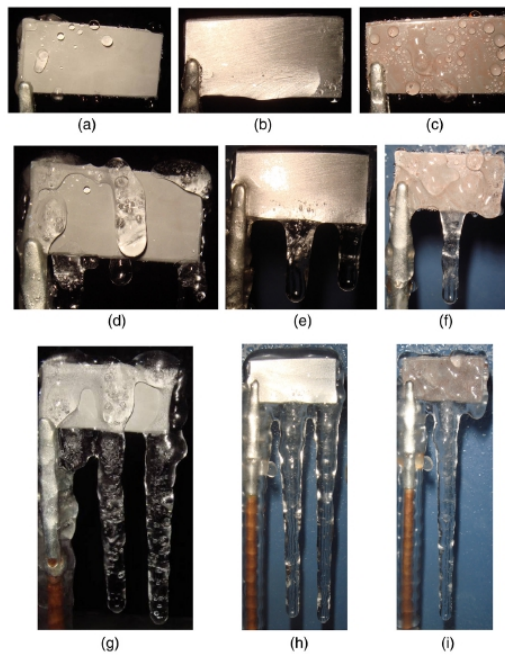


Figure 5.4: Ice accretion on three different aluminium surfaces: A superhydrophobic (a, d and g), a hydrophilic (b, e and h), and a hydrophobic (c, f and i) one. The photos in the first row are taken 1 minute after the onset of water spraying, those in the second row were taken after 10 minutes, and those in the third row were taken after 30 minutes.^[49]

ages show that the hydrophilic surface was quickly covered with a layer of water which transformed into ice. Water had more difficulty in covering the hydrophobic surface, but after 10 minutes this surface too was covered almost completely. On the superhydrophobic surface, on the other hand, water droplets only accreted on a few spots, and all new ice accumulated on these places. Even after 30 minutes, most of the surface was still ice-free. The same development was observed when the test was repeated with Al rods instead of Al sheets.

The SEM micrographs in Figure 5.5a and 5.5b show that the superhydrophobic Al surfaces consist of microscale protrusions and voids with randomly oriented nanoscale slices superimposed on them. This hierarchical structure is believed to give rise to the superhydrophobicity. In addition, the long hydrophobic carbon chains of the stearic acid coating decreases the interaction force between the Al substrate and the water droplets. The SEM micrograph in Figure 5.5c shows that the weak points on which ice accumulated can be attributed to flat areas on the superhydrophobic surface.

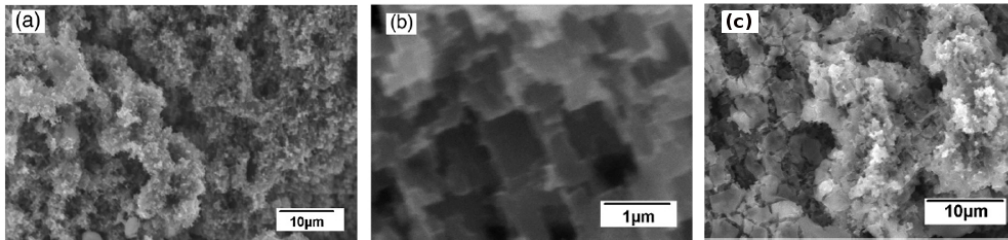


Figure 5.5: (a) and (b) SEM micrographs of the superhydrophobic Al surface at two different magnifications. (c) SEM micrograph showing a weak point on the superhydrophobic Al surface.^[49]

Mishchenko et al.^[6] tested ice accumulation on supercooled nano- and microstructured coatings that were exposed to supercooled water droplets impinging from a height of 10 cm onto the substrates. The substrate temperature was varied between -35 and 20°C and the droplet temperature was varied between -5 and 60°C . Three different tilt angles were used (0 , 30 and 60°). To avoid water condensation in the surface structures, the experiments were carried out under low humidity conditions. Figure 5.6 shows pictures from the test of smooth Al (a), smooth fluorinated Si (b), and microstructured fluorinated Si (c) surfaces. In these three cases the substrate temperature was -10°C and the substrate was tilted at 30° .

The inset shows micrographs of the high-aspect-ratio surface structures on the samples that were tested; posts, bricks, blades and honeycombs. The research group found that the freezing delay on the flat hydrophobic surface relative to the hydrophilic one was approximately 1 min, but after 10 min both substrates had experienced significant ice accumulation. The superhydrophobic surface, on the other hand, remained practically ice-free during the 10 min that the experiment lasted. The ice-repellent property was present with many different geometries, tilt angles, and substrate and droplet temperatures, but the best results were obtained with the closed-cell structures, and in particular the honeycomb structure.

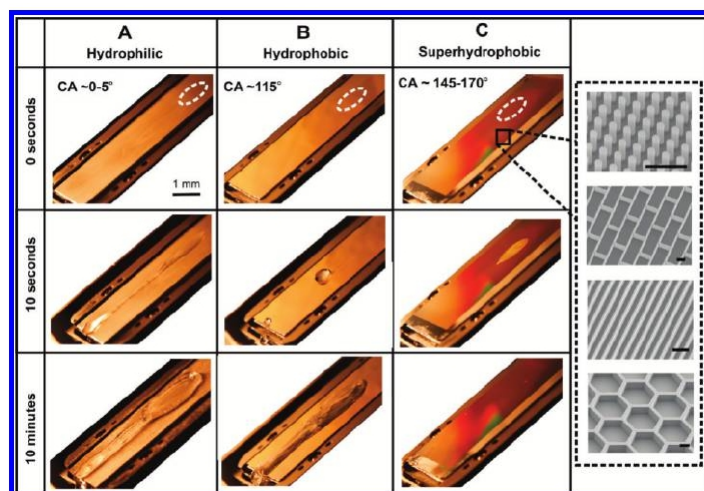


Figure 5.6: Ice accumulation on a hydrophilic flat Al surface (a), a hydrophobic smooth fluorinated Si surface (b), and a superhydrophobic microstructured fluorinated Si surface (c). The given CA values are the advancing CAs of the water droplets measured on each surface. The micrographs in the insets show different surface structures on the superhydrophobic surfaces. Scale bars: $10\mu\text{m}$.^[6]

To achieve a better understanding of the mechanisms behind the dynamic icing process, the behavior of a single droplet was recorded with a high-speed videocamera during its impingement on both a tilted and a flat surface (both with $T < 0^\circ\text{C}$). The images in Figure 5.7 show that on the low-friction superhydrophobic surface, the surface tension is able to retract the droplet completely after spreading. The droplet bounced off the surface ca. 20 ms after impingement, before the onset of freezing. This was not the case on the high-friction hydrophilic surface, where the droplet hardly retracted at all after spreading, and froze with a large contact area to the surface. On the hydrophobic surface, some retraction was observed, but not enough to bounce off the substrate before freezing. The retraction speed decreased with decreasing substrate temperatures due to increased viscous shear, but the superhydrophobic surfaces remained ice-free down to -25°C .

Once again closed-cell structures proved to have the best icephobic properties. Due to confinement of air in the closed cells, they were able to retain their superhydrophobic properties at higher pressures without the droplets undergoing transition to the Wenzel state. Experiments carried out in a high-pressure test chamber indicated that surfaces with a closed-cell structure were able to retain superhydrophobicity even when the droplets hit at

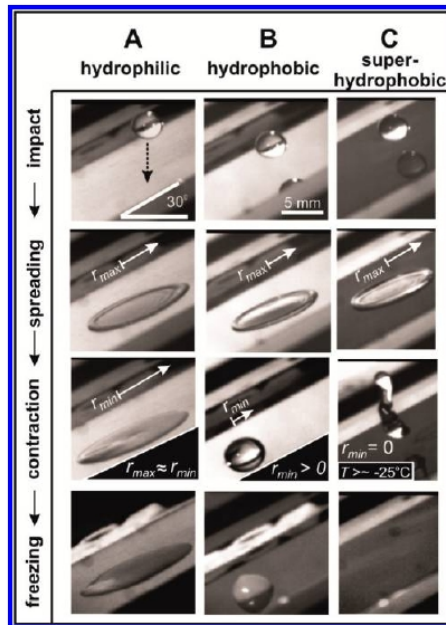


Figure 5.7: Dynamic behavior of water droplets impinging on tilted surfaces at sub-zero temperature.^[6]

a velocity of $90\text{-}135\text{ ms}^{-1}$. For temperatures above -25°C , the ice froze in the Cassie-Baxter state, and the adhesion was therefore low enough that it could be easily removed by raising the temperature above 0°C .

Tourkine et al.^[53] studied the dynamic behavior of water droplets on both superhydrophobic and flat Cu surfaces. Water droplets of volume $\sim 100\ \mu\text{L}$ were deposited on the surfaces, which were tilted at 40° , and the position of the leading and the trailing edge was recorded as a function of time as the droplets moved down the plane. The position vs. time relationship is shown graphically in Figure 5.8. On the superhydrophobic surface, the droplet remained compact all the way down, and it slid off the plane before freezing occurred, leaving behind a clean and dry surface. On the flat Cu surface, on the other hand, the initial diameter was much larger due to the smaller CA, and the trailing edge hardly moved at all before it froze. The leading edge did not make it to the bottom before it froze either, and the substrate was left covered with a long patch of ice. From this experiment, it is reasonable to conclude that superhydrophobic surfaces can prevent icing from dynamic rain droplets on cold solids.

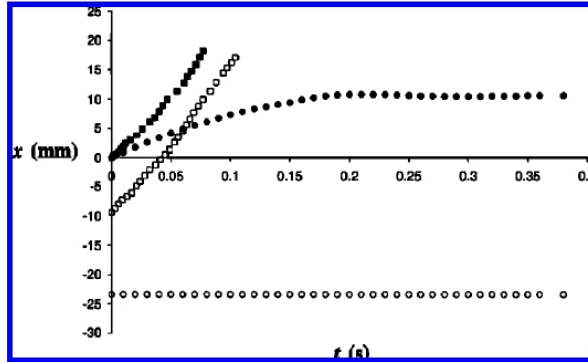


Figure 5.8: Position (x) of the leading (black) and trailing (white) edges of water droplets deposited on cold Cu substrates (-8°C) tilted 40° . The squares and the circles represent values measured on a superhydrophobic and a flat surface, respectively.^[53]

5.3 Effect of Nanoscale Roughness on Freezing Delay

Jung et al.^[51] studied delayed freezing of inkjet-generated supercooled water microdroplets accumulating on various surfaces ranging from hydrophilic to superhydrophobic. The droplets were generated at a rate of 80 Hz and continuously impinged onto the same sample location, forming a growing sessile droplet before eventually freezing. The onset of freezing was marked by a sudden clouding of the water volume due to spontaneous crystallization. Both the surfaces and the falling droplets were kept at -20°C .

Expectedly, their results show an increasing icing delay with increasing values of CA for the rough surfaces, as represented graphically in Figure 5.9a. However, the hydrophilic surfaces with roughness values close to the *critical nucleus radius* displayed significantly better icephobicity than typical hierarchically rough superhydrophobic surfaces of the same material, with icing delay times at least one order of magnitude longer. The critical nucleus radius is the minimum size an incipient ice crystal needs to reach in order to maintain a stable freezing process. With water temperature -20°C , the radius of the critical nucleus was calculated from $r_c = 2\gamma_{IW}/\Delta G_{f,v}$, where γ_{IW} is the ice-water interfacial tension, and $\Delta G_{f,v}$ is the volumetric free energy difference between bulk ice and bulk liquid. At -20° , the value of r_c is 2.2 nm. On smooth surfaces, the icing delay increased as the surface roughness approached r_c in the nanometer regime. Surfaces with surface

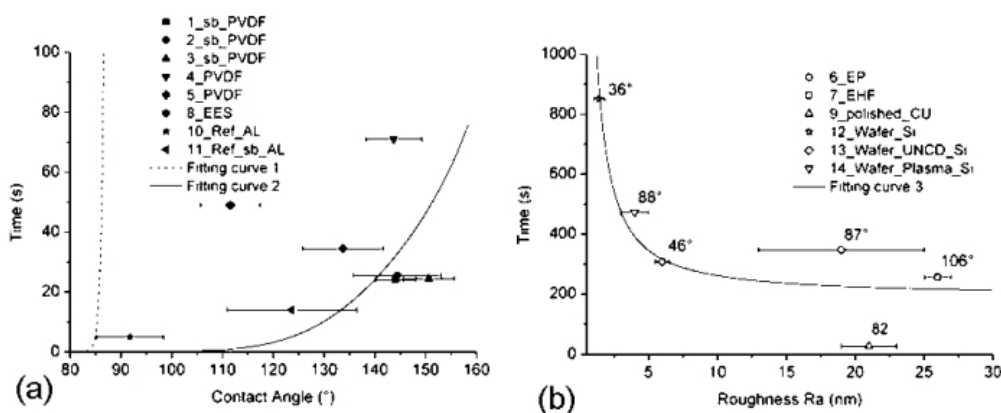


Figure 5.9: (a) Freezing delay time as a function of advancing CA for highly rough surfaces. (b) Freezing delay time as a function of surface roughness for smooth surfaces. The values tagged to the data points represent the measured CA on the respective surfaces. [51]

roughness close to r_c resisted icing considerably longer than typical rough superhydrophobic surfaces, as can be seen in Figure 5.9b.

These results clearly show that the icephobicity of a surface is not directly correlated with its hydrophobicity. The detailed surface morphology has an important effect on the kinetics of the freezing process. That the nanoscale smooth surfaces were best at delaying the freezing process indicates that decreasing the solid-liquid contact area may not necessarily offer the best choice in icephobic applications, and that nanoscale surface roughness may have a larger influence on freezing delay times.

Similar results have been reported by Cao et al., [50] who studied the formation of ice from supercooled water droplets on superhydrophobic surfaces made from a mixture of organosilane-modified nanoparticles of various diameters (ranging from 20 nm to 20 μm) and a polymer binder, as shown in Figure 5.10a. Figure 5.11a shows the measured advancing and receding water CAs on the different surfaces. As can be seen, most of the coatings had CAs higher than 150° and low CAH, which characterizes superhydrophobic surfaces.

After being stored for 3 h in a -20° freezer prior to the experiment, the surfaces were tilted at 10° to the horizontal plane. 500 mL of supercooled water ($T = -20^\circ$) was then poured onto each surface at a constant rate for about 10 s from a height of ca. 5 cm. Figure 5.12 shows images of a coated (left) and an untreated (right) Al surface during the experiment. Ice formed instantly upon impact with the untreated plate, but no ice accretion was

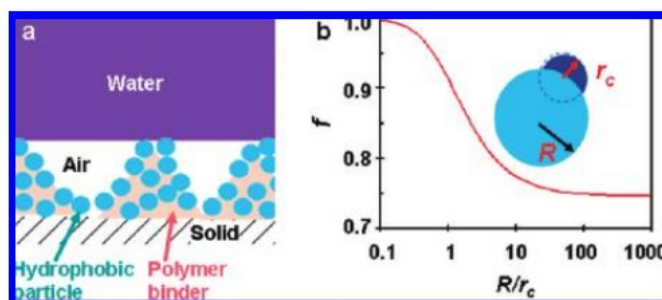


Figure 5.10: (a) Schematic illustration of a water droplet in contact with a superhydrophobic polymer/nanoparticle (or polymer/microparticle) surface. (b) Ratio (f) of the free energy barrier of nucleation around a spherical particle relative to that in the bulk vs. the particle radius R relative to the critical nucleation radius r_c .^[50]

observed on the coated plate until ice started to build up from the bottom upon contact with an uncoated Al tray.

The experiment was repeated 20 times on each surface, and the icing probability was calculated by dividing the number of cases when icing occurred by the total number of experiments. The icing probability as a function of particle diameter is shown in Figure 5.11b.

Comparing Figure 5.11a and 5.11b, one can conclude that the critical particle size that determines the superhydrophobicity of the surfaces is in another length scale than that which determines the icephobicity. Cao et al. accounts for the observed difference in length scale using a classical heterogeneous nucleation theory which predicts that the free energy barrier of heterogeneous nucleation around a spherical particle decreases as the particle size increases above the critical nucleation radius. Under the experimental conditions in this case, r_c was calculated to be 21.6 nm.

5.4 Reduced Ice Adhesion

When water droplets freeze in the Cassie-Baxter state, it is intuitively obvious that the ice adhesion will be reduced as compared to that on a smooth surface because of the reduced contact area. Some research groups have tried to find a correlation between the strength of ice adhesion and hydrophobicity by plotting measured ice adhesion values against the static CA. This has led to mismatching results, however.

Kulinich and Farzaneh^[54] reported an almost linear correlation between

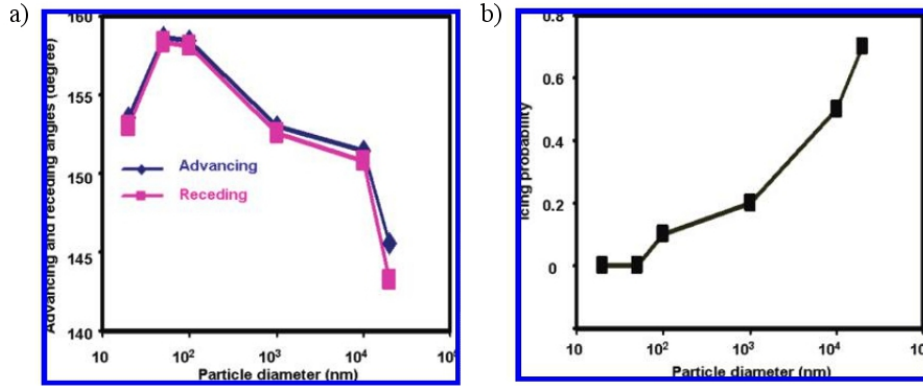


Figure 5.11: a) Advancing and receding water contact angles of six different polymer-nanoparticle coatings as a function of the particle size. b) Icing probability as a function of particle size. ^[50]

average ice adhesion strength and water CAH for ten rough polymer-based hydrophobic surfaces with different CA and CAH, but this hypothesis should later be modified by Meuler et al., ^[55] who tested the ice adhesion on nominally smooth ($r_f < 1.01$) bare and coated steel discs. 21 samples were coated with 200-300 nm thick layers made from polymers (e.g., PEMA, PMMA and PDMS) and fluoroPOSS). The latter is known to be one of the lowest surface energy molecules available ($\gamma_{SA} \approx 10$ mN/m ^[44]). The substrates were made with a broad range of substrate-water interactions, and the research group looked for a relationship between the ice adhesion strength and three different measures of water wettability: $[\cos \theta_R - \cos \theta_A]$, which scales with the liquid drop roll-off angle; $[1 + 0.5(\cos \theta_A + \cos \theta_R)]$, which scales with the equilibrium work of adhesion; and $[1 + \cos \theta_R]$, which scales with the practical work of adhesion.

When plotting the ice adhesion strength against CAH, their data set contained several points that deviated substantially from the linear trend found by Kulinich and Farzaneh, thus providing strong evidence that the ice adhesion strength is not a direct function of CAH. Furthermore, extrapolating both the data of Kulinich/Farzaneh and the data of Meuler et al. does not lead to lines passing through the origin. In other words, the ice adhesion does not approach zero as $[\cos \theta_R - \cos \theta_A] \rightarrow 0$, which one would expect if the correlation were correct. Instead, they found that the ice adhesion strength correlates strongly with the last quantity $[1 + \cos \theta_R]$, the linear correlation factor being $R^2 = 0.92$. With the best coating (PEMA and fluoroPOSS in a 4:1 ratio) they were able to reduce the ice adhesion strength

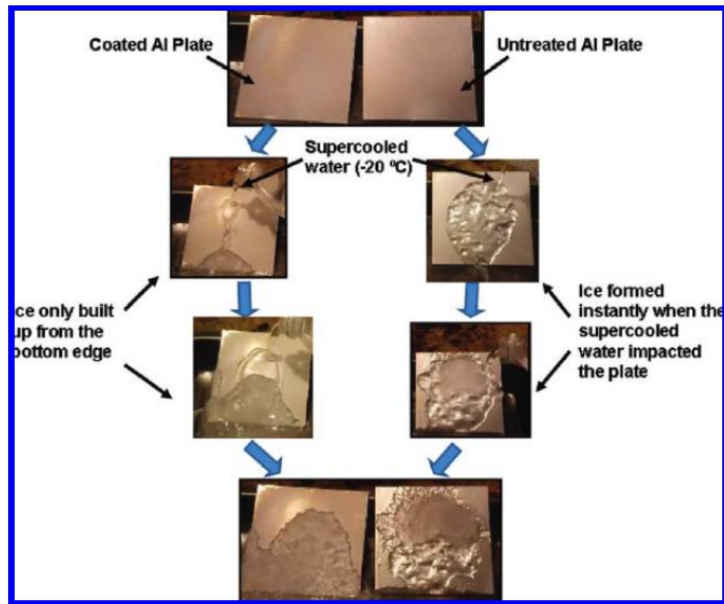


Figure 5.12: Optical images showing the icing process when supercooled water is being poured onto an Al plate coated with a nanoparticle-polymer composite with 50 nm particle size (left) and an untreated Al plate (right).^[50]

by a factor of 4.2 relative to the bare steel disc. The data are summarized in the graph in Figure 5.13. Data from two other research groups are also included. The measurements by Meuler et al., Kulinich et al. and Dotan et al. were obtained at -10°C , -10°C and -8°C , respectively. The results of these experiments suggest that ice adhesion can be minimized by maximizing the receding CA.

5.5 Deterioration of Icephobicity

Kulinich et al. investigated the anti-ice performance of various superhydrophobic surfaces under different conditions.^[56] The coatings were prepared on polished aluminium substrates. One group of samples was coated with a coating based on a ZrO_2 -incorporated fluoropolymer, another group was coated with FAS-17, a third group was coated with stearic acid. Surfaces with different wetting properties were obtained by spin-coating the suspension at different rotational speeds.

Their experiment shows that the icephobic properties deteriorate with

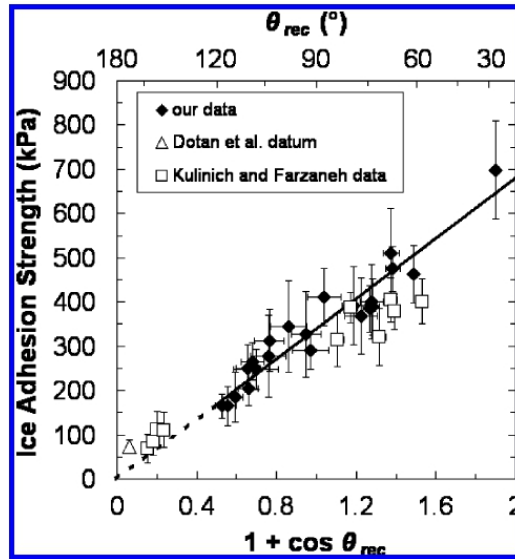


Figure 5.13: Compilation of ice adhesion strengths measured by three research groups, plotted against the practical work of adhesion to remove a liquid water drop from a surface. ^[55]

increasing icing/deicing cycles, a phenomenon attributed to damage on the surface structures (Figure 5.14). The top of the surface asperities have a tendency to indent into the water droplet, and when the droplet freezes and expands, mechanical tension is created that leads to damage and breakage. When the next icing event starts, the water droplet will therefore sit deeper on the surface, and the solid-ice interface area will increase, thereby increasing the ice adhesion. Figure 5.15 shows how the shear stress of ice detachment increases with the number of icing/deicing cycles.

The research group also showed that the anti-icing properties significantly deteriorate in humid conditions, due to water condensation both on top and between the surface asperities. Figure 5.16a shows how the CA values decreased and the CAH values increased with the condensation time. Figure 5.16b shows that the shear stress of ice adhesion increased with the condensation time, while the time needed to ice the samples was reduced.

Although ice formation from supercooled water droplets is an important icing mechanism, frost formation—i.e., direct sublimation of gaseous water to ice crystals—should also be considered. Varanasi et al. ^[57] studied frost formation on superhydrophobic surfaces comprised of arrays of hydrophobic Si posts manufactured by photolithography and coated with a thin layer of (tridecafluoro-1,1,2,2-tetrahydrooctyl)trichlorosilane (Gelest) which pro-

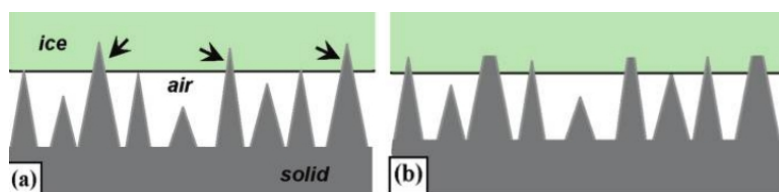


Figure 5.14: (a) Ice on a rough surface. The arrows indicate the asperities that are indented into the ice, and are likely to be damaged during icing or de-icing. (b) The same surface during the next icing cycle, with increased ice-solid contact area because of the broken asperities. [56]

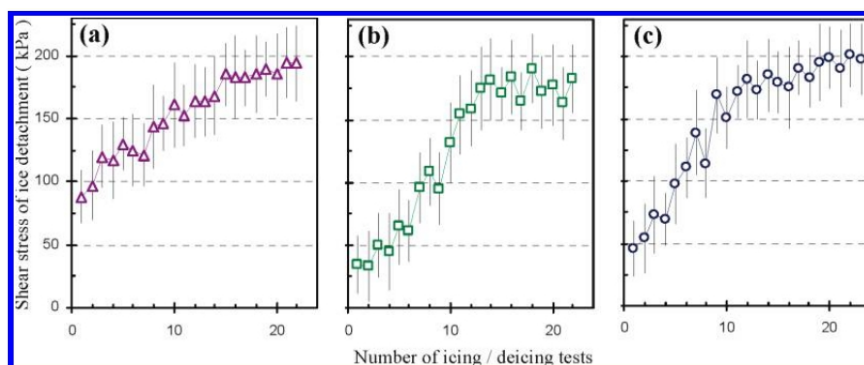


Figure 5.15: Ice adhesion strength as a function of icing-deicing cycles on three superhydrophobic surfaces: Spin coated ZrO_2 incorporated fluoropolymer (a), FAS-17 coated etched aluminium (b), and etched Al coated with stearic acid (c). [56]

vided superhydrophobicity. Frost nucleation was triggered by lowering the substrate temperature below the freezing point and increasing the vapor pressure in the chamber. ESEM (environmental SEM) micrographs revealed that frost nucleation occurred indiscriminately on the surfaces instead of at preferred places (Figure 5.17). This is due to the homogeneous surface energy. Frost-covered surface textures are hydrophilic, something that was confirmed by ice adhesion tests. Figure 5.18 shows a droplet-impact test on a dry (b) and frosted (c) superhydrophobic surface. On the dry surface, the antiwetting capillary pressure is greater than the dynamic wetting pressure, and the 1 mm radius droplet recoils from the surface. On the frosted surface, on the other hand, the frost forces the impacting droplet into the Wenzel state, and subsequent freezing results in *Wenzel ice*.

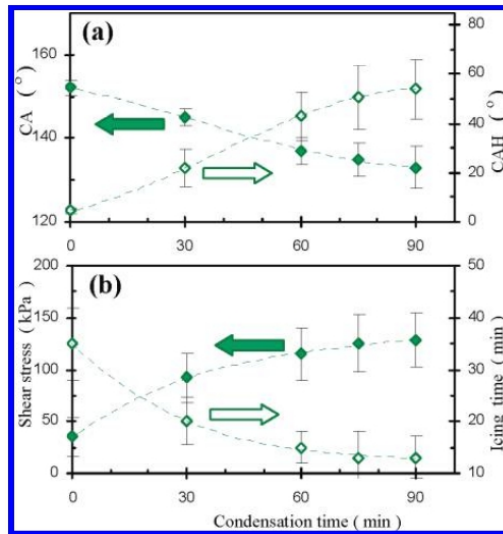


Figure 5.16: (a) CA and CAH values on a cold FAS-17 coated superhydrophobic surface as a function of water condensation time. (b) Shear stress of ice detachment (filled diamonds) and icing time (open diamonds) on the same surface as a function of water condensation time.^[56]

Ice adhesion tests were also carried out at -15° . The frosted superhydrophobic surfaces were actually shown to have a higher ice adhesion strength than their flat counterparts. The normalized ice adhesion strength is plotted against the normalized surface area in the graph in Figure 5.19. The linear fit passes through the origin, indicating that all the surface area is available for contact with the ice, resulting in Wenzel ice.

Surfaces with both micro- and nanostructure have been reported to perform somewhat better in humid environments than other surfaces.^[48] None the less, the results presented in this section raise doubt over the use of many superhydrophobic materials as anti-icing surfaces because they may be limited both with respect to duration and climatic conditions. One will have to look for very rigid or very elastic materials. In humid conditions, water condensation or frost formation (depending on the ambient conditions) between the surface asperities are major concerns that will lead to a significant deterioration of the anti-icing performance.

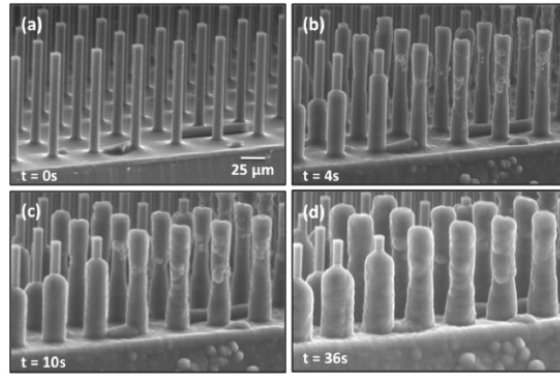


Figure 5.17: ESEM micrographs showing frost formation on a pillared superhydrophobic surface.^[57]

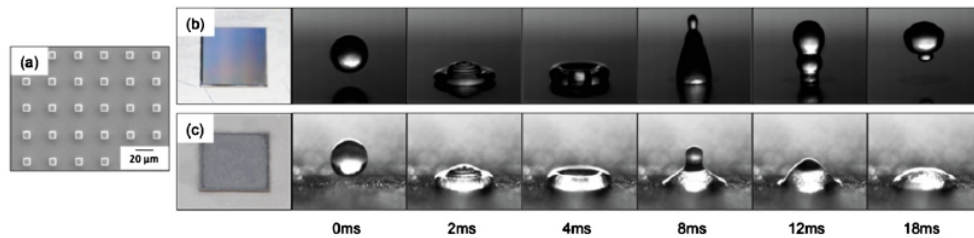


Figure 5.18: (a) Top view SEM micrograph of the pillared surface structure with pillar width, pitch and aspect ratio $10\ \mu\text{m}$, $20\ \mu\text{m}$ and 1, respectively. (b) Photograph of the dry surface (left) and sequential images of the droplet impact (right). (c) Photograph of the frosted surface (left) and sequential images of the droplet impact (right).^[57]

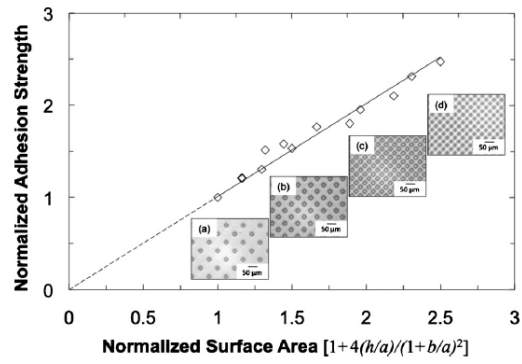


Figure 5.19: Measured ice adhesion strength of the textured PDMS surfaces normalized relative to the measured ice adhesion strength of the smooth surface as a function of total surface area normalized relative to the projected area. ^[57]

Chapter 6

Characterization and Testing of Superhydrophobic and Icephobic Properties

6.1 Chemical Composition and Morphological Characterization

Morphological characterization can be conducted using instruments like profilometers and scanning electron microscopes with energy-dispersive X-ray spectroscopy (SEM/EDX). The former is a good instrument for measuring roughness and analyzing morphology, while the latter can also be used to give information about the chemical composition of the surface. If the surface is very smooth, an atomic force microscopy (AFM) should be used instead of the profilometer.

The most common parameter used to characterize surfaces with random roughness is the *root mean square* (RMS), defined as the standard deviation from the center-line average of the surface profile (see Figure 6.1). In the two-dimensional case, the root mean square is given by^[61]

$$\sigma^2 = \frac{1}{L} \int_0^L (z - m)^2 dx \quad , \quad (6.1)$$

where m is the center-line average, z is the vertical position, and L is the sampling length.

To separate between spiky surfaces (which are associated with low values of CAH) and surfaces predominated by valleys (which are associated with high CAH values), two additional surface parameters are required: *surface*

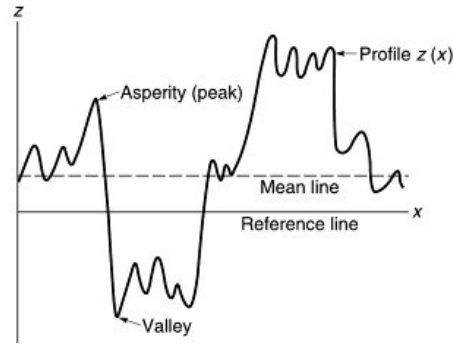


Figure 6.1: Schematic illustration of a rough surface profile.^[61]

skewness (S_{SK}) and *surface kurtosis* (S_{KU}). They are defined mathematically as^[61]

$$S_{SK} = \frac{1}{\sigma^3 L} \int_0^L (z - m)^3 dx , \quad (6.2)$$

and

$$S_{KU} = \frac{1}{\sigma^4 L} \int_0^L (z - m)^4 dx . \quad (6.3)$$

The surface skewness is a measure of the assymetry of the surface profile about the mean plane, so that spiky surfaces with peaks have positive values of S_{SK} and surfaces predominated by valleys have negative values of S_{SK} . The surface kurtosis is a measure of how narrow the peaks and valleys are, so that spiky surfaces have higher S_{KU} values. The differences are illustrated in Figure 6.2.

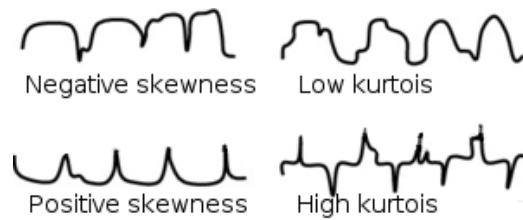


Figure 6.2: Schematic illustration of surfaces with different skewness and kurtosis.^[61]

To minimize the water-solid (or ice-solid) surface area, superhydrophobic and icephobic surfaces should have high values of both S_{SK} and S_{KU} .

6.2 Measuring Wettability

A modern drop shape analysis instrument can be used to measure the wetting behavior on prepared superhydrophobic surfaces. With the so-called sessile drop method, a water droplet (smaller than the capillary length) is gently placed on the surface using a needle coupled to a computer-controlled liquid-dispenser system, and goniometer optics and a computer with a special software are used to measure the static CA after the needle is removed. A drop shape analysis system from Krüss is shown in Figure 6.3.



Figure 6.3: A DSA30 drop shape analysis system from Krüss.^[62]

Due to the presence of long-lived metastable configurations, individual measurements may deviate substantially from the average value,^[55] so several measurements on different parts of the sample should be made to minimize the uncertainty. One should also wait a few seconds for the droplet to stabilize after it is placed on the surface. Some groups have also suggested that slightly vibrating the surface may help the droplet reach the equilibrium.^[55]

To measure the CA at sub-zero temperature, one can use a so-called *Peltier device* (see Figure 6.4).^[56] A Peltier device is a thermoelectric device which moves heat from one of its sides to the other when electricity is applied. The cold side is then brought in contact with the substrate and cools it to a chosen temperature before the water droplet is placed on it.

To measure the CAH, there are several options. One is the extension-contraction method (see Figure 6.5). Here, a syringe is used to add and subtract water to and from the droplet. When water is withdrawn from the droplet, the droplet will recede with a constant contact angle, which is the receding contact angle, θ_R . When water is added to the droplet, then the droplet grows while the contact angle is maintained at the advancing contact angle, θ_A .

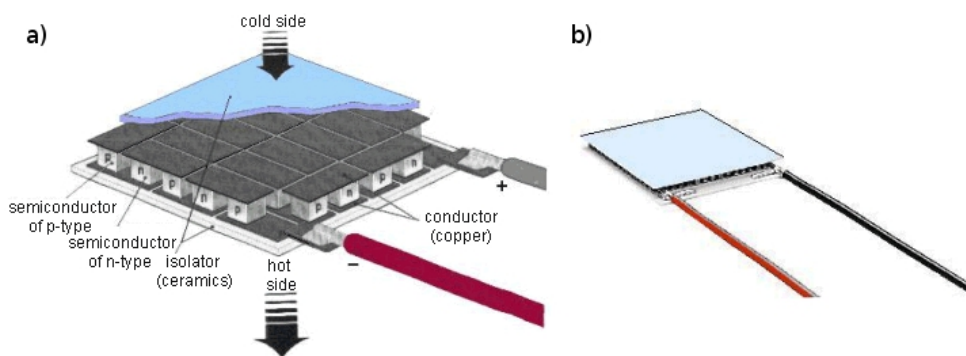


Figure 6.4: a) The structure of a peltier device. b) A peltier device.^[63]

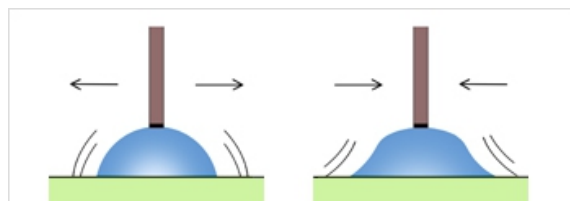


Figure 6.5: CAH measurement with the extension/contraction method.^[64]

Alternatively, the CAH can be evaluated by holding the water droplet in contact with a stationary needle while moving the substrate in one direction. The advancing and receding contact angles can then be measured on the water droplet's forefront and backside, respectively.

A third possibility is to gradually incline the plane on which the water droplet rests, using a motorized tilting stage. The advancing and receding contact angles can then be measured on the droplet's downside and upside, respectively, just before it starts moving down the plane. With this method—which is called the sliding method—other data than the CAH are also obtainable, such as the critical tilt angle and the adhesive work between the liquid and the solid.^[64]

6.3 Measuring Ice Adhesion

Measuring ice adhesion is not as straightforward as measuring water contact angles, as there are no standardized and commercially available instruments

available that are designed for measuring solid-solid adhesion strengths.^[55] Different groups have therefore come up with their own solutions.

One possibility is to mimic atmospheric glaze ice accretion by spraying supercooled water droplets through nozzles into the air stream in a wind tunnel / icing chamber, and then use a centrifugal machine to measure the adhesion of the accreted ice by spinning the sample with increasing rotational speed until the ice detaches.^[65] Parameters such as air temperature, water temperature, water content and air speed should be adjusted so that to simulate icing in natural environment. The distance between the nozzles and the substrate should be long enough for the water droplets to reach thermodynamic equilibrium before they impinge on the substrate. A schematic of a wind tunnel is shown in Figure 6.6.

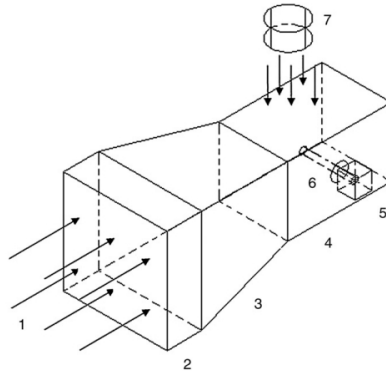


Figure 6.6: Icing experimental system: (1) fan, (2) stable section of the wind tunnel, (3) contraction section of the wind tunnel, (4) test section of the wind tunnel, (5) conductor motor, (6) experimental conductor, and (7) spray nozzle.^[49]

Using this method to measure the ice adhesion strength, one will first have to evaluate the ice mass and the ice-surface contact area while keeping the sample in a climatic chamber at sub-zero temperature.^[66] The iced sample is placed on one side of an Al beam and a counter-weight is placed on the other side to balance the weight of the ice (see Figure 6.7). The ice adhesion strength can be evaluated by assuming that the adhesive force is equal to the centrifugal force $F = mr\omega^2$, where m is the ice mass, r is the beam radius and ω is the rotational speed in rad s^{-1} at the moment of detachment. The moment of detachment can be detected with sensors embedded in the walls of the centrifuge. Lastly, the shear stress can be calculated by dividing the calculated force by the contact area: $\tau = F/A$.

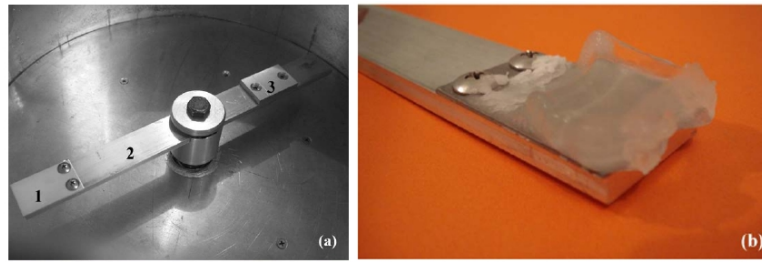


Figure 6.7: (a) Centrifuge equipment for measuring ice adhesion, comprising a coated sample (1), an Al beam (2), and a counter-weight (3). (b) A coated sample with artificial glaze ice.^[66]

As icing chambers and complex centrifuge equipment are unavailable in most laboratories, other groups have come up with less cumbersome solutions. For example, Meuler et al.^[55] simply poured water into cuvettes of square cross-section, loaded them onto their samples (coated steel discs), inverted the assembly, froze the water overnight, and then measured the average stress necessary to remove the ice columns (encased in cuvettes) from the surface using a propelling force transducer at constant velocity (see Figure 6.8). The adhesion strength was then calculated by dividing the measured force by the cross-sectional area of the ice-substrate interface.

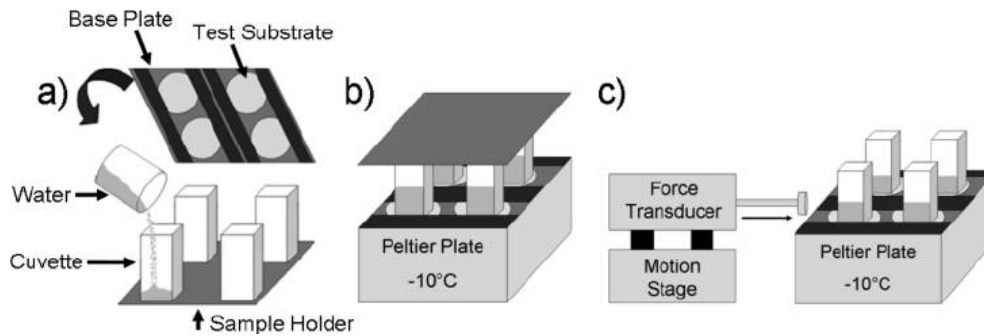


Figure 6.8: Schematic description of one possible procedure to measure ice adhesion. A liquid-cooled Peltier cooling plate is used to cool down the sample surface. Frost formation can be avoided by conducting the experiment in a low-humidity N_2 atmosphere.^[55]

Chapter 7

Fabrication of Superhydrophobic Surfaces

The number and scope of techniques to produce superhydrophobic surfaces have skyrocketed as nanotechnology has made possible both top-down and bottom-up fabrication of nanostructured surfaces, and the number of suggested applications has expanded in response. As of 2008, over 200 superhydrophobicity-related patents have already been granted, and various superhydrophobic products—such as surface coatings, exterior paints, and roof tiles—are already on the market.^[20]

Inspired by superhydrophobic surfaces in nature, such as the lotus leaf, researchers have devoted much effort to developing superhydrophobic surfaces that are structured both at the microscale and at the nanoscale. Taking advantage of the Wenzel and Cassie-Baxter equations and more sophisticated models, researchers have developed a plethora of fabrication routes to create dual-scale superhydrophobic surfaces on a wide range of substrates, e.g., polymers, metals, wood, glass and textiles. Both bottom-up and top-down methods are used, including plasma and/or chemical etching, photolithography, nanoimprint lithography, phase separation and self-assembly of nanoparticles.

The chosen method in each individual case depends on the material to be treated, and other desired properties, such as mechanical strength, transparency, electrical properties, etc. Top-down methods generally give very good control over the detailed surface structure, but they are often rather expensive, and hence they are mostly used in research applications thus far. Bottom-up methods are cheaper and may have a larger potential in industrial applications, despite poorer control of the detailed surface structure.

A comprehensive review of the fabrication methods is beyond the scope

of this thesis, but a few fabrication routes will be discussed briefly in this chapter.

7.1 Lithography Techniques

Photolithography is useful for generating well-defined patterns in a surface, e.g. pillars. The idea is to expose a photoresist (a photoactive polymer) to radiation through a photomask, and then remove the exposed or the unexposed parts, depending on the nature of the polymer used. The patterned polymer can then either be used directly, or be used as a mask for deposition or etching. Different radiation sources can be used, such as UV, X-rays, electrons, and ions. Often it is necessary to apply a hydrophobic coating to generate superhydrophobicity.

A promising candidate for the fabrication of superhydrophobic surfaces is *nanoimprint lithography* (NIL). NIL has several major advantages such as high throughput, high resolution, and low cost relative to other lithography techniques (photolithography, electron beam lithography, scanning probe lithography, etc.). Among the most interesting approaches is to directly use the dual-scale roughness of surfaces in nature—such as plant leaves, insects, lichen, mould and fungus—as stamps. For this purpose, Zhang et al.^[58] used the wings of the insect *cicada*, shown in Figure 7.1. In addition to being abun-

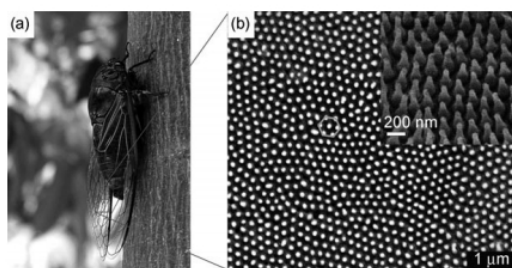


Figure 7.1: (a) Photograph of a cicada. (b) SEM micrograph depicting the surface of a cicada wing.^[58]

dant in nature, these insects have wings with a low surface tension—which renders the use of an anti-adhesive layer unnecessary—and the material can have a Young’s modulus as high as 7-9 GPa. This is sufficient for imprinting polymers like PMMA.^[58]

The first step is to form a nanowell array in the polymer by pressing the pillared cicada wing surface into a PMMA support at an elevated temperature, as seen on top in Figure 7.2. Subsequently, the pattern can either

be transferred to an underlying silicon substrate using reactive ion etching (RIE), or it can be used as a mold to fabricate a patterned structure of another material.

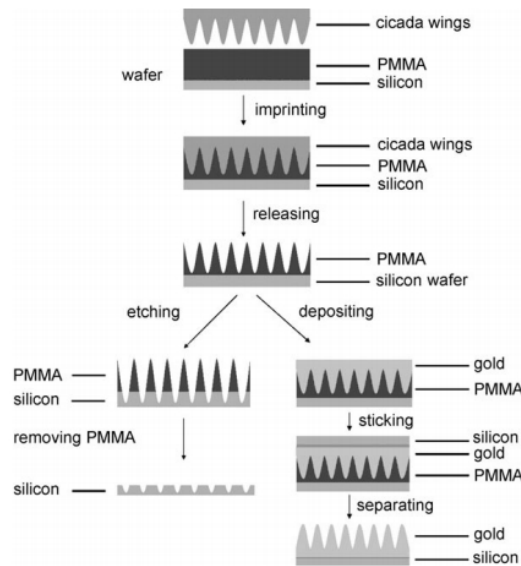


Figure 7.2: Nanoimprint lithography using cicada wings as stamps.^[58]

7.2 Electrospinning

Electrospinning involves the use of an electrostatic force to draw thin (from nanoscale to microscale) fibers with a viscous polymer liquid on a substrate. The method was briefly mentioned in Section 4.2. Water CAs as high as 172° and very low CAH have been reported for such surfaces when a highly hydrophobic polymer is used.^[20] By changing the process parameters, fibers can adapt shapes ranging from uniform cylinders to globules, and this makes it possible to fabricate surfaces with a dual-scale roughness. Although some polymers are hydrophobic enough to form a superhydrophobic surface, additional coatings are often necessary. For this purpose, fluorine-based materials are frequently used. A surface with porous electrospun fluorinated fibers is depicted in Figure 7.3a.

7.3 Phase Separation

If a stable multi-component liquid mixture becomes unstable due to cooling or a change in pressure, then the phases will begin to separate. A bicontinuous network is formed, and if one of the phases becomes solid in the process (e.g. block copolymer films), then the remaining liquid phase can be removed. The result is a three-dimensional porous network, like the one in Figure 7.3b. If the resulting wetting properties are not good enough, superhydrophobicity can sometimes be induced by applying an additional coating. Phase separation is a cheap and simple way of producing superhydrophobic materials.^[20]

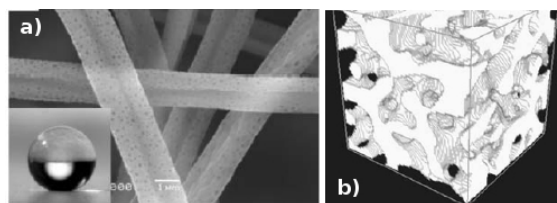


Figure 7.3: (a) Porous electrospun fluorinated fibers. Scale bar: $1\mu\text{m}$. (b) Model of a bicontinuous structure due to phase separation.^[20]

7.4 Layer-by-Layer Assembly

By utilizing the attraction between electrostatically charged particles, one can form a multilayer structure by sequentially dipping a substrate in a positive and a negative polyelectrolyte. For example, using the polymers polyallylamine hydrochloride (PAH) and poly(acrylic acid) (PAA) will generate a microporous surface that can be coated with silica nanoparticles to make it superhydrophobic.^[20]

7.5 Etching and Anodic Oxidation

Narita et al. fabricated superhydrophobic surfaces by using electrolytic etching to form micro-sized pits in an Al substrate, subsequently using anodic oxidation to generate nano-sized pits superimposed on the microstructure, and finally functionalizing the surface with a fluoroalkylsilane.^[20] The same method can also be used on other metals, such as zinc, copper, and polycrystalline metals.

7.6 Etching and Spin-Coating

Among the most frequently used substrates in icephobicity testing are panels made from Al or Al alloys. Micro- and/or nanoroughness can be created on such substrates for example through immersion in a hydrochloric acid solution. After cleaning and drying the rough surface, a hydrophobic chemical can be applied for example through spin-coating. Common solutions are based on silicon rubber mixed with hydrocarbons like hexane to reduce the viscosity.^[15] Nanopowders made from oxides like TiO₂ or CeO₂ are typically added to the solution to superimpose a nano roughness, something that will usually both increase the water CA and decrease the CAH. The solution must be stirred well before deposition on the surface. After coating, the residual solvents must be removed through a heat bake.

A schematic view of one possible fabrication process is shown in Figure 7.4.

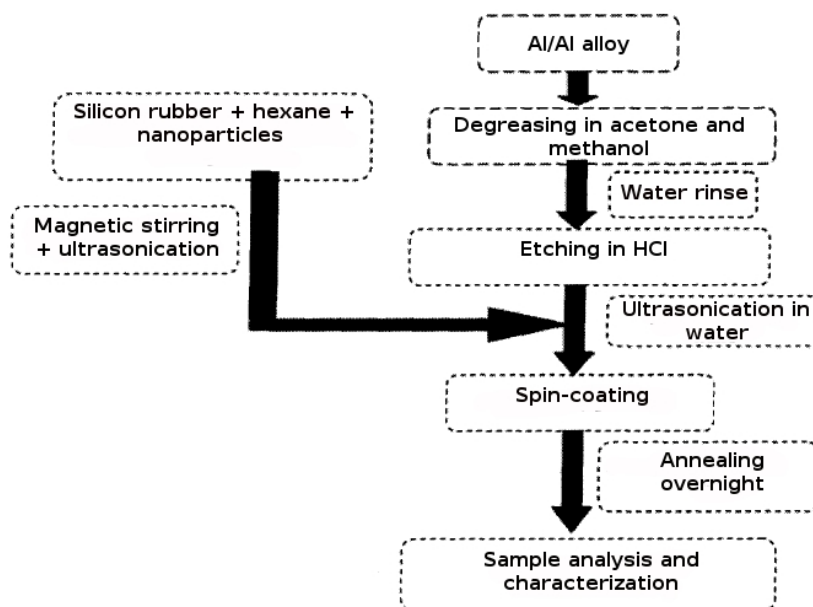


Figure 7.4: Schematic overview of the preparation of nanopowder-incorporated Si rubber coatings on rough Al substrates.^[15]

7.7 Superhydrophobic Coating Made from Candle Soot

Deng et al.^[86] developed a simple way to make robust, transparent and superhydrophobic surfaces. They first held a glass slide above the flame of a paraffin candle, so that it was covered by a layer of black candle soot (see Figure 7.5a). The SEM micrographs in Figure 7.5b and 7.5c reveal that the soot layer consists of a fractal-like network made up of carbon particles with a typical diameter of 30-40 nm. To make the structure more robust, CVD was used to deposit a 20 ± 5 nm thick shell of silica on top of the soot layer. The next step consisted in calcinating the carbon/silica network at 600°C for 2 h in air. This caused the carbon core to combust, thereby reducing the shell thickness, but the layer roughness and texture was retained. Lastly, to reduce the surface energy, the hydrophilic silica layer was coated with a layer of semi-fluorinated silane, again using CVD. The resulting surface demonstrated a water CA of $165\pm 1^\circ$, and a tilt angle smaller than 1° .

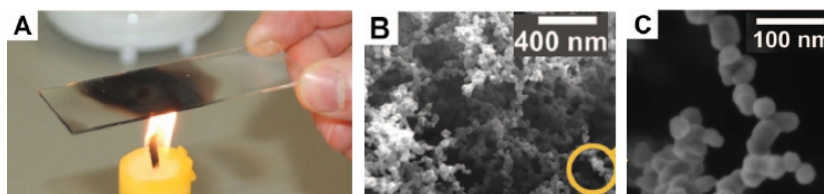


Figure 7.5: (a) A glass slide is held above the flame of a paraffin candle to form a soot layer, (b) SEM micrograph of the soot layer, (c) high-resolution SEM micrograph showing a single chain of carbon particles.^[86]

Since this type of superhydrophobic coating is transparent, it may be a promising candidate for applications on glass surfaces such as windows, touch screens, and goggles.

7.8 Graphene Nanomeshes (GNMs)

Since this thesis involves simulations of wetting on so-called *graphene nanomeshes* (GNMs), a discussion on the nature and fabrication of this material is included here.

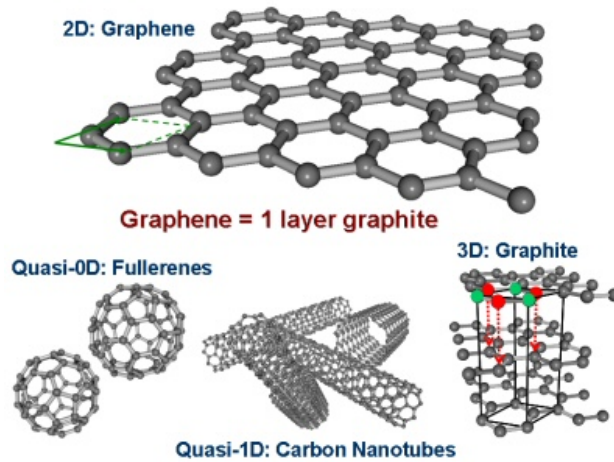


Figure 7.6: Visualization of a graphene layer, carbon fullerenes, carbon nanotubes, and graphite.^[67]

7.8.1 Graphene and GNM

Graphene is an allotrope of carbon, and consists of a single layer of sp^2 -bonded carbon atoms packed into a two-dimensional honeycomb lattice. It is the structural base of several more complex carbon allotropes, including fullerenes (graphene layers wrapped up into spheres), nanotubes (graphene layers rolled into tubes), and graphite (stacked graphene layers). These allotropes are shown in Figure 7.6.

The bond-length between adjacent carbon atoms in a graphene layer is approximately 0.142 nm. When several graphene layers are combined to form graphite, the interplanar spacing is ca. 0.335 nm. This means that a stack of 3 million graphene layers would be only 1 mm thick!

As electrons in graphene can travel very large distances without being scattered, it is believed to have a significant potential for application in fast electronic components.^[68] However, graphene is a semimetal with a zero bandgap, and cannot be used for effective field-effect transistors operating at room temperature without opening up the bandgap.

Bai et al.^[75] showed that it is possible to open up the bandgap of graphene by punching into it an array of nanoscale holes. They named their structures graphene nanomeshes (GNMs). GNMs can consist of a single graphene layer, or of several graphene layers stacked together. Since a solid covered with a GNM has a nanorough surface with a closed-cell structure, they may be an interesting candidate for application in superhydrophobic and icephobic coatings.

Graphene has a relatively high surface energy (with a CA of 84-86°).^[77] To make the surface more hydrophobic, one can coat it with a layer of a low surface energy material (like PTFE).

7.8.2 Production of GNMs

Bai et. al.^[75] prepared their nanomeshes using *block copolymer lithography*. This is a scalable method that has been used increasingly for patterning nanoscale features in polymers, silicon and metal, and it allows us to design and fabricate GNMs in a rational way. The periodicity (the center-to-center distance between two neighbouring nanoholes) and the hole diameter can be tuned with high precision, and the neck widths (the smallest edge-to-edge distance between two neighboring nanoholes) can be as small as 5 nm. Bai et. al. varied these parameters to tune the on-off ratio, i.e., the ratio between the currents when the device is switched on and when it is switched off. For our purpose, however, the periodicity and the hole diameter will be tuned to see how it influences the wetting properties of the surface in MD simulations.

The fabrication route of Bai et. al. is shown schematically in Figure 7.7. One starts off with a graphene layer on top of a silicon oxide substrate. The graphene film can be obtained for example through chemical exfoliation or chemical vapor deposition (CVD).^[76] A thin layer of SiO_x is then evaporated onto the graphene layer using an electron beam evaporator. This functions both as a protection layer and as a grafting substrate for the subsequent patterning. The surface is then functionalized with a 30-35 nm poly(styrene-*block*-methyl methacrylate) (P(S-*b*-MMA)) block copolymer thin film by spin coating and annealing. This block copolymer is made up of blocks of two different polymerized monomers—polystyrene (PS) and polymethylmethacrylate (PMMA)—that form distinct domain structures due to phase separation during solidification. The relative volume fraction determines whether the resulting domains are spheres, cylinders or lamellae.

The block copolymer films fabricated by Bai et al. have cylindrical domains normal to the surface that are used as the etching template. After etching, holes can be punched into the graphene layer by means of a CHF₃-based reactive ion etch (RIE) process followed by oxygen plasma etch.

Micrographs captured during the nanomesh fabrication process are shown in Figure 7.8. The centre-to-centre distance between adjacent PMMA domains was found to be ~39 nm when using P(S-*b*-MMA) with a molecular weight of 77,000 g mol⁻¹ and a PS:PMMA volume ratio of 70:30. The neck width of the final GNM structure can be adjusted with controlled over-etching, as shown in the TEM micrographs in Figure 7.9a,e, Figure 7.9b,f, and Figure 7.9c,g. The periodicity (and the neck width) can be changed by

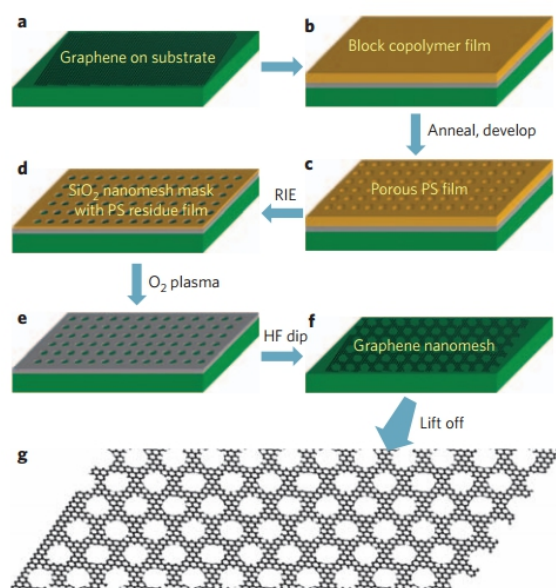


Figure 7.7: Fabrication of a GNM. a) Graphene flake on a silicon oxide substrate. b) The graphene flake is covered with a thin layer of evaporated SiO_x and a thin film of spin-coated block-copolymer P(S-*b*-MMA). c) The block-copolymer film is annealed and developed, leaving the porous PS matrix as the nanomesh template for further patterning. d) RIE is used to penetrate the oxide layer, partially degrade the PS film, and form the SiO_x nanomesh hard mask. e) Graphene in the exposed area is etched away by O₂ plasma. f) The oxide is removed with an HF dip. g) The GNM is removed from the silicon oxide by etching away the underlying substrate.^[75]

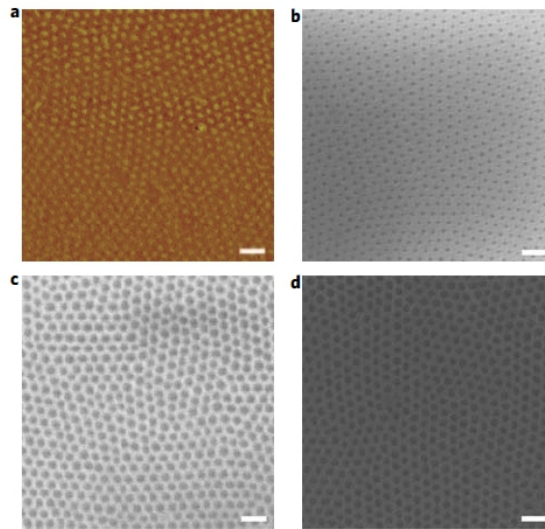


Figure 7.8: a) AFM image of the annealed P(S-*b*-MMA) thin film on graphene, with clearly visible PMMA domains arranged in a hexagonal fashion in the PS matrix. b) SEM image of the PS film after selectively etching away the PMMA domains. c) SEM image of the SiO_x nanomesh mask after reactive ion etching with the PS mask. d) SEM image of the GNM structure after removing the top SiO_x mesh mask.^[75]

using a block copolymer of a different weight, as shown in Figure 7.9d,h.

With even more aggressive over-etching than that shown in these TEM micrographs, the research group was able to achieve neck widths as small as ~ 5 nm. Aiming at such small neck widths may be problematic, as some necks are likely to break due to non-uniformity. Further optimization of the block copolymer self-assembly process could make them feasible to produce, however. But then again, there is the problem with mechanical stability.

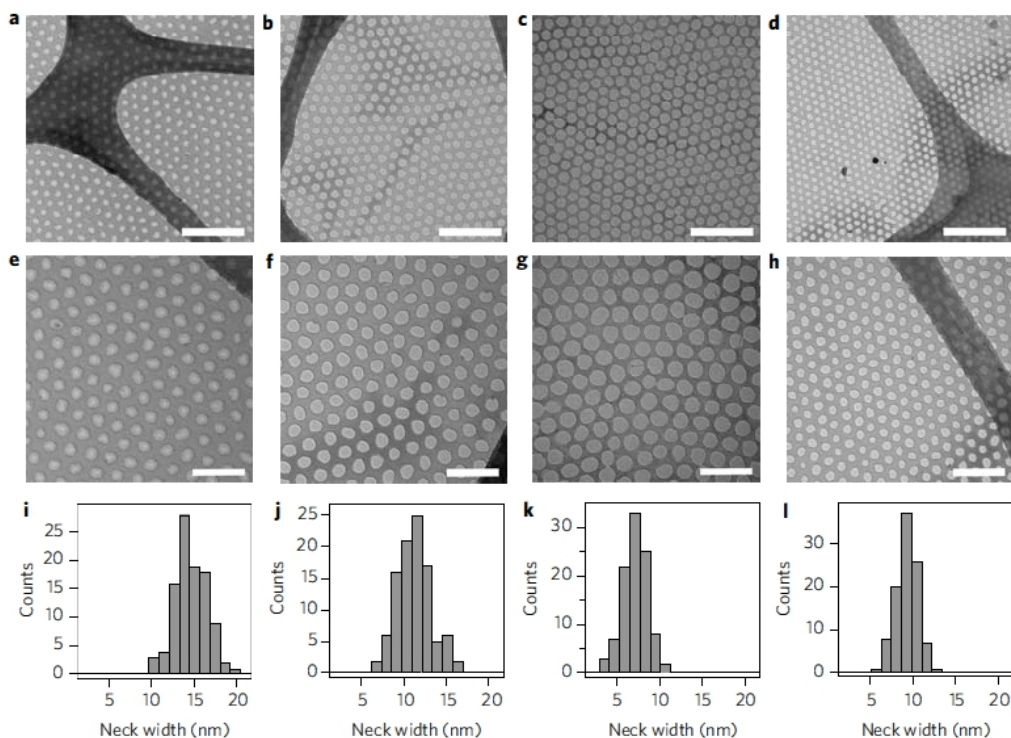


Figure 7.9: a),e) TEM images of a GNM with a periodicity of 39 nm and an average neck width of 14.6 nm obtained with block copolymer P(S-*b*-MMA) of a molecular weight of 77,000 g mol⁻¹. b),f) A GNM with a periodicity of 39 nm and an average neck width of 11.2 nm obtained with controlled over-etching. c),g) A GNM with a periodicity of 39 nm and an average neck width of 7.1 nm obtained with additional over-etching. d),h) A GNM with a periodicity of 27 nm and an average neck width of 9.3 nm obtained with block copolymer P(S-*b*-MMA) of a molecular weight of 47,700 g mol⁻¹. Scale bars: 200 nm (a-d) and 100 nm (e-h). i)-l) histograms of the GNM neck widths. Standard deviations are 2.0, 1.9, 1.5, and 1.3 nm, respectively.^[75]

Chapter 8

Condensation Theory

8.1 What is Condensation?

It is well known that water may come into contact with a surface not only by projection or deposition, but also by condensation. Condensation is the change of state from gaseous phase into liquid phase. Among the examples that can be experienced in our daily lives, are condensation of water droplets from our breath on cold windows, and dew on grass blades in the morning.

Water condensation starts by the formation of molecular clusters either within its gaseous volume—like the formation of rain droplets within clouds—or at the contact between the gaseous phase and a surface. This is known as *nucleation*. It commonly occurs when air is cooled below the *dew point*, i.e., the temperature at a constant pressure at which the air can no longer hold all the moisture it contains.

When water droplets condense on a cold surface, the nucleation is followed by the growth of isolated water droplets. Later on the coalescence of adjacent water droplets will increase the growth rate.

8.2 Growth Laws

At the early stage, when the surface coverage is low and the droplets are isolated, the droplet radius grows as

$$\langle R \rangle \sim t^{1/D_d} , \quad (8.1)$$

where t is the time and D_d is the *droplet dimensionality*, i.e., the the number of dimensions in which the droplet may grow.^[78] When the droplet growth is not constrained in any direction, D_d equals to three, and the isolated droplets grow as

$$\langle R \rangle \sim t^{1/3} . \quad (8.2)$$

At this initial stage of the growth process, the droplets are circular or just slightly non-circular.

At the intermediate and late stage, when coalescence can no longer be neglected, the droplet radius grows as

$$\langle R \rangle \sim t^{1/(D_d - D_s)} . \quad (8.3)$$

Here, D_s is the *substrate dimensionality*, i.e., the number of dimensions in which coalescence may occur. This is usually equal to two, and consequently, when neither the droplet growth nor the droplet coalescence are constrained, the droplets grow as

$$\langle R \rangle \sim t . \quad (8.4)$$

Both the nucleation rate and the droplet growth rate are slower on hydrophobic surfaces than on hydrophilic ones.^[78]

8.3 How Condensation Affects Wettability

Recent studies have shown that the lotus leaf will lose its superhydrophobic properties if water is able to condensate between the hair-like structure on its surface.^[80] Water droplets impinging on such surfaces will have a greater tendency to stick to the surface instead of readily rolling off even at very small angles. Cheng and Rodak^[80] performed an experiment whereby water was condensed on a lotus leaf by facing the hydrophobic side of the leaf above a beaker of boiling water, and placing an ice cube on the other side of the leaf to aid in the condensation. The setup was left running for ten minutes, and during this time span very small water droplets were observed to condense on the surface. As the condensation continued, some of the droplets merged to form bigger droplets. In contrast to droplets placed on the surface, these condensation droplets did not readily roll off the surface, but instead formed "sticky" droplets.

Droplets (ca. 2 mm in diameter) were then placed onto different parts of the leaf's condensed regions. While some of the droplets rolled off in the typical fashion of water droplets placed on a lotus leaf, other droplets came to a stop and remained adhered even at a tilt angle close to 90° (see Figure 8.1a). The loss of superhydrophobicity was also demonstrated by measured advancing and receding CAs of 148° and 38°, respectively. Moreover, some of the droplets were even observed to spread out, wetting the leaf at CAs

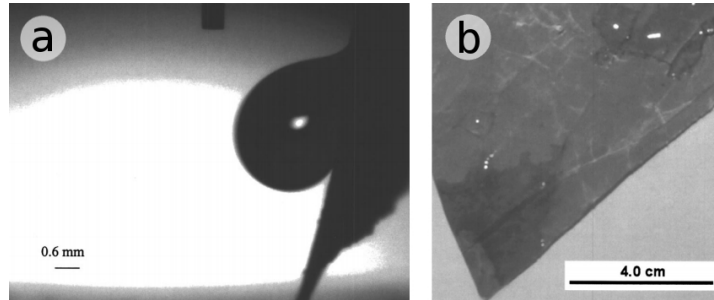


Figure 8.1: (a) A water droplet placed on a condensed lotus leaf, tilted at $73,7^\circ$. (b) Hydrophilic regions on a condensed lotus leaf. ^[80]

as low as 40 to 60° (see Figure 8.1b). This experiment shows that water condensation can not only ruin the superhydrophobic properties of a surface, but can even render it hydrophilic.

To explain the different droplet behavior on dry lotus leaves and on lotus leaves exposed to water condensation, Cheng and Rodak proposed a model based on liquids in contact with composite surfaces. When microscopic water droplets are entrapped in the features of the lotus leaf during condensation, we get a composite surface consisting of solid and water instead of solid and air. Since the CA is 0° for water droplets in water and 180° for water droplets in air, the observed CA will decrease. The actual CA obtained depends on the fraction of the surface area that is filled with water (see Figure 8.2).

Xiao and Cheng^[79] conducted a condensation experiment and found their porous carbon films to lose superhydrophobicity upon condensation. After ten minutes of condensation while the surface temperature was kept constant at 5°C , the CA of a freshly deposited water droplet had decreased from 150° to 130° (see Figure 8.3), and the tilt angle had increased from 5° to 90° . After 20 minutes of condensation, fresh water droplets immediately spread and wetted the surface with a CA close to 0° . Lastly, the surface was heated with air to remove the water from the pores. The high-CA droplet shape was then restored, and so was the low CAH.

Lau et al.^[77] reported the creation of a superhydrophobic surface consisting of a forest of untangled and vertically aligned carbon nanotube pillars functionalized with a low surface energy poly(tetrafluoroethylene)(PTFE) coating (see Figure 8.4). The forest was deposited with a plasma enhanced chemical vapor deposition (PECVD) technique, allowing for precise control of both the height and the diameter of the CNTs. The surface had 10 MWNTs per μm^2 , the mean tube diameter being 50 nm (before coating) and the mean height being 2 μm .

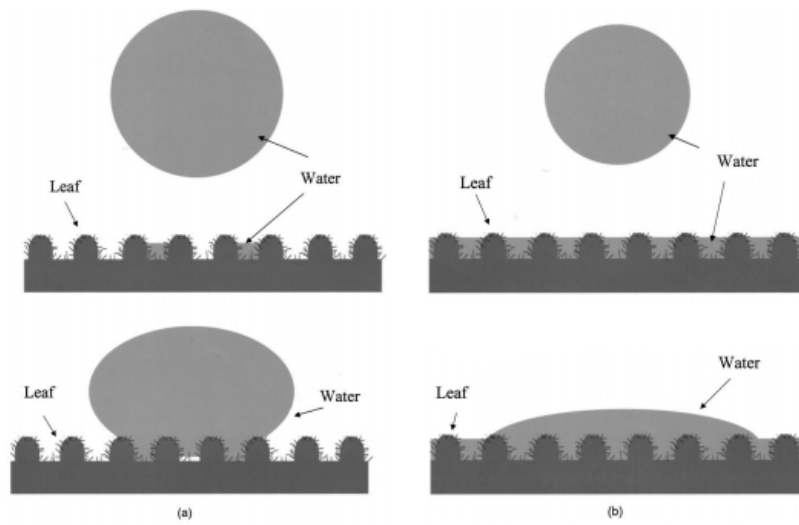


Figure 8.2: Schematic illustration of a water droplet on a lotus leaf following water condensation: (a) A droplet on a region with a small fraction of the surface area filled with water. (b) A droplet on a region with a large fraction of the surface area filled with water. ^[80]

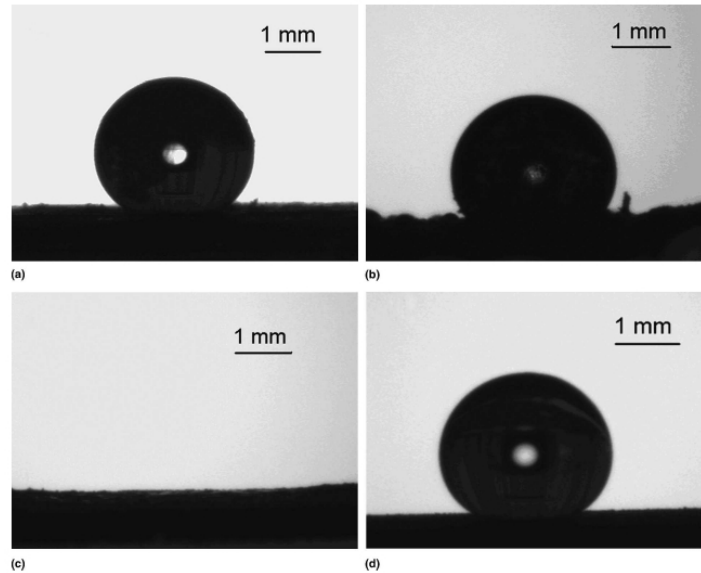


Figure 8.3: Water droplets on a carbon film (a) before condensation, with a CA of about 150° ; (b) after 10 minutes of condensation, with a CA of about 130° ; (c) after 20 minutes of condensation, with a CA of about 0° ; (d) after drying, with the CA restored to about 150° . ^[79]

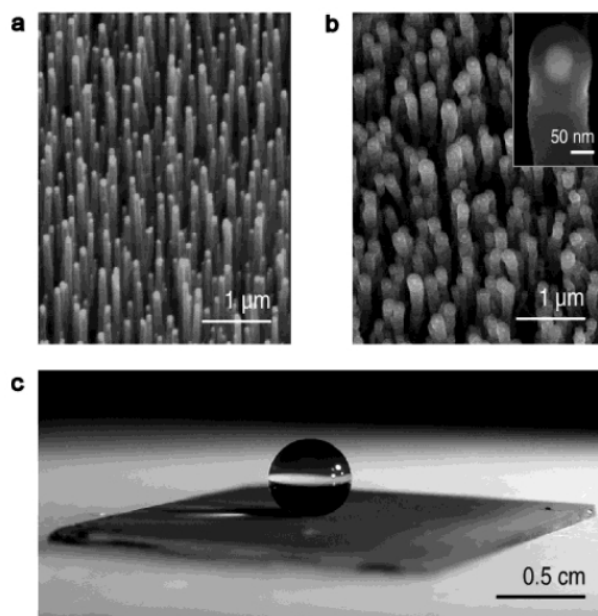


Figure 8.4: SEM micrographs of a CNT forest. (a) As-grown forest prepared by PECVD, (b) PTFE-coated forest, and (c) a water droplet suspended on the PTFE-coated forest.^[77]

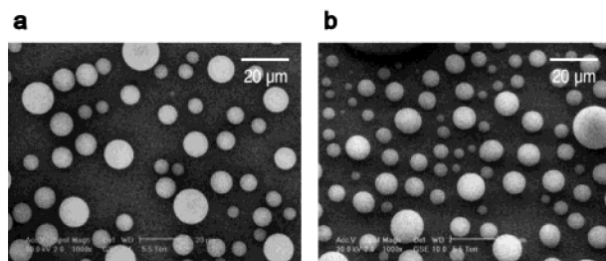


Figure 8.5: ESEM micrographs of water droplets on CNT forest. (a) Water droplets on a PTFE-coated forest, (b) 15° tilt view.^[77]

Vapor condensation experiments inside an ESEM confirmed that the surface was superhydrophobic even for water droplets down to the micrometer range. Precisely controlling the water vapor pressure and the temperature of the sample stage allowed for imaging of the formation of micrometer-sized water droplets, as seen in Figure 8.5. These were clearly suspended on top of the nanotubes. Repeated condensation-evaporation cycles rendered the nanotube structure unchanged.

Narhe et al.^[83] studied the condensation process on dual scale superhydrophobic zinc surfaces coated with hydroxide zinc carbonate (HZC) by chemical bath deposition. The hydrophobicity was tuned by changing the deposition time. Their results showed that water condensation on superhydrophobic surfaces is determined by the surface chemistry and not the surface texture, as the nucleation events occur at a much smaller length scale than that the surface roughness. Therefore, condensation on superhydrophobic and smooth surfaces follow the same droplet growth laws, with a transition from Cassie-Baxter to Wenzel wetting states at long times.

It has proven to be very difficult to sustain the C-B state on a surface exposed to condensation. Even on lotus leaves, condensate droplets tend to penetrate the surface texture and stick to the cooled surface. Chen et al.^[84] showed that it is possible to retain the Cassie-Baxter state during and after condensation on a dual-scale structure mimicking the lotus leaf. The surface they used consisted of squarely positioned micropillars etched in silicon, covered with CNT nanopillars with an average length of 400 nm, and a hydrophobic parylene coating. The ambient air was kept at ca. 19°C, having a relative humidity of 74 percent. This corresponds to a dew point of 14°C. The surface was then cooled to ca. 5° to induce condensation. The condensation of water vapor onto the substrate was visualized by an optical microscope and a CCD camera.

The condensation on the dual-scale surface was compared with conden-

sation on single-scale surfaces, with microscale or nanoscale roughness only. The importance of the dual-scale structure is shown in Figure 8.6. The condensation droplets appeared to conform to the surface roughness both on the microtexture only (Figure 8.6a and 8.6b) and on the nanotexture only (Figure 8.6c and 8.6d) surfaces, indicated by the flat and irregular drop shapes. On the dual-scale surface, however, the shape of the coalesced droplets remained almost spherical after 1 hour of condensation—indicating the Cassie-Baxter state. The only exceptions were droplets smaller than the micropillar separation.

These observations can be explained by the thermodynamic criterion introduced in Chapter 4. The C-B state is thermodynamically more stable when the CA on a smooth surface is greater than the critical CA, expressed by Equation 4.1. Thus, a stable C-B state can be achieved in either of two ways: (i) Decreasing the critical CA by using a surface with lower liquid-solid fractional area, f_1 ; and higher roughness, r . (ii) Increasing the Young's CA, e.g. by coating. With a parylene coating, the Young's CA is $91 \pm 4^\circ$. This was well below the critical CA of both the microstructure only (120°) and the nanostructure only (96°) surfaces, but comparable to the two-tier structure (94°). Because of this, the Wenzel state is the energetically favorable state on the one-tier structures, while the C-B state is favored on the two-tier structure.

On a micro-nano two-tier structure, the liquid-solid fractional area is given by $f_{1,mn} = f_{1,m} \cdot f_{1,n}$; and the roughness is given by $r_{mn} = r_m \cdot r_n$. Here, the subscripts mn , m , and n denote the micro-nano, the micro, and the nano structure, respectively.

Narhe et al.^[83] investigated water condensation on zinc surfaces treated with hydroxide zinc carbonate (HZC) by chemical bath deposition. The surface roughness, and hence the effective water contact angle, was tuned from 75 to 150° by varying the deposition time. Figure 8.7 shows SEM micrographs of what the surface typically looked like after 24 h deposition. One can see that it consists of a micro-flowers-like structure superimposed by interconnected nano sheets. Calculations based on an estimation of the surface roughness, showed that the Wenzel state should be the most stable configuration on this surface.

The condensation experiments took place in a condensation chamber, where the substrates were fixed on a electrolytic copper plate. The air flow was saturated with water vapor with a fixed flow rate of 0.6 Lmin^{-1} , and the temperature difference between the saturated water vapor ($23 \pm 0.5^\circ\text{C}$) and the substrate was $8 \pm 0.5^\circ\text{C}$. The heterogeneous nucleation process that followed was captured with a video camera attached to an optical microscope.

This group also found the growth laws governing the condensation process

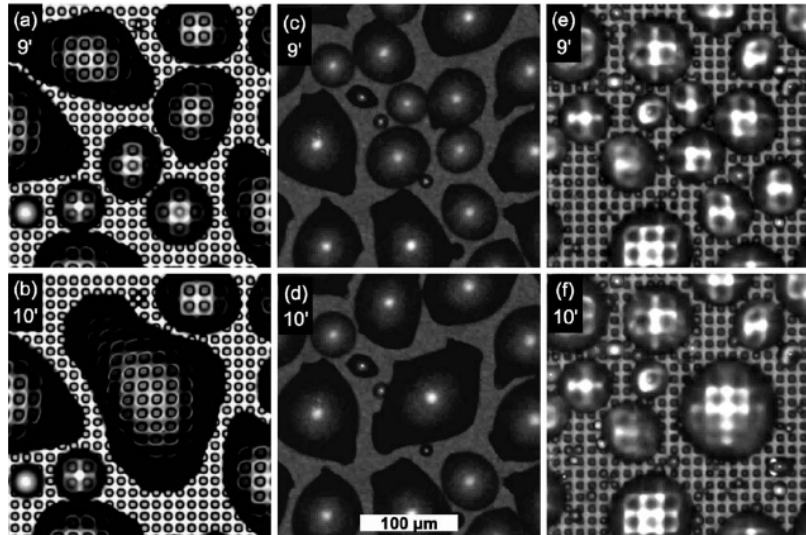


Figure 8.6: Coalescence of condensate droplets on parylene-coated surfaces. (a)-(b) One-tier structure with only micropillars, (c)-(d) one-tier structure with only nanopillars, (e)-(f) two-tier structure with nanopillars superimposed on micropillars.^[84]

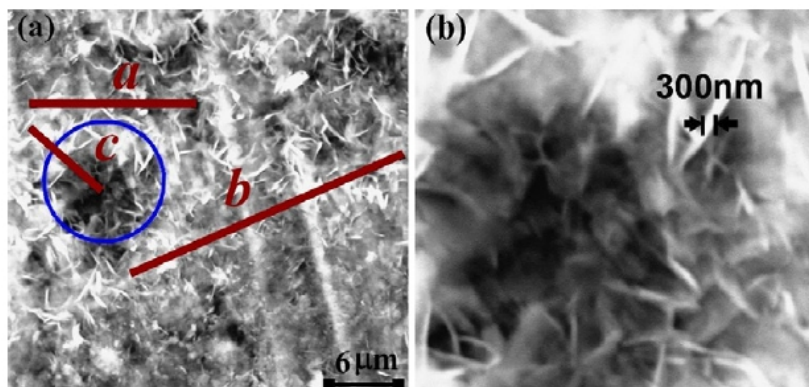


Figure 8.7: (a) SEM micrograph of a zinc surface showing the micro-flower-like structure of the surface ($a=12\mu\text{m}$, $b=25\mu\text{m}$, $c=10\mu\text{m}$), (b) ca. 300 nm thick nano-sheets superimposed on the micro-structure.^[83]

to be similar to those previously found for smooth surfaces, as the nucleation events occur on much smaller length scales than those of the surface texture. The *initial stage* (typically $t < 3$ min) is characterized by drop nucleation while the droplet surface coverage (the ratio of the total the area covered by droplets to the total surface area) is low. The coalescence is negligible, and the droplets grow mainly by direct vapor condensation, following the radius growth law $\langle R \rangle \sim t^{1/3}$.

In the *intermediate stage* (typically $3 < t < 8$ min), the surface coverage increased significantly, and two different kinds of droplets were observed. Droplets condensing on the micro-flowers were bright and almost spherically shaped, corresponding to a high apparent CA (indicating Cassie-Baxter mode), while droplets condensing in the vicinity of the micro-flowers were comparatively darker and more irregularly shaped, corresponding to a low apparent CA (suggesting Wenzel mode). The Cassie-Baxter droplets remained in this state until they coalesced with neighboring droplets. The coalescence energy is sufficient to overcome the energy barrier from the metastable state, making transition to the global energy minimum possible. A mixed case was also observed, where one side of the droplet was dark (Wenzel mode) and the other was bright (Cassie-Baxter mode).

In the *last stage* (typically $11 < t < 16$ min), coalescence is the dominant factor determining the droplet growth, and the droplets grow as $\langle R \rangle \sim t$. The surface coverage converges to a value determined by the apparent CA^[83]

$$\epsilon_{\infty} = 1 - \frac{\theta^*}{200}, \quad (8.5)$$

in this case to a value between 0.62 and 0.65. The surface coverage at long times can therefore be used to estimate the mean apparent CA.

Condensate droplets will normally have to be removed by external forces. Gravitational removal is the most obvious solution, but this approach depends on the orientation of the device. Moreover, it will only affect droplets larger than the capillary length. But Boreyko and Chen^[85] showed that on surfaces where the C-B state represents the global energy minimum (CA $\sim 170^\circ$), the released surface energy due to droplet coalescence can cause spontaneous droplet removal whereby coalescing droplets jump off the surface at a speed as high as 1 ms^{-1} . This is possible since the pinning forces along the droplet contact line are much lower. The images in Figure 8.8 show how condensate droplets on a hydrophobic surface continued to grow, while they were automatically removed on the superhydrophobic surface, leaving behind a large dry area after ca. 20 min (This is not likely to occur on surfaces with sub-zero temperature, however, as the droplets will freeze before spontaneous removal can occur). Besides, the surface coverage flattens out at ca. 0.6 on

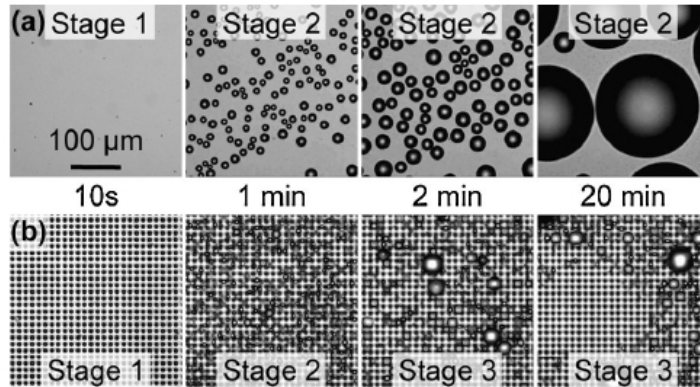


Figure 8.8: (a) Dropwise condensation on a smooth hydrophobic surface (a), and on a rough superhydrophobic surface with visible micropillars (b).^[85]

the hydrophobic surface, compared to only 0.4 on the superhydrophobic one. Another difference is the droplet diameter, which reaches a maximum of ca. $5 \mu\text{m}$ on the superhydrophobic surface, while the growth shows no tendency to slow down even after reaching $100 \mu\text{m}$ on the hydrophobic surface. (However, this so-called autonomous droplet removal was observed only when the coalescence involved at least one drop with diameter $\geq 10 \mu\text{m}$.)

We have seen that the actually realized droplet state is not necessarily the lowest-energy state. If the Wenzel state is the lowest-energy state, transition from the Cassie-Baxter state requires the droplet to overcome an energy barrier, for example with kinetic energy. However, when a droplet is formed by condensation, Wenzel droplets may form directly.

Chapter 9

Simulation Theory

As computers have become more powerful, it has become possible to model wetting and freezing of water droplets on solid surfaces using numerical methods. Information can now be obtained which would have been hard—or even impossible—to gather from physical lab experiments. Scientists can study systems at temperatures and pressures which may be expensive to obtain with real experiments, and it is possible to apply external forces, add or withdraw particles, and move particles—or collections of particles—with high accuracy. Ultimately, the main restriction on the use of modern simulation programs is the scientist’s creativity. This chapter provides a short introduction to the basics of molecular dynamics simulations, and how programs like LAMMPS can be used to simulate wetting of liquid droplets on solid surfaces.

9.1 Basic Theory of Molecular Dynamics

Molecular Dynamics (MD) has been developed as an important computer tool aimed at simulating the motion and interaction of atoms and molecules in areas such as fluid dynamics and material science. During a simulation, each atom in the system is constrained by a surrounding potential that approximates the short-range and long-range interactions with its neighboring atoms, and it abides by Newtonian physics.

The most commonly used potential in MD simulations is the Lennard-Jones potential, abbreviated L-J, and sometimes also known as the 6-12 potential or the 12-6 potential. For a pair of atoms separated by a distance r , the L-J potential is given by^[69]

$$\phi_{L-J}(r) = 4\epsilon \left[\left(\frac{\sigma}{r} \right)^{12} - \left(\frac{\sigma}{r} \right)^6 \right], \quad (9.1)$$

where ϵ and σ are material specific constants chosen to fit the physical properties of the materials in the system.

Lennard-Jones interactions are repulsive at short range, where the $\sim (1/r)^{12}$ term dominates, and attractive at moderate and long distances, where the $\sim (1/r)^6$ term dominates. The L-J potential is shown graphically in Figure 9.1. The graphical meaning of the parameters ϵ and σ are also indicated. ϵ is the depth of the potential well, and σ is the distance of zero potential. The force at a given interaction distance is equal to the slope of the potential curve. The origin of the repulsive forces at very short distances is the Pauli principle, which states that no two electrons can reside in the same state. The origin of the repulsive forces are van der Waals interactions, induced by dipole-dipole interactions due to fluctuating dipoles.

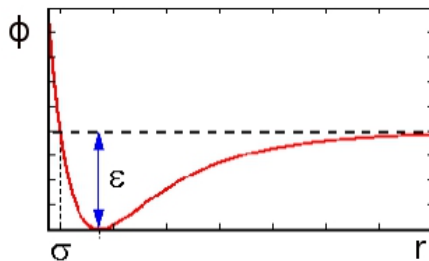


Figure 9.1: The Lennard-Jones potential.^[70]

The total potential for a single particle i in a system with N particles is found by summing over all the pairwise interactions with all other particles j in the system:^[69]

$$\Phi_{L-J,i}(r) = \sum_{j \neq i}^N \phi_{L-J}(\mathbf{r}_{i,j}) . \quad (9.2)$$

Here, $\mathbf{r}_{i,j}$ is the distance between i and j . The net force on particle j can then be calculated as the spacial gradient of the potential,^[69]

$$\mathbf{F}_i = -\nabla \Phi_{L-J,i} , \quad (9.3)$$

and this force is then used to calculate the trajectory of the particle using Newton's second law, $\mathbf{F} = m \cdot \mathbf{a}$, where \mathbf{F} is the force acting upon the particle, m is the mass, and \mathbf{a} is the acceleration. The trajectory of each particle is calculated stepwise, and when the equations of motion for all the particles are integrated, one can obtain the system's structure and properties at the macroscopic level.

In a system with N particles, there are $(N - 1)!$ pairs of interaction that must be considered. This amounts to extremely large numbers even in systems with a two-digit number of atoms. To make the calculations less computer expensive, MD programs therefore truncate the potential to zero at a range where the interactions have become negligible.

The steps of MD simulations are summarized in the flow chart in Figure 9.2.

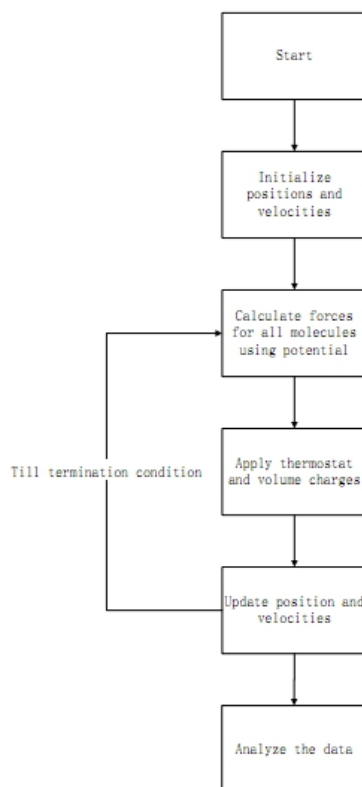


Figure 9.2: Process flow chart for MD simulations. [71]

9.2 Software

LAMMPS (Large-scale Atomic/Molecular Massively Parallel Simulator) is an open source MD program from Sandia National Laboratories that can be used to model systems consisting of a few atoms up to billions of particles. [72]

Visual Molecular Dynamics (VMD) is a visualization program that has been developed for viewing and analyzing the results of MD simulations, and

it supports LAMMPS trajectory files. VMD, too, is freely available online.^[73]

9.3 Wetting Simulation in LAMMPS

To get an idea of how LAMMPS can be used to simulate wetting, we will consider an experiment performed by X. Yong and L. T. Zhang,^[74] who studied nanoscale wetting on groove-patterned surfaces to find out whether the predictions of Wenzel and Cassie and Baxter are valid also at the nanoscale.

Their simulations involved a liquid mercury droplet consisting of approximately 2000 mercury atoms, with a radius of 18.5 Å; and a copper plate comprising seven layers of 150 x 150 Å² copper atoms arranged in an FCC structure with a lattice constant of 3.69 Å. Mercury was used as a liquid because it is a single atomic material and thus requires less computational time. The L-J potential was used, with liquid-liquid parameters $\epsilon_{ll} = 2.6453$ kcal/mol and $\sigma_{ll} = 2.61$; solid-solid parameters ϵ_{ss} ranging from 0.026453 to 2.6453 kcal/mol depending on the surface affinity for the liquid, and $\sigma_{ss} = 2.34$. The liquid-solid interactions were calculated as follows:

$$\sigma_{ls} = \sqrt{\sigma_{ss}\sigma_{ll}} \quad , \quad \epsilon_{ls} = \sqrt{\epsilon_{ss}\epsilon_{ll}} \quad . \quad (9.4)$$

The potential was truncated at $r_{tr} = 3.5\sigma_{ll}$.

Figure 9.3 shows the initial configuration of the system. The simulation

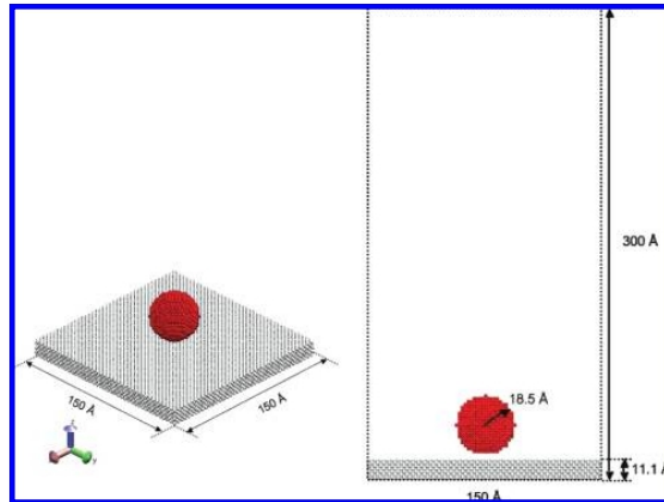


Figure 9.3: The initial configuration in the simulations performed by X. Yong and L. T. Zhang.^[74]

space is a box of size 150 x 150 x 300 Å. Periodic boundary conditions were used in the x and y directions, which means that any atom that crosses the boundary of the box will appear again at the opposite side with the same speed. In the z direction, reflective walls were used instead, to avoid particles showing up at the bottom of the substrate. In this way, the number of atoms in the simulation box was retained. The temperature was also kept constant by applying a so-called thermostat to fix the temperature at 700 K every time step. If a thermostat is not coupled to the system, cut-offs and rounding errors in the calculations can lead to energy fluctuations, and the system may heat up.

The so-called *Verlet algorithm* was used to calculate the positions and velocities of the atoms stepwise. On a rough surface, it may take up to 30 ns—corresponding to $6 \cdot 10^6$ time steps—to reach equilibrium.

When equilibrium was reached, the CA was estimated using the following geometrical relationships based on the geometric dimensions shown in Figure 9.4.^[74]

$$\theta = 2 \tan^{-1} \left(\frac{h}{r'} \right) \quad \text{if } h < r \quad (9.5)$$

$$\theta = 90^\circ + \sin^{-1} \frac{h - r}{r} \quad \text{if } h > r \quad (9.6)$$

Here, h and r are the height and radius of the droplet, respectively; and r' is the radius of the circular liquid-solid contact area.

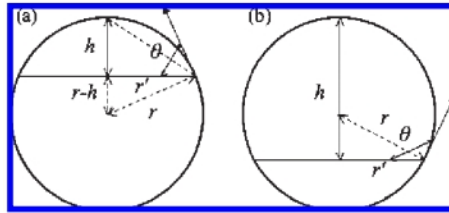


Figure 9.4: Parameters for CA evaluation for (a) a droplet with height smaller than its radius, and (b) a droplet with height larger than its radius.^[74]

The relative energy ϵ_r between ϵ_{sl} and ϵ_{ll} can be written $\epsilon_r = \sqrt{\epsilon_{ss}/\epsilon_{ll}}$. With $\epsilon_{ll} = 2.6453$ kcal/mol and ϵ_{ss} ranging from 0.026453 to 2.6453 kcal/mol, it means that ϵ_r is varied between 0.1 and 1. Low values of ϵ_r indicate low attraction of the liquid to the solid surface, and as we can see in the plot in Figure 9.5, the CA increased as ϵ_r was decreased. For $\epsilon_r < 0.4$, the surface

was intrinsically mercury-phobic. For $\epsilon_r > 0.4$, it was intrinsically mercury-philic.

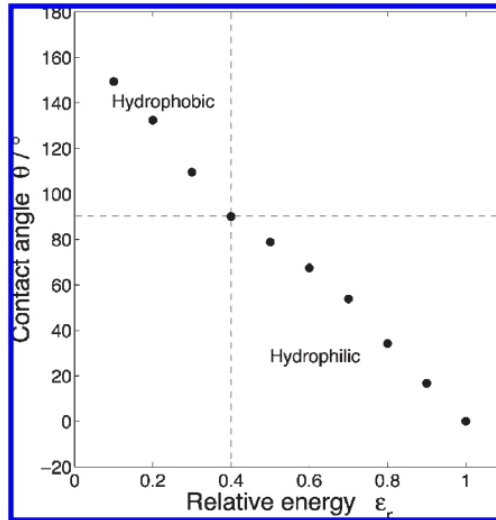


Figure 9.5: CA as a function of the relative energy parameter ϵ_r .^[74]

When the intrinsic CAs were known, surface roughness was introduced in the shape of grooves with width a , height b , and spacing c , as shown in Figure 9.6. CAs were measured for different values of roughness factor, R_f ,

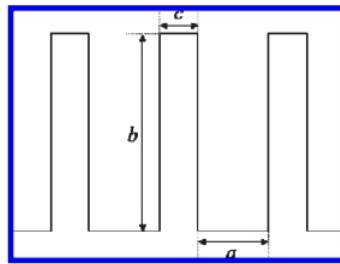


Figure 9.6: Surface structure with groove width a , groove height b , and spacing c between grooves.^[74]

and surface fraction of the liquid-solid interfaces, f_1 . With f_1 held constant at 0.5, the CAs were measured on an intrinsically mercury-phobic ($\epsilon_r = 0.3$) surface for different roughness values. R_f was varied between 1.25 and 4. The obtained results are plotted in the graph in Figure 9.7, where the wetting behavior predicted by the Wenzel and the Cassie-Baxter equations

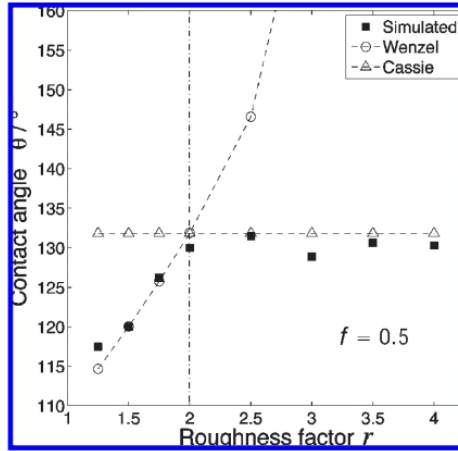


Figure 9.7: CA vs. roughness factor on a nanogrooved mercury-phobic surface with $f_1 = 0.5$, and comparison with predictions according to Wenzel and Cassie-Baxter.^[74]

are also included. As we can see, the measured CAs have a good match with those predicted by Wenzel and Cassie-Baxter. The CA increases with increasing roughness, in agreement with Wenzel's theory (see Figure 3.4), and there is a regime transition at a roughness factor of approximately 2, which is exactly what is predicted by Equation 4.1 when the intrinsic CA is 109.5° . The behavior for roughness > 2 is in good agreement with the Cassie-Baxter equation, despite small deviations due to liquid atoms that had penetrated into the grooves and caused partial wetting. A snapshot from a MD simulation of a droplet in the Cassie-Baxter state is shown in Figure 9.8.

The group also studied the effect of reducing the surface fraction f_1 while keeping the roughness factor constant. The CA as a function of f_1 proved to be consistent with the theories for small values of R_f , but partial wetting occurred for high values of R , which induced deviations from the Cassie-Baxter equation.

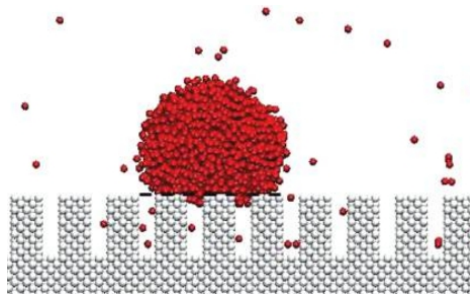


Figure 9.8: Snapshot of a MD simulation of a mercury droplet in contact with a mercury-phobic surface. $f_1 = 0.5$, $R \approx 3.5$, $CA = 130.6^\circ$. Some liquid particles have penetrated into the grooves and cause small deviations from the Cassie-Baxter equation.^[74]

Chapter 10

Graphene Nanomesh Simulations

As indicated in the preceding chapters, most of the research in the field of superhydrophobic surfaces has involved surfaces with open-cell structures, e.g. pillar-like surfaces and surfaces with bumps and valleys. In Chapter 5 we saw that surfaces with closed cells have a comparative advantage in that they are better at resisting transition to the Wenzel state due to pressure. To investigate the wetting properties of closed-cell structures further, I decided to take a closer look using LAMMPS simulations. As far as I know, this has not been done before.

The goal was to find if wetting on closed-cell structures (GNMs) satisfies the theories of Wenzel and Cassie-Baxter, which have later been modified by Zheng et al.^[46] More precisely: How do GNMs perform relative to the performance of pillared surfaces having the same solid-liquid fractional area f_1 and roughness scale S ?

Freezing of water is a very complex phenomenon, and simulations are very cumbersome to carry out in LAMMPS. Therefore, the the simulations in this thesis only involve liquid water. Moreover, since the simulations involve static wetting only, and since the water droplets used are nanometer-sized; the effect of pressure and gravity is negligible. Thus, should the closed-cell structures prove to perform better (or worse) than the open-cell structures, the discrepancies will have to be explained in other ways.

If discrepancies are found, the theories of Wenzel and Cassie-Baxter (and later modifications) may have to be modified to take into consideration the effect of replacing open cells with closed cells. Disregarding the entrapment of air, which leads to enhanced resistance to pressure, perhaps the most striking difference between closed-cell GNMs and the open-cell pillars is the fact that the center of curvature of the three-phase intersection line is located

on the pillar tops in the case of the open-cell surface, and above the holes in the case of the closed-cell structures (see Figure 10.1). To explain possible discrepancies in the wetting behavior, one option would be to investigate the wetting in terms of geometrical differences like this.

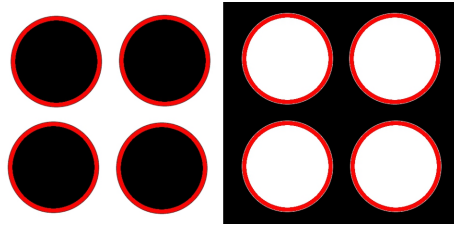


Figure 10.1: Schematic depiction of an open-cell structure (left) and a closed-cell structure (right). The red circles mark the three-phase intersection lines.

10.1 Preparation

The first thing that had to be done in the preparation of the simulations was to model the graphene sheets. This was done using the programming language Fortran 90 in a Linux text editor. A stack of five graphene sheets was made. The source code is given in Appendix A. The distances $\sqrt{3} \cdot CC$ and $1.5 \cdot CC$ are shown in Figure 10.2.

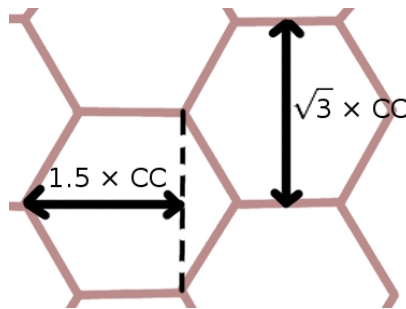


Figure 10.2: Schematic drawing of a graphene sheet, showing the distances used in the simulations.

CC is the intermolecular distance between two adjacent carbon atoms in the graphene sheet, i.e., 0.142 nm. The size of each graphene layer was chosen to be $60 \cdot 1.5 \cdot CC$ by $50 \cdot \sqrt{3} \cdot CC$, i.e. ca. 12.8 by 12.3 nm. This

corresponds to 6000 carbon atoms in each layer. The graphene layers were stacked in a regular AB fashion, as shown in Figure 10.3.

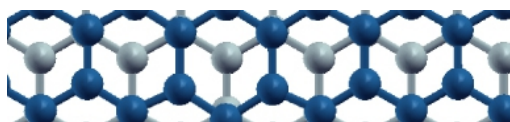


Figure 10.3: Top view of two graphene sheets stacked in a regular AB fashion.^[87]

The Fortran code was then compiled to an executable file and converted to a so-called XYZ file, which is a format that specifies the molecular geometry of the system by assigning the appropriate atomic symbol and Cartesian coordinates to each atom. The first line gives the total number of atoms that will be read, and each of the following lines contains the Cartesian coordinates of a single carbon atom with units in Ångströms. The first few lines were:

```

30000
C      -63.54500    -60.87293    0.00000
C      -63.54500    -58.41341    0.00000
C      -63.54500    -55.95390    0.00000
C      -63.54500    -53.49439    0.00000

```

To add water to the system, an MD simulation package called GROMACS (GROningen MACHine for Chemical Simulations) was used. To make the XYZ file compatible with Gromacs, it had to be converted to a .gro file. This was achieved with another Fortran code, which is also given in Appendix A. The .gro file is very similar to the XYZ file, as can be seen for the first few lines:

```

Generated by changing xyz to gro
30000
1CNT   C      1   -6.354   -6.087   0.000
1CNT   C      2   -6.354   -5.841   0.000
1CNT   C      3   -6.354   -5.595   0.000
1CNT   C      4   -6.354   -5.349   0.000

```

A GROMACS command was then used to generate a box of water. The system now consisted of 30 000 carbon atoms and 8 461 water molecules.

Yet another Fortran code was then used to cut the holes in the stack of graphene layers, generating graphene nanomeshes (GNMs). This code can also be found in Appendix A. Different output files were generated by changing the hole radius and the distance between the holes in the Fortran code.

Finally, another Fortran code was used to convert the .gro files to LAMMPS files. This too is given in Appendix A. The output files produced were now ready for simulations in LAMMPS. To make LAMMPS simulations possible, an input file containing all the information about the simulation must be provided. The input file gives details about the types of atoms and interactions in the system, as well as details about different restrictions. Both the input file and the code used to convert the .gro files to LAMMPS files can be found in Appendix A.

For explanations of the different commands in the in file, take a look at the LAMMPS user manual.^[88]

10.2 Experimental

First, a simulation was run on a stack of graphene sheets without holes in them. This way, an intrinsic CA of 90.9° was found. In other words, the surface was slightly hydrophobic. A total of 33 simulations were then run on the GNM surfaces.

The first series consisted of seven simulations (simulation 1 through 7 in the Results section), whereby the roughness scale S was kept constant at 0.200, while the solid-liquid fractional interface f_1 was varied from 0.920 to 0.613. Ideally, one would like to reduce f_1 to values way below this, but due to the small scale of the system, the reduction of the neck width between the holes is constrained by the atomic structure of the graphene sheets.

In the second series, another seven simulations were run (simulation 8 through 14). These simulations were identical to simulation 1 through 7, except that the potential was changed so that the intrinsic water CA on the graphene surface was 137.4° instead of 90.9° . This corresponds to treating the surface with a hydrophobic coating.

In the third series, three simulations were done whereby the potential was changed to *decrease* the intrinsic CA to 46.2° (simulation 15 through 17). This corresponds to applying a hydrophilic coating to the surface. S was still kept constant at 0.200, while f_1 was varied from 0.741 to 0.613.

In the fourth series, ten simulations (simulation 18 through 27) were run on an "inverted" GNM surface, i.e. a surface with pillars instead of holes. Just like in simulations 1 through 7, the roughness scale was kept constant at

0.200, while the solid-liquid fractional interface was varied—this time from 0.080 to 0.627.

In the fifth and last series, six simulations (simulation 28 through 33) were done on surfaces with the standard water CA of 90.9° . This time f_1 was kept constant at 0.613, while S was varied. Simulation 7 was included in in this series for comparison, so that the roughness scale was varied from 0.200 to 0.440

The trajectory files generated by the LAMMPS simulations were visualized and analyzed with VMD (Visual molecular dynamics). Figure 10.4 shows what the water-graphene system looks like in a three-dimensional perspective.

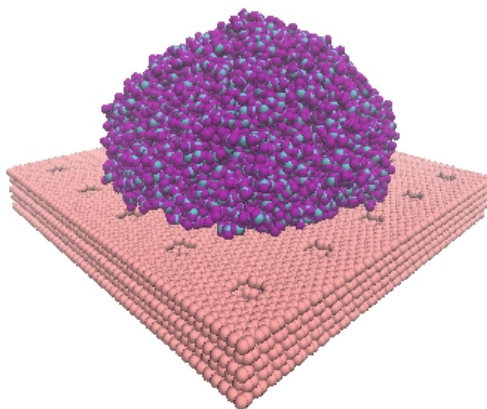


Figure 10.4: Screenshot of a VMD simulation.

To calculate the contact angle, it was first necessary to determine a droplet boundary based on the density of water in the system. Droplet boundary points were set where the density of water was half that of the bulk density. A curve was then fitted to these boundary points, and from this curve a contact angle could be computed.

10.3 Results

All of the VMD screenshots shown in this section are taken when the water-graphene systems have reached thermodynamic equilibrium.

10.3.1 Simulations with Surfaces of Constant S and Varying f_1

Simulation series 1: Standard GNM surfaces

Top view and side view screenshots from the simulations with constant S and varying f_1 are shown in Figure 10.5. To keep S constant, the same hole radius was used in all the simulations (0.4 nm), while the neck width was changed to vary f_1 .

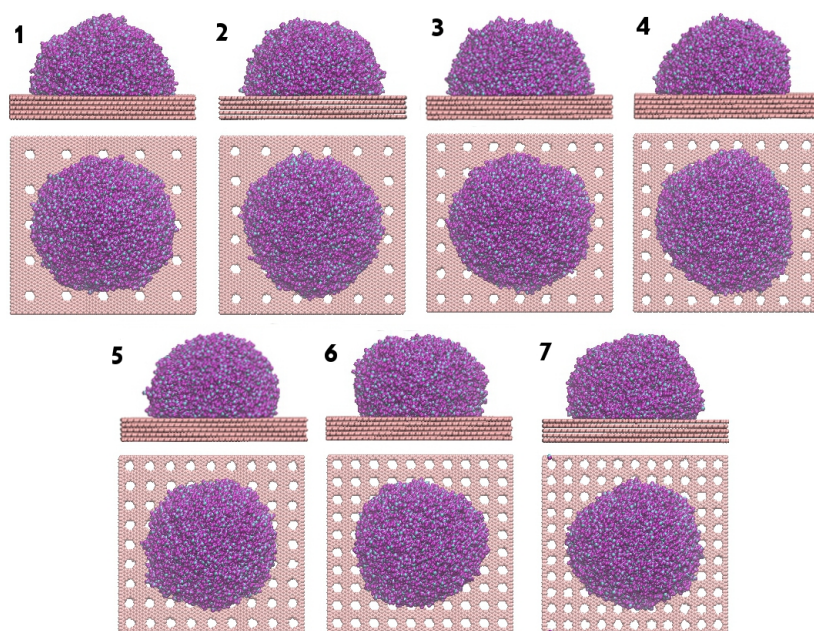


Figure 10.5: Simulation 1-7. S is kept constant while f_1 is decreasing.

Design parameters and measured CAs for the water-GNM systems in simulation series 1 are shown in Table 10.1.

Simulation series 2: GNM surfaces with increased hydrophobicity

Top view and side view screenshots from the simulations with constant S and varying f_1 on a surface with an intrinsic water CA of 137.4° are shown in Figure 10.6. Once again, the hole radius was 0.4 nm in all the simulations, while the neck width was changed to vary f_1 .

	f_1	S	CA	$\cos(\text{CA}) + 1$
Simulation 1	0.920	0.200	94.65	0.9189
Simulation 2	0.885	0.200	97.13	0.8760
Simulation 3	0.843	0.200	97.74	0.8654
Simulation 4	0.795	0.200	101.65	0.7981
Simulation 5	0.741	0.200	108.03	0.6904
Simulation 6	0.680	0.200	111.16	0.6390
Simulation 7	0.613	0.200	114.32	0.5882

Table 10.1: Design parameters and measured CAs for the simulations in the first series.

	f_1	S	CA	$\cos(\text{CA}) + 1$
Simulation 8	0.920	0.200	137.56	0.2620
Simulation 9	0.885	0.200	139.73	0.2370
Simulation 10	0.843	0.200	138.91	0.2463
Simulation 11	0.795	0.200	142.99	0.2015
Simulation 12	0.741	0.200	144.43	0.1866
Simulation 13	0.680	0.200	146.71	0.1641
Simulation 14	0.613	0.200	150.38	0.1307

Table 10.2: Design parameters and measured CAs for the simulations in the second series.

Design parameters and measured CAs for the water-GNM systems in simulation series 2 are shown in Table 10.2.

Simulation series 3: GNM surfaces with decreased hydrophobicity

Top view and side view screenshots from the simulations with constant S and varying f_1 on a surface with a decreased water CA of 46.2° are shown in Figure 10.7. This time too, the hole radius was 0.4 nm in all the simulations, while the neck width was varied.

Design parameters and measured CAs for the water-GNM systems in simulation series 3 are shown in Table 10.3.

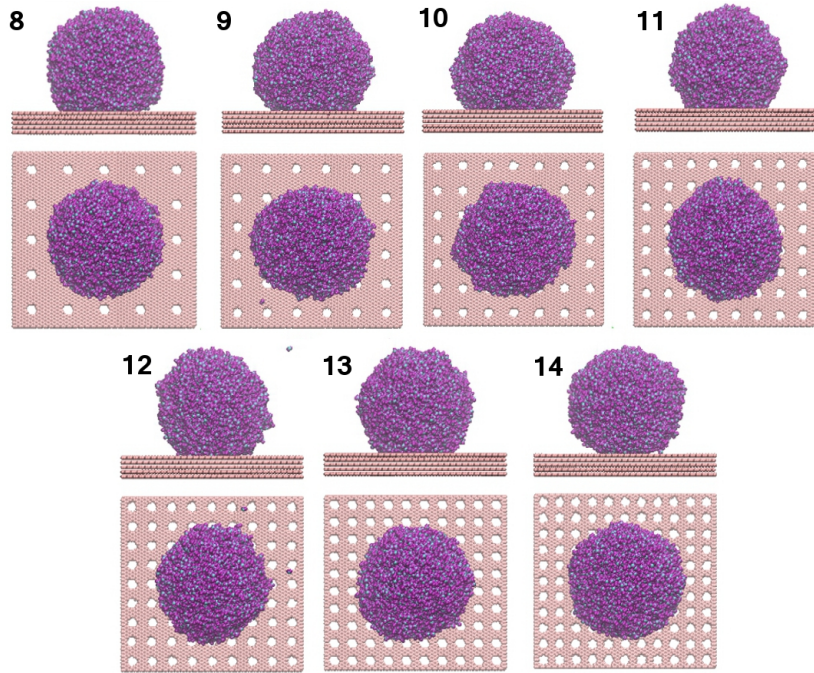


Figure 10.6: Simulation 8-14. S is kept constant while f_1 is decreasing.

Simulation series 4: Pillared surfaces

Top view and side view screenshots from the simulations with constant S and varying f_1 on a surface with pillars instead of holes are shown in Figure 10.8. The pillar radius was 0.4 nm in all the simulations, while the pillar density was varied to change f_1 .

Design parameters and measured CAs for the water-GNM systems in simulation series 4 are shown in Table 10.4.

	f_1	S	CA	$\cos(\text{CA}) + 1$
Simulation 15	0.741	0.200	76.36	1.2358
Simulation 16	0.680	0.200	81.40	1.1496
Simulation 17	0.613	0.200	86.53	1.0605

Table 10.3: Design parameters and measured CAs for the simulations in the third series.

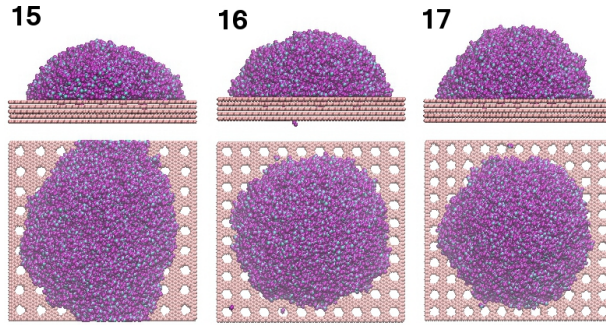


Figure 10.7: Simulation 15-17. S is kept constant while f_1 is decreasing.

	f_1	S	CA	$\cos(\text{CA}) + 1$
Simulation 18	0.080	0.200	151.31	0.1228
Simulation 19	0.115	0.200	152.24	0.1151
Simulation 20	0.157	0.200	147.92	0.1527
Simulation 21	0.205	0.200	145.14	0.1795
Simulation 22	0.259	0.200	138.20	0.2545
Simulation 23	0.320	0.200	135.24	0.2899
Simulation 24	0.387	0.200	131.49	0.3376
Simulation 25	0.461	0.200	127.96	0.3849
Simulation 26	0.541	0.200	123.57	0.4470
Simulation 27	0.627	0.200	116.35	0.5561

Table 10.4: Design parameters and measured CAs for the simulations in the fourth series.

Graphical representation of simulation series 1-4

The results from simulation 1 through 27 are shown graphically in Figure 10.9. $1 + \cos\theta^*$ is plotted against f_1 (θ^* is the measured CA in each simulation). The three dotted lines have slope $1 + \cos\theta$, where θ is the intrinsic water CA.

	f_1	S	CA	$\cos(\text{CA}) + 1$
Simulation 28	0.613	0.440	108.73	0.6789
Simulation 29	0.613	0.367	108.44	0.6837
Simulation 30	0.613	0.314	119.20	0.5122
Simulation 31	0.613	0.275	117.71	0.5351
Simulation 32	0.613	0.244	115.59	0.5681
Simulation 33	0.613	0.220	115.05	0.5767
Simulation 7	0.613	0.200	114.32	0.5882

Table 10.5: Design parameters and measured CAs for the simulations in the fifth series.

10.3.2 Simulations with Surfaces of Constant f_1 and Varying S

Simulation series 5: Standard GNM surfaces

Top view and side view screenshots from the simulations with constant f_1 and varying S are shown in Figure 10.10. The intrinsic water CA is 90.9° .

Design parameters and measured CAs for the water-GNM systems in simulation series 5 are shown in Table 10.5.

Graphical representation of simulation series 5

The results from simulation 28 through 33 plus 7 are shown graphically in Figure 10.11. The estimated CA in each simulation is plotted against the roughness scale (S).

10.4 Discussion

As can be seen in the graph in Figure 10.9, for constant values of S , the CA increases steadily with decreasing f_1 , according to the theory of Cassie and Baxter. The few deviations from this rule can be explained by measurement uncertainties since only one simulation was run for each value of f_1 .

As expected, the surfaces with increased intrinsic hydrophobicity (series 2) performed better than the standard GNM surfaces (series 1), while the surfaces with decreased hydrophobicity (series 3) performed worse. The data from all the four simulation series seem to follow the linear trend predicted by Equation 3.11: $1 + \cos \theta_{CB} = (1 + \cos \theta_Y)f_1$.

One of the goals in this thesis was to find out if closed-cell structures perform better than pillared surfaces with the same roughness scale. Judging by the comparison between simulation series 1 and 4, the answer is no. If the closed-cell GNM surfaces were superior, the black circles on the graph would follow a line with a steeper slope than that of the white circles. But as we can see, the data from both simulation series follow the same line. There is even a slight tendency for the pillared surfaces to perform better, but this can probably be explained by measurement uncertainties.

The conclusion is that the Cassie-Baxter equation applies also for nanodroplets on nanostructured surfaces, and that the geometrical differences between open-cell and closed-cell structures has no effect on the wettability. However, as we have seen, there are benefits by using closed-cell microstructures when dealing with larger droplets, as surfaces with such structures are better at resisting pressure.

The graph in Figure 10.11, on the other hand, does not seem to confirm the modified Cassie-Baxter equation developed by Zheng et. al.^[46] that takes into consideration the effect of scaling down the surface topography. According to Zheng et al., the CA should increase as S decreases toward a critical value l_{cr} , from where it will drop sharply. The reason for the lack of correspondence to theory here is probably that the droplets are too small. Each droplet covers just a few holes, and the line tension has little influence on the contact angle.

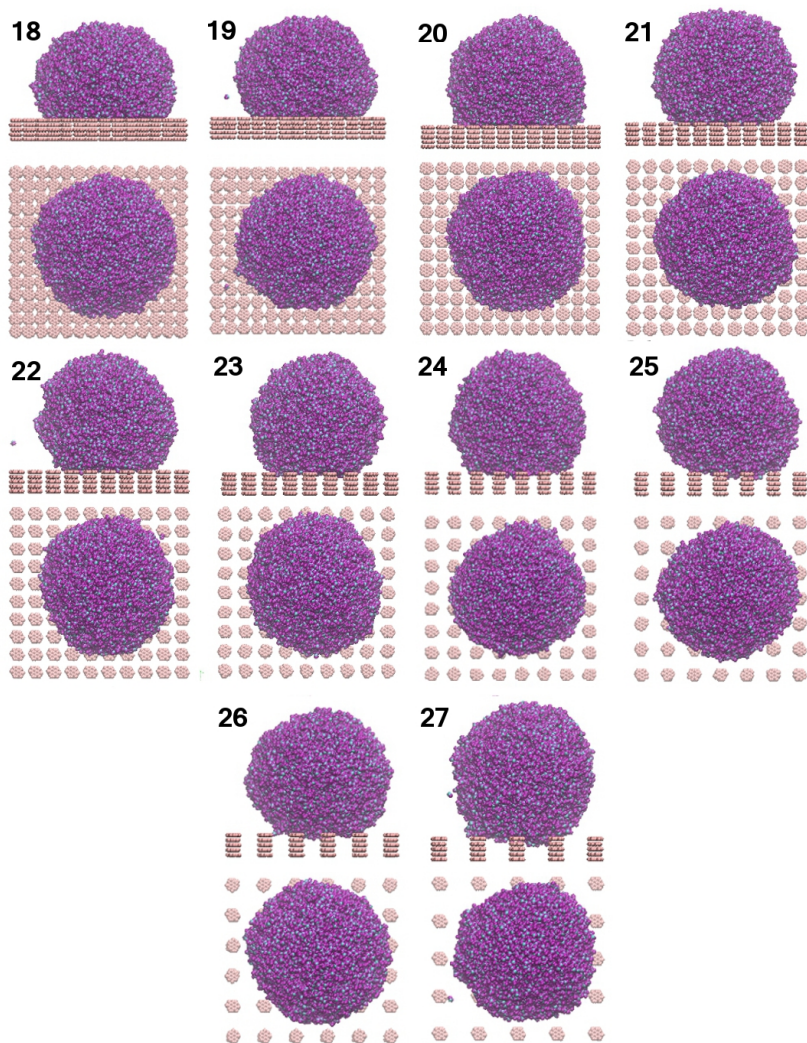


Figure 10.8: Simulation 18-27. S is kept constant while f_1 is decreasing.

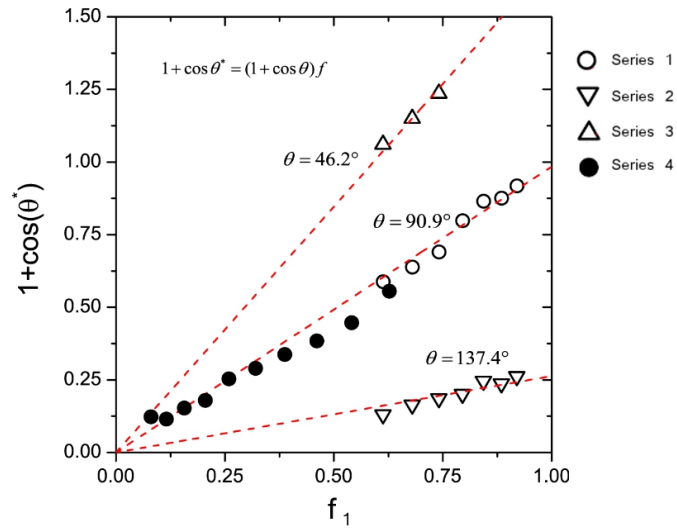


Figure 10.9: Graphical representation of the simulations with constant S and varying f_1 .

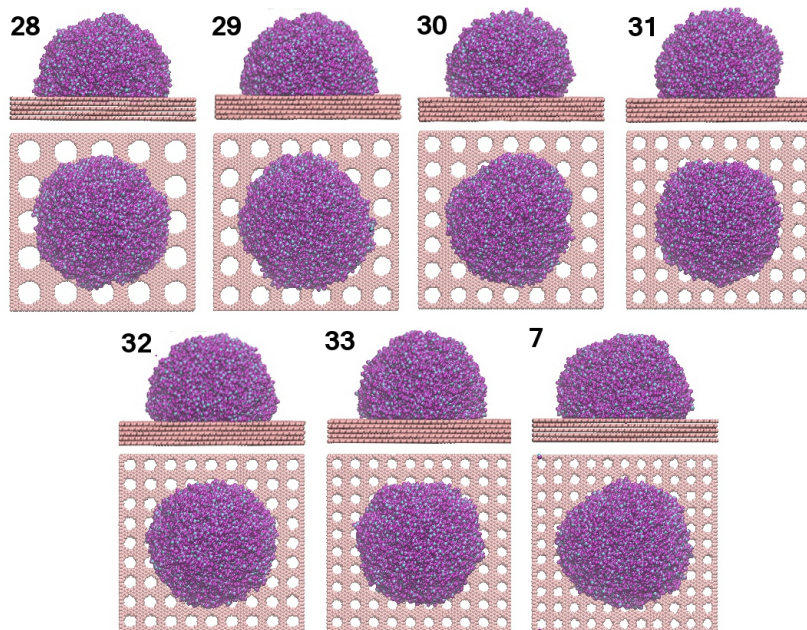


Figure 10.10: Simulation 28-33 plus 7. S is kept constant while f_1 is decreasing.

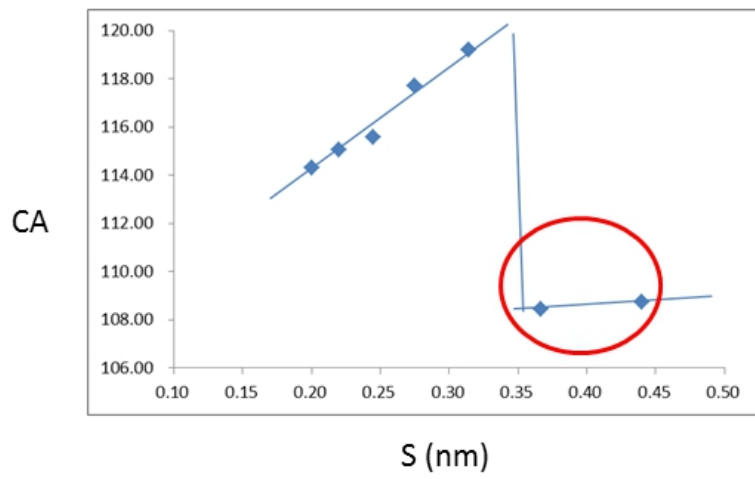


Figure 10.11: Graphical representation of the simulations with constant f_1 and varying S .

Chapter 11

Droplet Impact Experiments

In these experiments, the goal was to study the effect of water condensation on the behavior of impacting water droplets on a hydrophobic surface made from black silicon.

11.1 Preparation

In the preparation for the experiments, the condensation process was studied. A black silicon surface was attached to a Peltier plate (module number TEC1-3108, dimensions: 20 x 20 x 3.8mm) and put under a light microscopy as shown in Figure 11.1.

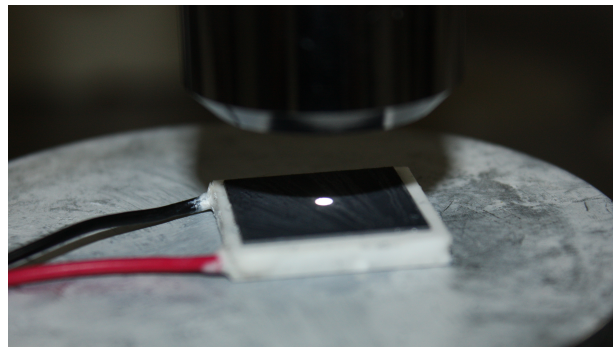


Figure 11.1: A peltier plate with a black silicon sample under a light microscopy.

Silicon is intrinsically hydrophilic, but since our sample had a high surface roughness and had been treated with octadecyltrichlorosilane (OTS) three months prior to the experiments, it was expected to be hydrophobic. To

confirm this, the CA and CAH of water on the substrate was measured using the sessile drop method. A droplet of ca. $2 \mu\text{L}$ was deposited on the substrate by means of a micro-syringe, and visualized using a CCD camera. The CA was found by analyzing the droplet in a drop shape analysis instrument from Powereach. Based on the average of six measurements, the static CA was estimated to be ca. 145° (Figure 11.2a). The advancing contact angle was obtained by pushing the droplet, while the receding contact angle was obtained by pulling it. The CAH seemed to be ca. 15° (Figure 11.2b).

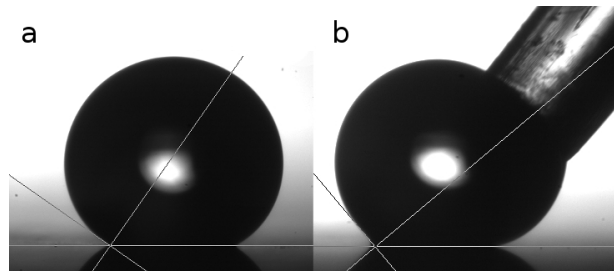


Figure 11.2: Screenshots from the CA (a) and CAH (b) measurements.

An SEM micrograph of the OTS-coated black silicon surface is shown in Figure 11.3.

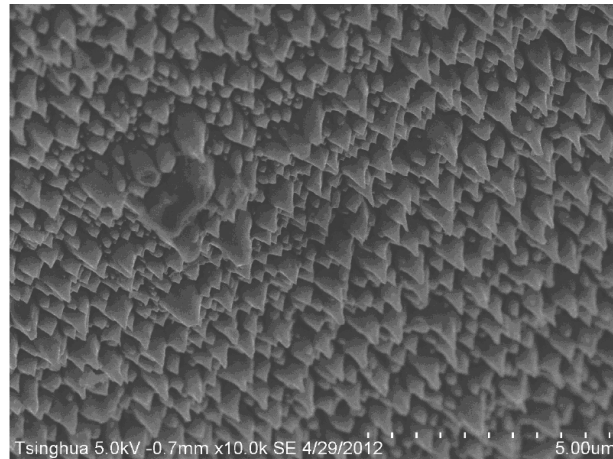


Figure 11.3: SEM micrograph of a rough black silicon surface coated with OTS.

After the sample was attached to the Peltier plate, it was cooled to a few degrees above 0°C by sending a current through the Peltier plate. When the

temperature was below the dew point, condensation initiated. The condensation process was then observed and recorded digitally. During the experiments, the room temperature and the humidity were 23°C and 55 percent, respectively.

Water was observed to start condensing almost immediately upon cooling. Digital snapshots from the condensation process are shown in Figure 11.4.

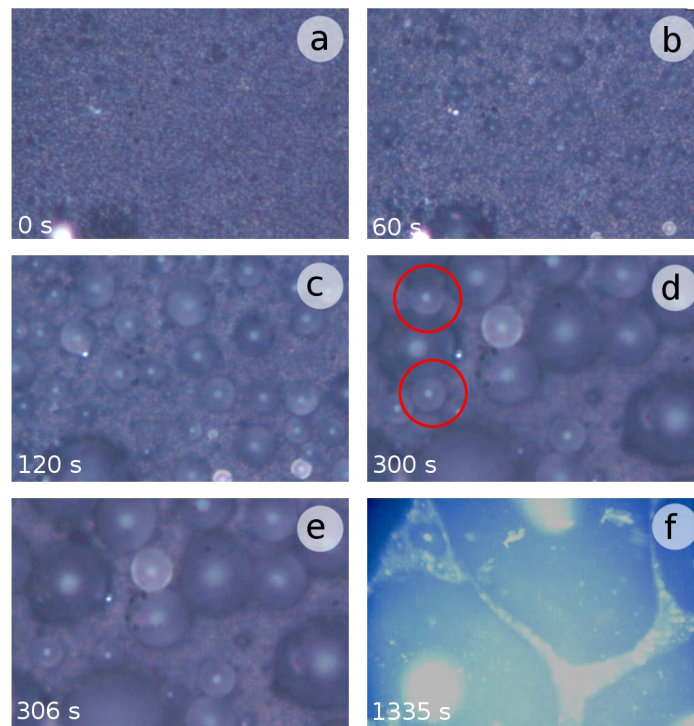


Figure 11.4: Snapshots from the condensation process. The droplets are in the micrometer range.

At the early stage, tiny water droplets were observed to nucleate on the surface (Figure 11.4b). The droplets grew in size, but as the surface coverage remained low, no coalescence was observed (Figure 11.4c). Some of the droplets were in the Wenzel state and others were in the Cassie-Baxter state. The two states were distinguishable by their color. A dark color tells us that the droplet is in the Wenzel state, while a lighter color indicates the Cassie-Baxter state.

As the condensation continued and the surface coverage increased, some of the droplets merged, forming larger droplets. Larger droplets were also observed to consume smaller ones. Figure 11.4d and 11.4e show how a large

droplet in the Wenzel state swallows two neighboring droplets in the Cassie-Baxter regime (encircled in red).

The condensation rate was observed to decrease with time, and after 22 minutes of water condensation, the surface was covered mostly with large Wenzel drops of irregular drop shape, and the total coverage was roughly 80-90 percent (Figure 11.4f). Blowing air over the surface did not generate transition to the Cassie-Baxter state. When the current was turned off, all of the water on the surface evaporated within seconds.

11.2 Experimental

The equipment setup is shown in Figure 11.5. The black silicon was attached to a peltier plate which was coupled to a MINIPA MSP-3053 DC-regulated Power supply. The other side of the peltier plate was attached to a system consisting of a metallic support and a cooling fan, designed to optimize heat removal. Water was transferred from a beaker through a plastic rubber, before water droplets with a diameter of ca. 2.5 mm were released approximately 15 cm above the sample, corresponding to an impact velocity of ca. 1.7 m/s. A lamp was used for illumination. The experiments were captured with a Photron FASTCAM SA3 high-speed CCD camera, and analyzed with a QCapture Pro software.

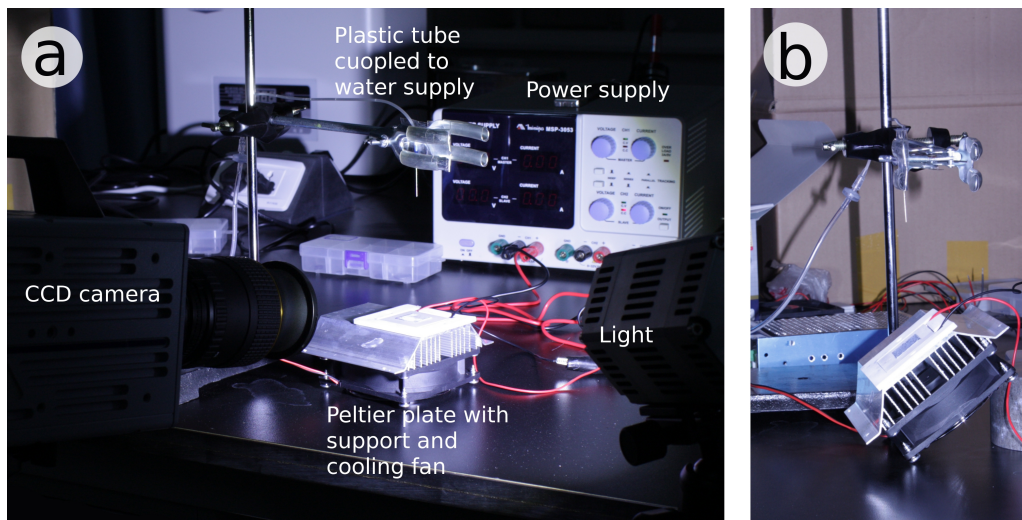


Figure 11.5: Experimental setup with (a) a horizontal surface, and (b) a tilted surface.

Four experiments were carried out. First, the droplet behavior was tested

on a horizontal surface (as shown in Figure 11.5a), both on a dry surface and on a surface exposed to condensation. Then, the droplet behavior was tested on a surface tilted 35° (as shown in Figure 11.5b), again both on a dry surface and on a surface exposed to condensation.

11.3 Results

On the dry and horizontal surface, the droplet expanded upon impact until it reached a maximum diameter of ca. 6.3 mm after ca. 0.003 s (Figure 11.6b). Then it contracted because of the surface tension, and eventually it bounced off the surface, ca. 0.016 s after the impact (Figure 11.6c). The droplet bounced two more times, before it underwent damped oscillations and finally came to a rest in the Cassie-Baxter state ca. 2 s after the first impact (Figure 11.6d).

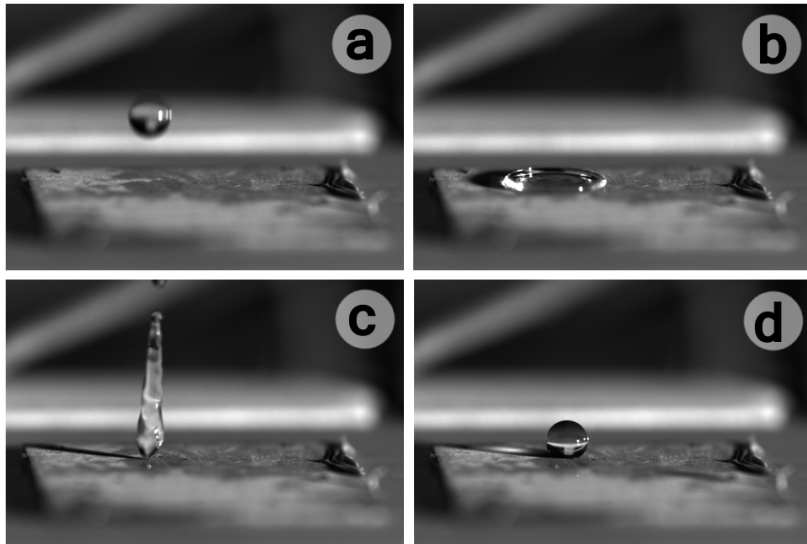


Figure 11.6: Droplet impact on a dry and horizontal surface.

On the horizontal surface with water condensation on it, the surface tension was not able to contract the droplet fully. The droplet expanded to a diameter of ca. 10.8 mm in 0.004 seconds (Figure 11.7b), and then contracted for another 0.043 s until its contact surface with the substrate was a disk with a diameter of ca. 5.1 mm. As the droplet contracted, it dragged with it the small condensate droplets on the surface, leaving behind a bright ring outside of its contact line with the substrate, as seen in Figure 11.7c.

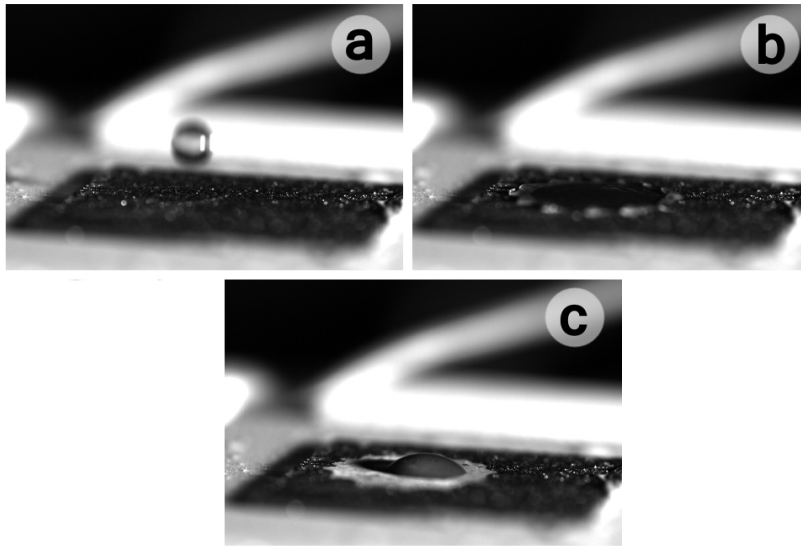


Figure 11.7: Droplet impact on a horizontal surface exposed to water condensation.

On the dry and tilted surface, the droplet started to expand until it reached its maximum diameter of ca. 5.9 mm ca. 0.003 s after the impact (Figure 11.8b). Another 0.010 s later, it jumped off the surface (Figure 11.8c). During the whole time in which the droplet was in contact with the surface, it slid down the plane. The point of impact and the point of departure were separated by ca. 7.7 mm.

On the tilted surface which had water condensation on it, the droplet expanded and reached its maximum diameter of ca. 9.5 mm after ca. 0.006 s (Figure 11.9b). The droplet then started to contract slowly. As one would expect, most of the contraction happened on the upper side due to the effect of gravity. Ca. 0.2 s after the impact, the droplet had contracted to a stable state in which it had a diameter of ca. 6.0 mm (Figure 11.9).

11.4 Discussion

These experiments confirm the earlier findings that were reviewed in the theory sections of this thesis. Superhydrophobic and near-superhydrophobic surfaces are able to repel incoming water drops, leaving behind a completely dry surface. The much poorer performance on the surfaces with water condensate is due to condensate droplets that have been trapped in the pores of the silicon surface. Because some or all of the surface pores are filled with

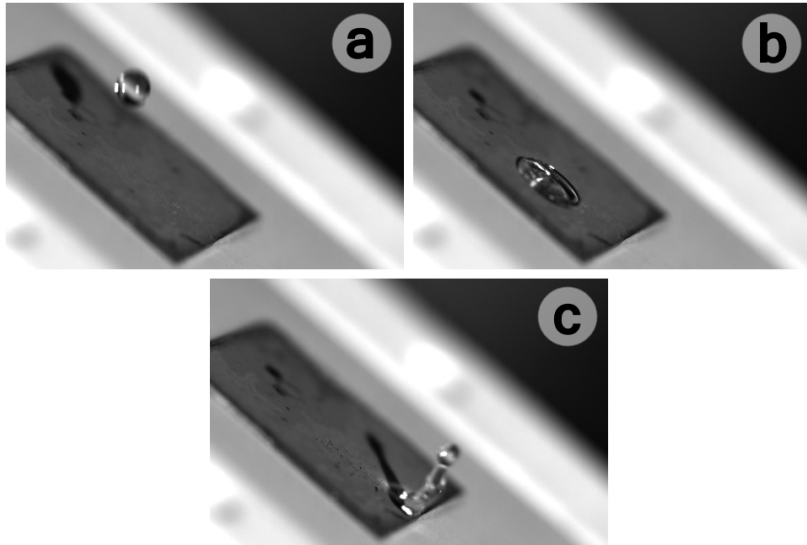


Figure 11.8: Droplet impact on a dry and tilted surface.

water instead of air, the hydrophobicity decreases according to the Cassie-Baxter equation, and the dynamic droplet behavior is also influenced by this deterioration.

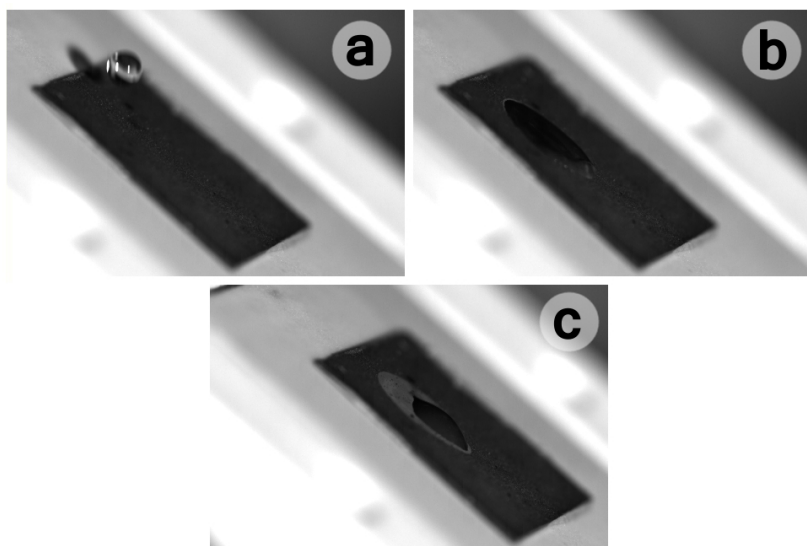


Figure 11.9: Droplet impact on a tilted surface exposed to water condensation.

Chapter 12

Conclusions and Outlook

There is a large body of literature to support the suggestion that surfaces with micro-nano hierarchical roughness can induce superhydrophobicity. On such surfaces, water droplets bead up with a high contact angle, and they roll off with ease when the surface is slightly inclined. They also show a self-cleaning effect, as water droplets tend to pick up contamination particles as they move down the surface.

Even if there is no direct correlation between superhydrophobicity and icephobicity, many superhydrophobic surfaces have been observed—at least under some environmental conditions—to delay freezing, and minimize or even eliminate both static and dynamic ice accumulation. Moreover, ice that accumulates on superhydrophobic surfaces in the Cassie-Baxter state is more weakly bonded, and is therefore relatively easy to remove.

Many different strategies have been suggested to design surfaces that effectively resist transition to the Wenzel state—a transition which may otherwise be brought about by mechanisms such as kinetic energy, vibration, and impingement of high-energy supercooled water droplets. Closed-cell structures have looked particularly interesting in this regard. Physical experiments have shown that they have better stability to pressure than open-cell structures, but judging by the molecular dynamics simulations carried out in this thesis, they seem to have no other comparative advantage—static wetting on surfaces with closed-cell textures follow the same wetting laws as static wetting on surfaces with open-cell textures.

Despite showing promising results in many cases, there are still major issues that ought to be understood and addressed before deploying nanostructured materials in commercial anti-icing applications at large scale. The micro-nano hierarchical surfaces fabricated so far are prone to failure due to pressure and impact, due to physical damage of the surface structure, or—as the droplet impact experiments in this thesis have confirmed—due to deteri-

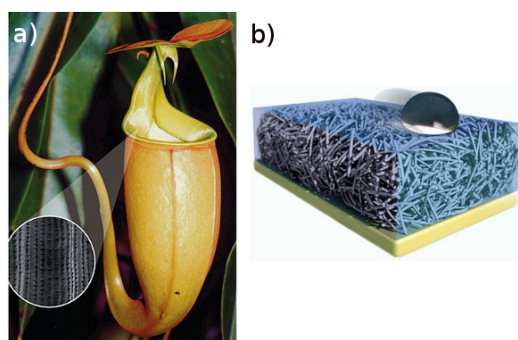


Figure 12.1: (a) *Nepenthes* pitcher plant.^[60] (b) A liquid droplet is repelled from the surface by an immobilized liquid in a porous structure.^[59]

oration because of water condensation. In addition, the production is often both cumbersome and expensive. Solving all of these problems may require an entirely new approach.

Wong et al.^[59] recently came up with a revolutionary new concept which might serve as a remedy for these problems. Their surfaces are called *SLIPS*, which is short for "Self-healing, slippery Liquid-Infused Porous Surfaces". Their inspiration was found in nature, more specifically in the carnivorous *Nepenthes* pitcher plant's almost frictionless surface.

After rain, this plant creates a slick coating on its top by locking in a layer of water in its porous structure, which is shown in the inset in Figure 12.1a. Its sweet smell attracts insects like ants and spiders. The feet of these creatures are covered with oil so that they are repelled by the thin layer of water on the plant's surface. Thus, the insects will slide down into the "trap" as soon as they move onto the slippery surface. This approach is fundamentally different from that of the lotus leaf. Rather than using its solid surface to repel a liquid directly, the pitcher plant uses an intermediary liquid to repel another liquid, the solid's function being only to immobilize the intermediary liquid. The effect can be compared to that of a car hydroplaning with its tires gliding on a thin water film rather than on the road, and is illustrated in Figure 12.1b.

Inspired by this plant, Wong et al. started with porous materials—such as a network of teflon nanofibers—and infused it with a low-surface energy perfluorinated fluid. 3M Fluorinert FC-80 and DuPont Krytox 100 and 103 are good candidates. As liquid surfaces are intrinsically defect-free and fluidic, defects in the underlying porous substrate will quickly be healed by

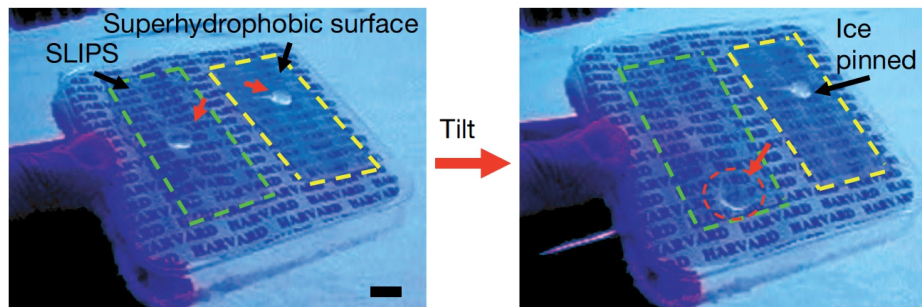


Figure 12.2: Ice mobility on a SLIPS (left) compared to strong ice adhesion to a epoxy-resin-based nanostructured superhydrophobic surface (right). The experiments were performed outdoors at -4°C and 45% humidity.^[59]

liquid spontaneously moving into damaged sites by capillary wicking, refilling voids, cracks, etc. Their experiments showed that the SLIPS were able to repel water at a pressure of ~ 676 atm, which was the highest available pressure in their setup. This is almost 100 times the highest recorded pressure stability of a superhydrophobic surface to date!^[59] In addition, both very low CAHs ($< 2^{\circ}$) and low tilt angles ($\leq 3^{\circ}$) for droplet volume $\leq 2 \mu\text{L}$ were observed. The SLIPS were also tested for their ability to repel ice in outdoor conditions, and showed much better performance than the epoxy-resin-based superhydrophobic surfaces which they were compared to, displaying both reduced frost formation and lower ice adhesion (see Figure 12.2).

Whether the SLIPS concept is technologically and commercially viable remains to be seen. Regardless, future work in the field of superhydrophobicity and anti-icing should aim at advancing our knowledge of the fundamental physics of icing, and our knowledge of how wetting and freezing mechanisms are affected by surface parameters like those outlined in Chapter 4. An interesting possibility would be to employ the honeycomb structure in conjunction with other stabilizing designs, such as convex curvature.

Appendix A

Programming codes

A.1 Code used to create graphene layers

The following Fortran code was used to create the five-layer stack of graphene sheets. Lines starting with an exclamation mark are comments only, and are not executed.

```
!
!   A-B stacking double graphene coordinates generator
!       with orientation theta
!
!       m-----
!       |         n-----|-----
!       |         |         |         |         Graphite Oscillation
!       |         |         |         |         Layer n on layer m
!       |         |         |         |
!       |-----|-----|
!       |         |         |
!       |         |         |
!
!
!   input instruction
!   line #1: length in 1, 2 direction ( Ang.)
!   line #2: angle of layer 1 and 2 ( Deg.)
!   length unit: Angstrom
```

```
PROGRAM mkgraphene
```

```

IMPLICIT NONE
INTEGER :: i, j, k, ia, ib, layers
INTEGER, DIMENSION(2) :: maxn1,maxn2
DOUBLE PRECISION :: CC, PI
DOUBLE PRECISION :: LC, theta1, theta2
DOUBLE PRECISION, DIMENSION(2) :: length1,length2, L1, L2, x0, ba
DOUBLE PRECISION, DIMENSION(2) :: tmp1, tmp2, tmp3, tmp4
DOUBLE PRECISION, DIMENSION(2) :: ntmp1, ntmp2, ntmp3, ntmp4
DOUBLE PRECISION, DIMENSION(1000000,2) :: xa, xb, nxa, nxb

!-----
real(8), parameter :: h=3.35
!-----
PI = 4.D0 * ATAN(1.D0)
!-----
CC = 1.0*1.42D0

layers=5
length1(1)=1.5D0*CC*60.D0
length1(2)=DSQRT(3.D0)*CC*50.D0
length2(1)=1.5D0*CC*60.D0
length2(2)=DSQRT(3.D0)*CC*50.D0
theta1=0.
      theta2=0.
      write(*,*) "x,y= ",length1(1)/10.0,length1(2)/10.0,"nm"

!-----
LC = DSQRT(3.D0) * CC
L1 = (/1.5D0 * CC, 0.5D0 * DSQRT(3.D0) * CC/)
L2 = (/0.D0, DSQRT(3.D0) * CC/)

! length : graphene length x and y dimension
!           both for layer m and n
! theta1 : theta for layer m
! theta2 : theta for layer n

maxn1(:) = INT(4.D0 * length1(:) / LC)
maxn2(:) = INT(4.D0 * length2(:) / LC)
theta1 = theta1 * PI / 180.D0
theta2 = theta2 * PI / 180.D0

```

```

! A stacking
x0(1) = 0.5D0 * CC * 0.5D0
x0(2) = 0.5D0 * CC * 0.5D0 * DSQRT(3.D0)
! B stacking, with the same vector L as A, but different origin
ba(1) = 0.5D0 * CC
ba(2) = 0.5D0 * DSQRT(3.D0) * CC

ia = 0
ib = 0

DO i = -maxn1(1), maxn1(1)
DO j = -maxn1(2), maxn1(2)
!
! A stacking
!
tmp1(:) = DBLE(i) * L1(:) + DBLE(j) * L2(:) + x0(:)
tmp2(:) = DBLE(i) * L1(:) + DBLE(j) * L2(:) - x0(:)

! apply orientation
ntmp1(1) = DCOS(theta1) * tmp1(1) - DSIN(theta1) * tmp1(2)
ntmp1(2) = DSIN(theta1) * tmp1(1) + DCOS(theta1) * tmp1(2)
ntmp2(1) = DCOS(theta1) * tmp2(1) - DSIN(theta1) * tmp2(2)
ntmp2(2) = DSIN(theta1) * tmp2(1) + DCOS(theta1) * tmp2(2)

IF ((DABS(ntmp1(1)) .LT. 0.5*length1(1)) .AND. &
& (DABS(ntmp1(2)) .LT. 0.5*length1(2))) THEN
ia = ia + 1
xa(ia,:) = ntmp1(:)
END IF
IF ((DABS(ntmp2(1)) .LT. 0.5*length1(1)) .AND. &
& (DABS(ntmp2(2)) .LT. 0.5*length1(2)) ) THEN

ia = ia + 1
xa(ia,:) = ntmp2(:)
END IF
END DO
END DO
DO i = -maxn2(1), maxn2(1)
DO j = -maxn2(2), maxn2(2)

```

```

!
! B stacking , translate with the vector A->B
!
tmp3(:) =DBLE(i) * L1(:) + DBLE(j) * L2(:) + x0(:)+ ba(:)
tmp4(:) = DBLE(i) * L1(:) + DBLE(j) * L2(:) - x0(:)+ ba(:)
! apply orientation
ntmp3(1) = DCOS(theta2) * tmp3(1) - DSIN(theta2) * tmp3(2)
ntmp3(2) = DSIN(theta2) * tmp3(1) + DCOS(theta2) * tmp3(2)
ntmp4(1) = DCOS(theta2) * tmp4(1) - DSIN(theta2) * tmp4(2)
ntmp4(2) = DSIN(theta2) * tmp4(1) + DCOS(theta2) * tmp4(2)

IF ((DABS(ntmp3(1)) .LT. 0.5*length2(1)) .AND. &
& (DABS(ntmp3(2)) .LT. 0.5*length2(2))) THEN
    ib = ib + 1
    xb(ib,:) = ntmp3(:)
END IF
IF ((DABS(ntmp4(1)) .LT. 0.5*length2(1)) .AND. &
& (DABS(ntmp4(2)) .LT. 0.5*length2(2)) ) THEN
    ib = ib + 1
    xb(ib,:) = ntmp4(:)
END IF
END DO
END DO

open(10 , file ='graphene.xyz' , status ='unknown ')

if (mod(layers ,2)==1)then
    k=ia*(int(layers/2)+1)+ib*int(layers/2)
else
    k=(ia+ib)*int(layers/2)
end if

write(10 ,*) k
write(10 ,*)

do k=1,layers
if (mod(k,2)==1)then
DO i = 1, ia
WRITE (10 , '( a2,3F12.5) ' ) 'C ' ,1.0*xa(i ,1) ,1.0*xa(i ,2) , (1-k)*h
END DO

```

```

else
DO i = 1, ib
WRITE (10, '(a2,3F12.5)') 'C ', 1.0*xb(i,1), 1.0*xb(i,2), (1-k)*h
END DO
endif
end do

!           DO i = 1, ia
!           WRITE (10, '(A2,3F12.5)') 'U ', xa(i,:), h
!           END DO
!           DO i = 1, ib
!           WRITE (10, '(A2,3F12.5)') 'D ', xb(i,:), h+3.4
!           END DO

close(10)
END

```

A.2 Code used to convert XYZ file to gro file

The following Fortran code was used to convert the XYZ file format to a gro file format.

```

program xyz2gro
implicit none
integer :: i, j, mid, id
real(8) :: CC, x, y, z, rtemp1, rtemp2, rtemp3, rtemp4
real(8) :: x0, xtmp, ytmp, ztmp
real(8) :: y0, xwater, ywater, zwater
integer :: atoms
character(len=5) :: cha1, cha2, temp
=====
real(8), parameter :: h=3.35
CC = 1.0*1.42D0
x0=1.5D0*CC*60.D0
y0=DSQRT(3.D0)*CC*50.D0
write(*,*)
=====
xwater=8.0 !nm
ywater=8.00

```

```

ywater=7.0
zwater=7.0

!integers 7.0 !n,mn
=====
!n=7950
!mn=2650
open(10,file='5graphene.xyz',status='unknown')
open(20,file='water-graphene-C.gro',status='unknown')

write(20,*) "Generated by changing xyz to gro"
read(10,*) atoms
write(20,*) atoms
!read(10,"(i8,4f8.3)") atoms,rtemp1,rtemp2,rtemp3,rtemp4
read(10,*)

i=1
x0=x0/10.0
y0=y0/10.0
do while(i<=atoms)
!read(10,"(a2,3f12.5)") cha2,x,y,z
read(10,*) cha2,x,y,z

x=x/10.0
y=y/10.0
z=z/10.0

xtmp=x
ytmp=y
ztmp=z

!x=xtmp+x0/2.0
!y=ytmp+y0/2.0
!z=(ytmp+ztmp+12.5)*sqrt(2.0)/2.0

!x=xtmp*(1.0+(xtmp+x0/2.0)/x0*0.2-0.1)
!y=ytmp*(1.0+(ytmp+y0/2.0)/y0*0.2-0.1)
!z=ztmp

!x=x+7.0
!y=y+2.0

```

```

    if (cha2=='C      ') then
        write(20,"(i5,2a5,i5,3f8.3)") 1,'CNT  ',ADJUSTR(cha2),i,x,y,z
    else
        write(20,"(i5,2a5,i5,3f8.3)") 2,'BAL',ADJUSTR(cha2),i,x,y,z
    endif

i=i+1
enddo

write(20,"(3f12.5)") xwater,ywater,zwater

close(10)
close(20)
end program xyz2gro

```

A.3 Code Used to Cut Holes in the Graphene

```

program cut_graphene
implicit none

integer :: i,j,mid,id,flag,option,ii,jj,kk
real(8),parameter :: pi=3.141592653
real(8)::x,y,z,CC,x0,y0,xwater,ywater
real(8)::xtmp,ytmp,ztmp,r,cutflag,xc,yc
integer :: atoms,new_atoms,new_mol,n
character(len=5)::cha1,cha2,temp
!-----
n=5 !cells per edge
r=0.4 !hole radius, nm

CC = 1.0*1.42D0 !strain
x0=1.5D0*CC*60.D0/10.0
y0=DSQRT(3.D0)*CC*50.D0/10.0
xwater=7.0
ywater=7.0
!-----
open(10,file='water-graphene.gro',status='unknown')
open(20,file='water-graphene_new_cut.gro',status='unknown')

```

```

option=0 !0 for cut graphen; 1 for cut water
if(option==0) then !cut graphene
  read(10,*)
  write(20,*)
  read(10,*) atoms
  write(20,*)
  write(*,*) atoms

  i=1
  new_atoms=0
  new_mol=2
  do while(i<=atoms)
    read(10,"(i5,2a5,i5,3f8.3)") mid,cha1,cha2,id,x,y,z

=====ping yi graphene=====
=====ping yi graphene=====
    if(cha2==' C' .or. cha2==' G') then
      xtmp=x+xwater*0.5
      ytmp=y+ywater*0.5
      ztmp=z
    else
      xtmp=x
      ytmp=y
      ztmp=z
    endif

=====
=====cut graphene=====
    cutflag=0

    if(cha2==' C' .or. cha2==' G') then
      do ii=1,n
      do jj=1,n
        xc=(ii-0.5)*x0/real(n)-(x0*0.5-xwater*0.5)
        yc=(jj-0.5)*y0/real(n)-(y0*0.5-ywater*0.5)
        if((xtmp-xc)**2+(ytmp-yc)**2 .LE. r**2) then
          cutflag=1
          !
          exit
        endif
      enddo
    endif
  enddo

```

```

        enddo
    else
        cutflag=0
    endif

    if (cutflag==0) then
        new_atoms=new_atoms+1
        x=xtmp
        y=ytmp
        z=ztmp
        write(20,"(i5,2a5,i5,3f8.3)") mid,cha1,cha2,new_atoms,&
            &x,y,z
    endif
!=====

    i=i+1
    enddo

elseif(option==1)then !cut water

    read(10,*)
    read(10,*) atoms
    write(*,*) atoms

    i=1
    new_atoms=0
    new_mol=2
    do while(i<=atoms)

        read(10,"(i5,2a5,i5,3f8.3)") mid,cha1,cha2,id,x,y,z

!=====cut water=====
        if(cha2==' C' .or. cha2==' G') then
            if(z<5.1) then
                new_atoms=new_atoms+1
                write(20,"(i5,2a5,i5,3f8.3)") mid,cha1,cha2,&
                    &new_atoms,x,y,z
            endif
        elseif(cha2==' OW') then
            flag=0
!            if(.not.(z>=3.0 .and. (x-x0/20.0)&

```

```

& **2+(y-y0/20.0)**2 >= 2.87)) &
& then
    if (z < 5.6) then
        new_atoms=new_atoms+1
        new_mol=new_mol+1
        write (20, "( i5 , 2 a5 , i5 , 3 f8 . 3 )" ) new_mol , cha1 , cha2 , &
        & new_atoms , x , y ,
    else
        flag=1
    endif
else
    if (flag == 0) then
        new_atoms=new_atoms+1
        write (20, "( i5 , 2 a5 , i5 , 3 f8 . 3 )" ) new_mol , cha1 , cha2 , &
        & new_atoms , x , y ,
    endif
endif
endif


---


    i=i+1
enddo

else

endif

write (*,*) new_atoms
write (20,*) x0,y0,20.0
close (10)
close (20)

end program cut_graphene

```

A.4 Code Used to Convert .gro files to LAMMPS input files

```

program gro2lammps
implicit none
integer :: i , mid , id , flag
real (8) :: x , y , z
integer :: atoms , nofbonds , nofangles = 0

```

```

character (len =5)::cha1 , cha2 , temp
real (8)::x0 , xtemp , xwater
real (8)::y0 , ytemp , ywater
real (8)::CC

=====
integer , parameter :: num_C=yyy
CC = 1.0*1.42D0
x0=1.5D0*CC*60.D0
y0=DSQRT(3.D0)*CC*50.D0

xwater=7.0 !nm
ywater=7.0
xtemp=0.5*xwater*10.0 !ping yi original point to the center
ytemp=0.5*ywater*10.0
=====
flag=0
open(10 , file = 'kjxxxwater-graphene_new_cut.gro' , status = 'unknown')
open(20 , file = 'kjxxxwater-graphene' , status = 'unknown')

write(20 , *) " water and graphene"
write(20 , *)
read(10 , *)
!read(10 , "(a10)") temp
read(10 , *) atoms
write(20 , *) atoms , 'atoms'

write(20 , "(i8 , a7)") 2*(atoms-num_C)/3 , 'bonds'
write(20 , "(i8 , a7)") (atoms-num_C)/3 , 'angles'

write(20 , *)

write(20 , "(i5 , a12)") 3 , 'atom types'
write(20 , "(i5 , a12)") 1 , 'bond types'
write(20 , "(i5 , a12)") 1 , 'angle types'
write(20 , *)

write(20 , "(2f12.5 , a9)") -x0/2.0 , x0/2.0 , 'xlo xhi'
write(20 , "(2f12.5 , a9)") -y0/2.0 , y0/2.0 , 'ylo yhi'
write(20 , "(2f12.5 , a9)") -30.0 , 90.0 , 'zlo zhi'

```

```

write(20,*)
write(20,*) 'Masses '
write(20,*)
write(20,"(i,f12.5)") 1,15.9994
write(20,"(i,f12.5)") 2,1.0080
write(20,"(i,f12.5)") 3,12.0000
write(20,*)
write(20,*) 'Bond Coeffs '
write(20,*)
write(20,"(i,f9.4,f12.5)") 1,19.52,1.0000
write(20,*)
write(20,*) 'Angle Coeffs '
write(20,*)
write(20,"(i,f9.4,f12.5)") 1,2.385,109.47
write(20,*)
write(20,*) 'Atoms '
write(20,*)
i=1
do while(i<=atoms)
!read(10,"(i5,2a5,i5,3f9.4)") mid,cha1,cha2,id,x,y,z
read(10,"(i5,2a5,i5,3f8.3)") mid,cha1,cha2,id,x,y,z

if(id==0) flag=flag+1
id=id+100000*flag
if(id/=i) then
write(*,*) 'wrong!'
endif

x=10.0*x-xtemp
y=10.0*y-ytemp
z=10.0*z

!-----
!-----
if(cha2==' C') then
write(20,"(i8,i8,i3,f7.3,3f14.6)") id,mid,3,0.0,x,y,z

elseif(cha2==' HW1'.or.cha2==' HW2') then
! write(20,"(i8,i8,i3,f9.4,3f14.6)") id,mid,2,0.3650,x,y,z
!reax
write(20,"(i8,i8,i3,f9.4,3f14.6)") id,mid,2,0.4238,x,y,z
!SPC/E

```

```

! write(20,"(i8,i8,i3,f9.4,3f14.6)") id,mid,2,0.5242,x,y,z
!TIP4P

elseif(cha2==' OW') then
! write(20,"(i8,i8,i3,f9.4,3f14.6)") id,mid,1,-0.7300,x,y,z !reax
write(20,"(i8,i8,i3,f9.4,3f14.6)") id,mid,1,-0.8476,x,y,z
! write(20,"(i8,i8,i3,f9.4,3f14.6)") id,mid,1,-1.0484,x,y,z
nofangles=nofangles+1
endif
i=i+1
enddo

nofbonds=2*nofangles
write(20,*)
write(20,*) " Bonds"
write(20,*)
i=num_C+1
do while(i<=nofbonds/2+num_C)
write(20,"(4i8)") 2*(i-num_C)-1,1,3*(i-num_C)-2+num_C,3*&
&(i-num_C)-1+num_C
write(20,"(4i8)") 2*(i-num_C),1,3*(i-num_C)-2+num_C,3*&
&(i-num_C)+num_C
i=i+1
enddo

write(20,*)
write(20,*) " Angles"
write(20,*)
i=num_C+1
do while(i<=nofangles+num_C)
write(20,"(5i8)") i-num_C,1,3*(i-num_C)-1+num_C,3*(i-num_C)&
&-2+num_C,3*(i-num_C)+
i=i+1
enddo

close(10)
close(20)
end

```

A.5 Input file

```

units                metal
atom_style           full
pair_style           lj/charmm/coul/long 8.0 10.0
bond_style          harmonic
angle_style         harmonic
boundary            p p p
processors           3 2 2
read_data            ./water-graphene\${label}
pair_coeff           * * 0.0 0.0
pair_coeff           1 1 6.735e-3 3.166
pair_coeff           1 3 \${epsilon}e-3 3.19
kspace_style        ppm 0.0001
group               graphene type 3
group               oxygen type 1
group               hydrogen type 2
group               water type 1 2
variable            nowm equal count(oxygen)
variable            sw equal (xhi-xlo)*(yhi-ylo)
variable            ave_z equal xcm(oxygen,z)
compute            ef graphene group/group oxygen
variable            ave_fx equal c_ef[1]/\${sw}*1.60217646e5
variable            ave_fy equal c_ef[2]/\${sw}*1.60217646e5
variable            ave_fz equal c_ef[3]/\${sw}*1.60217646e5
fix                31 water shake 0.0001 100 10000000 b 1 a 1
velocity           graphene set 0.0 0.0 0.0 units box
fix                2 water nvt temp 300.0 300.0 0.1
fix                10 oxygen momentum 100 linear 1 1 0
thermo_style        custom step cpu v_ave_z v_ave_fx v_ave_fy v_ave_fz&
                   &c_ef etotal pe ke
thermo             100
thermo_modify       flush yes
dump               2 all atom 10000 atomacc.lammpstrj
dump               1 oxygen xyz 200 oxygen.xyz
restart            500000 restart
timestep           1.0e-3
run                2000000

```

References

- [1] S. Frankenstein, A.M. Tuthill, "Ice Adhesion to Locks and Dams: Past Work; Future Directions?" *J. Cold Reg. Eng.* **2002**, 16, pp.83-96.
- [2] F. Wang et al., "A Facile Superhydrophobic Surface for Mitigating Ice Accretion" *Properties and Applications of Dielectric Materials* **2009**, pp.150-153.
- [3] M. Farzaneh, "Atmospheric Icing of Power Networks", Springer, **2008**.
- [4] "Understanding the Stall-Recovery Procedure for Turboprop Airplanes in Icing Conditions" *Flight Safety Digest* **April 2005**, 24 (4), pp.1-17.
- [5] <http://www.aopa.org/asf/publications/sa11.pdf>
- [6] L. Mishchenko† et al., "Design of Ice-free Nanostructured Surfaces Based on Repulsion of Impacting Water Droplets" *ACS nano* **2000**, 4(12), pp.7699-7707.
- [7] <http://www.aviation-safety.net/>
- [8] http://www.pilotfriend.com/safe/safety/icing_conditions.htm
- [9] J. Ayres et al., "Characterization of Titanium Alkoxide Sol-Gel Systems Designed for Anti-Icing Coatings" *J. Coat. Technol. Res.* **2007**, 4, pp.463-471.
- [10] "Aircraft Icing Handbook" Civil Aviation Authority, Lower Hutt, New Zealand, **2000**.
- [11] V. F. Petrenko, R. W. Whitworth, "Physics of ice", Oxford University Press, **1999**.
- [12] B. W. Jones, "Discovering the Solar System", John Wiley and Sons, **2007**.

- [13] C. D. Ahrens, "Meteorology today: an introduction to weather, climate, and the environment", Cengage Learning, **2007**.
- [14] J. M. Theriault et al., "On the Simulation of Winter Precipitation Types", *J. Geophys. Res.*, **2000**, 111(2006), pp. 1-11.
- [15] F. Arianpour, "Water and Ice-Repellent Properties of Nanocomposite Coatings Based on Silicone Rubber", Master's thesis, Universite du Quebec, December **2010**.
- [16] http://www.wmo.int/pages/prog/www/IMOP/meetings/Surface/ET-STMT-2/COST-727-report_MCH-V75.pdf
- [17] http://t1.gstatic.com/images?q=tbn:ANd9GcRz9ywdrFfzPVAQMKPE_a1S_nTyHjJN5ypi1FfnGkpS-OkLOSJcEjLL1KAN
- [18] Z. Liu et al., "Frost formation on a super-hydrophobic surface under natural convection conditions", *Int. J. Heat Mass Transfer*, **2008**, 51, pp. 5575-5982.
- [19] A. Carré, K. L. Mittal, "Superhydrophobic Surfaces", VSP, **2009**.
- [20] P. Roach et al., "Progress in superhydrophobic surface development", *Soft Matter*, **2007**, 7, pp. 224-240.
- [21] R.K. Sharma, "Elementary Chemistry", Discovery Publishing House, **2007**.
- [22] B. He et al., "Multiple Equilibrium Droplet Shapes and Design Criterion for Rough Hydrophobic Surfaces", *Langmuir*, **2003**, 19, pp. 4999-5003.
- [23] S.H. Kim, "Fabrication of Superhydrophobic Surfaces", *J. Adhes. Sci. Technol.*, **2008**, 22, pp. 235-250.
- [24] B. Bhushan, "Nanotribology and Nanomechanics II", Springer, **2011**.
- [25] W. Barthlott, C. Neinhuis, "Purity of the sacred lotus, or escape from contamination in biological surface", *Planta*, **1997**, 202, pp. 1-8.
- [26] P.G. de Gennes et al., "Capillarity and wetting phenomena: drops, bubbles, pearls, waves", Springer, **2004**.
- [27] J.T. Hirvi, T.A. Pakkanen, "Wetting of Nanogrooved Polymer Surfaces", *Langmuir*, **2007**, 23, pp. 7724-7729.

- [28] R. N. Wenzel, "Resistance of Solid Surfaces to Wetting by Water", *Ind. Eng. Chem.*, **1936**, 28 (8), pp. 988-994.
- [29] L. Jiang, L. Feng, "Bioinspired intelligent nanostructured interfacial materials", Chemical Industry Press, **2010**.
- [30] B. Bhushan et al., "Micro-, nano- and hierarchical structures for superhydrophobicity, self-cleaning and low adhesion", *Phil. Trans. R. Soc. A*, **2009**, 367, pp. 1631-1672.
- [31] A. B. D. Cassie, S. Baxter, "Wettability of Porous Surfaces", *Trans. Faraday Soc.*, **1944**, 40 (8), pp. 546-551.
- [32] Q. S. Zheng et al., "Effects of Hydraulic Pressure on the Stability and Transition of Wetting Modes of Superhydrophobic Surfaces" *Langmuir* **2005**, 21, pp. 12207-12212.
- [33] L. Gao, T. J. McCarthy, "Wetting 101°", *Langmuir*, **2009**, 25 (24), pp. 14105-14115.
- [34] C. G. L. Furnidge, "Studies at phase interfaces. I. The sliding of liquid drops on solid surfaces and a theory for spray retention", *J. Colloid Sci.*, **1962**, 17, pp. 309-324.
- [35] D. Öner, T. J. McCarthy, "Ultrahydrophobic Surfaces. Effects of Topography Length Scales on Wettability", *Langmuir*, **2000**, 16, pp. 7777-7782.
- [36] Z. Yoshimitsu et al., "Effects of Surface Structure on the Hydrophobicity and Sliding Behavior of Water Droplets", *Langmuir*, **2002**, 18, pp. 5818-5822.
- [37] B. Bhushan, "Biomimetics inspired surfaces for drag reduction and oleophobicity/philicity", *Beilstein J. Nanotechnol.*, **2011**, 2, pp. 66-84.
- [38] X. Q. Feng et al., "Superior Water Repellency of Water Strider Legs with Hierarchical Structures: Experiments and Analysis", *Langmuir*, **2007**, 23, pp. 4892-4896.
- [39] S. Herminghaus, "Roughness-induced non-wetting", *Europhys. Lett.*, **2000**, 52, pp. 165-170.
- [40] A. R. Parker, C. R. Lawrence, "Water capture by a desert beetle", *Nature*, **2001**, 414, pp. 133-34.

- [41] K. Autumn, "Adhesive force of a single gecko foot-hair" *Nature*, **2000**, 405(6787), pp. 681-685.
- [42] A. Lafuma, D. Quéré, "Superhydrophobic States", *Nature Materials*, **2003**, 2, pp. 457-460.
- [43] M. Nosonovsky, "Multiscale Roughness and Stability of Superhydrophobic Biomimetic Interfaces", *Langmuir*, **2007**, 23, pp. 3157-3161.
- [44] A. Tuteja et al., "Designing Superoleophobic Surfaces" *Science* **2007**, 318, pp. 1618.
- [45] Q. Zheng et al., "Mechanical and Superhydrophobic Stabilities of Two-Scale Surface Structure of Lotus Leaves", *Langmuir*, **2007**, 23, pp. 8212-8216.
- [46] Q. Zheng *et al.*, "Small is beautiful, and dry", *Sci. China Phys. Mech. Astron.*, **2010**, 53 (12), pp. 2245-2259.
- [47] D. Bartolo et al., "Bouncing or sticky droplets: impalement transitions on micropatterned surfaces", *Eur. Phys. Lett.*, **2006**, 74 (2), pp. 299-305.
- [48] B. Mockenhaupt et al., "Superhydrophobicity of Biological and Technical Surfaces under Moisture Condensation: Stability in Relation to Surface Structure" *Langmuir* **2008**, 24, pp. 13591-13597.
- [49] F. Wang et al., "Ice accretion on superhydrophobic aluminum surfaces under low-temperature conditions" *Cold Reg. Sci. Technol.* **2010**, 62(1), pp. 29-33.
- [50] L. Cao et al., "Anti-Icing Superhydrophobic Coatings" *Langmuir* **2009**, 25(21), pp.12444-12448.
- [51] S. Jung et al., "Are superhydrophobic surfaces best for icephobicity?" *Langmuir*, **2011**, 27(6), pp.3059-3066.
- [52] A. W. Neumann, R. David, Y. Zuo, "Applied Surface Thermodynamics, Second Edition", CRC Press, **2010**.
- [53] P. Tourkine et al., "Delayed Freezing on Water Repellent Materials" *Langmuir* **2009**, 25(13), pp. 7214-72156.
- [54] S. A. Kulinich, M. Farzaneh, "How Wetting Hysteresis Influences Ice Adhesion Strength on Superhydrophobic Surfaces, **2009**, 25 (16), pp. 8854-8856.

- [55] A. J. Meuler *et al.*, "Relationships Between Water Wettability and Ice Adhesion" *ACS Appl. Mater. Interfaces* **2010**, 2(11), pp.3100-3110.
- [56] S. A. Kulinich *et al.*, "Superhydrophobic Surfaces: Are They Really Ice-Repellent?", *Lamgmuir* **2011**, 27 (1), pp. 25-29.
- [57] K. K. Varanasi *et al.*, "Frost formation and ice adhesion on superhydrophobic surfaces", *Appl. Phys. Lett.* **2010**, 97, pp. 234102-234103 .
- [58] G. Zhang *et al.*, "Cicada Wings: A Stamp from Nature for Nanoimprint Lithography" *Small* **2006**, 2 (12), pp. 1440-1443.
- [59] T. S. Wong *et al.*, "Bioinspired self-repairing slippery surfaces with pressure-stable omniphobicity", *Nature*, **2011**, 477, pp. 443-447.
- [60] <http://news.harvard.edu/gazette/story/2011/09/plant-offers-slick-strategy/>
- [61] M. Nosonovskii, B. Bhushan, "Multiscale dissipative mechanisms and hierarchical surfaces: friction, superhydrophobicity, and biomimetics", Springer, **2008**.
- [62] <http://www.directindustry.com/prod/kruss/contact-angle-measuring-devices-14849-443837.html>
- [63] <http://ixbtlabs.com/articles/peltiercoolers/>
- [64] <http://face-kyowa.com/en/learning/learning1.html>
- [65] S. Farhadi *et al.*, "Anti-Icing Performance of Superhydrophobic Surfaces" *Appl. Surf. Sci.* **2010**, 257(14), pp.6264-6269.
- [66] S. A. Kulinich, M. Farzaneh, "Ice adhesion on super-hydrophobic surfaces", *Appl. Surf. Sci.* **2009**, 255, pp. 8153-8157.
- [67] <http://www.graphene.nat.uni-erlangen.de>
- [68] <http://physics.bu.edu/documents/pw1106.pdf>
- [69] F. Ercolessi, "A molecular dynamics primer", **1997**, <http://www.fisica.uniud.it/~ercolessi/md/md.pdf>.
- [70] <http://phycomp.technion.ac.il/~talimu/md2.html>
- [71] C. Yuan, "A Molecular Dynamics Study of the Spreading of Nano-Droplets", Master thesis, Royal Institute of Technology, Sweden, **2010**.

- [72] <http://lammps.sandia.gov/>
- [73] <http://www.ks.uiuc.edu/Research/vmd/>
- [74] X. Yong, L. T. Zhang, "Nanoscale Wetting on Groove-Patterned Surfaces", *Langmuir*, **2009**, 25(9), pp. 5045-5053.
- [75] J. Bai, et. al, "Graphene nanomesh", *Nature*, **2010**, 5, pp. 190-193.
- [76] S. Park, R. S. Ruoff, "Chemical methods for the production of graphenes", *Nature*, **2009**, 4, pp. 217-224.
- [77] K. K. S. Lau et al., "Superhydrophobic carbon nanotube forests", *Nano Letters*, **2003**, 3 (12), pp. 1701-1705.
- [78] R. D. Narhe and D. A. Beysens, "Nucleation and growth on a superhydrophobic grooved surface", *Phys. Rev. Lett.*, **2004**, 93 (7), pp. 1-4.
- [79] X. Xiao and Y. T. Cheng, "Condensed water on superhydrophobic carbon films", *J. Mater. Res.*, **2008**, 23 (8), pp. 2174-2178.
- [80] Y. Cheng and D. E. Rodak, "Is the lotus leaf superhydrophobic", *Appl. Phys. Lett.*, **2005**, 86, pp. 144101.
- [81] Y. Cheng et al., "Microscopic observations of condensation of water on lotus leaves", *Appl. Phys. Lett.*, **2005**, 87, pp. 194112.
- [82] L. Yin et al., "Stability of superhydrophobicity of lotus leaf under extreme humidity", *Chem. Lett.*, **2010**, 39, pp. 816-817.
- [83] R. D. Narhe et al., "Water condensation on zinc surfaces treated by chemical bath deposition", *Appl. Surf. Sci.*, **2010**, 256, pp. 4930-4933.
- [84] C. Chen et al., "Dropwise condensation on superhydrophobic surfaces with two-tier roughness", *Appl. Phys. Lett.*, **2007**, 90, pp. 173108.
- [85] J. B. Boreyko and C. Chen, "Self-propelled dropwise condensate on superhydrophobic surfaces", *Phys. Rev. Lett.*, **2009**, 103, pp. 184501-1-184501-4.
- [86] X. Deng et al., "Candle soot as a template for transparent robust superamphiphobic coating", *Science.*, **2012**, 335, pp. 67-70.
- [87] <http://iopscience.iop.org/>
- [88] <http://www.qft.iqfr.csic.es/docs/lammps/Manual.pdf>